RICE UNIVERSITY

Probing and Manipulating Ultracold Fermi Superfluids

by

Lei Jiang

A Thesis Submitted
in Partial Fulfillment of the
Requirements for the Degree

Doctor of Philosophy

Approved, Thesis Committee:

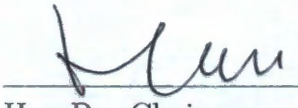

Han Pu, Chair
Associate Professor in Physics and Astronomy

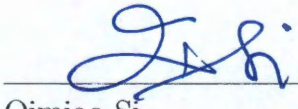

Qimiao Si
Harry C. and Olga K. Wiess Professor of Physics and Astronomy

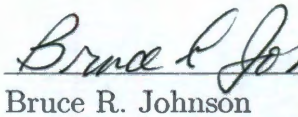

Bruce R. Johnson
Distinguished Faculty Fellow in Chemistry

Houston, Texas

November, 2011

ABSTRACT

Probing and Manipulating Ultracold Fermi Superfluids

by

Lei Jiang

Ultracold Fermi gas is an exciting field benefiting from atomic physics, optical physics and condensed matter physics. It covers many aspects of quantum mechanics. Here I introduce some of my work during my graduate study.

We proposed an optical spectroscopic method based on electromagnetically-induced transparency (EIT) as a generic probing tool that provides valuable insights into the nature of Fermi paring in ultracold Fermi gases of two hyperfine states. This technique has the capability of allowing spectroscopic response to be determined in a nearly non-destructive manner and the whole spectrum may be obtained by scanning the probe laser frequency faster than the lifetime of the sample without re-preparing the atomic sample repeatedly. Both quasiparticle picture and pseudogap picture are constructed to facilitate the physical explanation of the pairing signature in the EIT spectra.

Motivated by the prospect of realizing a Fermi gas of ^{40}K atoms with a synthetic non-Abelian gauge field, we investigated theoretically BEC-BCS crossover physics in the presence of a Rashba spin-orbit coupling in a system of two-component Fermi gas with and without a Zeeman field that breaks the population balance. A new bound state (Rashba pair) emerges because of the spin-orbit interaction. We studied the properties of Rashba pairs using a standard pair fluctuation theory. As the two-fold

spin degeneracy is lifted by spin-orbit interaction, bound pairs with mixed singlet and triplet pairings (referred to as rashbons) emerge, leading to an anisotropic superfluid. We discussed in detail the experimental signatures for observing the condensation of Rashba pairs by calculating various physical observables which characterize the properties of the system and can be measured in experiment.

The role of impurities as experimental probes in the detection of quantum material properties is well appreciated. Here we studied the effect of a single classical impurity in trapped ultracold Fermi superfluids. Although a non-magnetic impurity does not change macroscopic properties of s-wave Fermi superfluids, depending on its shape and strength, a magnetic impurity can induce single or multiple mid-gap bound states. The multiple mid-gap states could coincide with the development of a Fulde-Ferrell-Larkin-Ovchinnikov (FFLO) phase within the superfluid. As an analog of the Scanning Tunneling Microscope, we proposed a modified radio frequency spectroscopic method to measure the local density of states which can be employed to detect these states and other quantum phases of cold atoms. A key result of our self consistent Bogoliubov-de Gennes calculations is that a magnetic impurity can controllably induce an FFLO state at currently accessible experimental parameters.

Acknowledgements

I would like to express my sincere acknowledgement to my advisor Prof. Han Pu for his constructive suggestions, and continuous encouragements through the whole period of my Ph. D. study in Rice University. His guidance helped me overcome all the difficulties in my research.

Many aspects of this thesis benefit from the collaborations with Prof. Hong-Yuan Ling, Prof. Weiping Zhang, Prof. Hui Hu, Prof. Xia-Ji Liu, and Prof. Yan Chen. Their vast knowledge, deep insights and infectious enthusiasm in physics have made the work possible. Also their hospitality and time were greatly appreciated.

I thank Dr. Satyan Bhongale, Dr. Leslie Baksmaty, and Dr. Rong Yu with whom I have had many invaluable discussions. I also thank members in our group: Hong Lu, Ramachandhran Balasubramanian, Lin Dong, and Ying Dong who have provided valuable support from time to time.

Finally I thank my lovable parents, and wife, Xiao He. With their unfailing supports, this work is so meaningful.

Contents

Illustrations

Chapter 1

Introduction

In exploring the exotic feature of quantum mechanics, physicists have paid much attention to bosonic atoms. If one cools Bose gases to the point that their de Broglie wavelength is comparable to the average distance between atoms, individual atoms become indistinguishable and their wave functions overlap with each other. Bosonic atoms fall into the ground state to form Bose-Einstein Condensate (BEC). All the bosonic atoms have the same energy and are said to be degenerate. This could not happen to fermions as Pauli exclusion principle prohibits two fermions occupying the same state. Instead, fermions are obliged to fill all the different quantum energy states, starting from the energy bottom. This is said to constitute a degenerate fermi gas. BEC has been achieved in 1995 in alkali atoms[1, 2, 3]. To achieve degenerate fermi gas is more difficult as fermions in the same hyperfine state avoid collisions which are required for evaporate cooling. To combat this, a JILA group in Boulder prepared ^{40}K atoms in two different hyperfine states and got the degenerate fermi gas[4]. When temperature is low, scattering only occurs between atoms of different hyperfine states.

Fermions can condense if there is attractive interaction between them and they get paired. The pairing mechanism can be different. In one extreme, atoms are paired strongly and they can (as molecules) collapse into a Bose-Einstein Condensate. In the other extreme, atoms can pair weakly and they form correlated state analogous to Cooper pairs of electrons[5]. In this extreme, we have BCS pairings.

BCS theory was developed in 1950's and is one of the most successful condensed matter theories[6, 7] ever since. It is originally used to describe superconductivity for electrons in metal. Electrons form Cooper pairs when there is weak attractive interaction. A Cooper pair is formed by two electrons with total momentum zero near the Fermi surface. It can be viewed as a weakly bound boson and it forms and condenses at the same temperature. BCS theory has also been used to explain superfluidity in ^3He. In solid, the attractive interaction between electrons comes from the electron-phonon interaction, while in ^3He the attractive interaction comes from the spin fluctuation[8].

In dilute Fermi gases, instead of superconductivity for electron, for charge neutral atoms, it should be superfluidity. In experiments, atoms are in different hyperfine states. We use pseudo spins to label these different hyperfine states. The attractive interaction between two atoms comes directly from atom-atom interaction which is Van der Waals force. We consider a gas of fermions with the attractive interaction V. When the interaction is weak, the fermions undergo Cooper instability and form Cooper pairs. This is a many-body effect as the s-wave scattering length is negative. There is no two-body bound state. The length of the pair a_0 is very large and we have $na_0^3 >> 1$, where n is the gas density. Cooper pairs overlap with each other. It is proper to give them a mean field description.

In cold atoms, although the temperature is cooled below the degenerate temperature, it is very hard to push into the superfluid phase. As we know from BCS theory, the transition temperature T_c is proportional to $\exp(-1/|V|)$ where V is the interaction strength. For the Van der Waals interaction, T_c is an extremely low temperature. It is hopeless to go to the superfluid phase in ultra-dilute systems where the interaction strength is very small. This leads to a need for a method to increase the

interaction strength and Feshbach resonance is just the method[9, 10]. For Feshbach resonance, there is a bound state in a closed channel which is energetically unfavorable. When the bound state is resonant with the free atoms in the open channel, the scattering length for atoms in the open channel goes to infinity. Also the energy for different hyperfine states can be changed using an external magnetic field. Therefore one can tune the magnetic field to change the strength of the interaction. Using Feshbach resonance, the superfluid Fermi gas is achieved in 2002[11, 12].

Using Feshabch resonance, we can study the BCS-BEC crossover. The energy region near a broad resonance, where the s-wave scattering length goes to infinity, is called the unitary regime. There is only one length scale $1/k_F$. This is a strongly correlated system since the interaction between atoms is very strong. The pair size is comparable to the interparticle spacing. Quantum fluctuation is important in this region. Fermi gases in the unitary regime represent a type of "high temperature superfluid", as $T_c/T_F \approx 0.2$ (T_F is Fermi temperature), which is much larger than that for cuprate high temperature superconductors. It is hoped that studies of strongly interacting Fermi gases may shed light on the long-standing problem of the high T_c superconductivity.

When the interaction is even stronger, the scattering length is positive. Two fermions form a bound state and when the temperature is small, they may undergo Bose-Einstein Condensation. Now the pair length is small, $na_0^3 << 1$ and the internal structure of bound pairs is irrelevant. From the BCS regime to the BEC regime, the physics in different regimes is quite different, however it turns out that it is not a transition but a crossover. Physical quantities change smoothly from one regime to the other. In this chapter, I will first introduce the mean field theory for $T = 0$ to see the crossover, then I will introduce a theory beyond mean field to deal with the

$T \neq 0$ case. In the end, I will show some experiments.

In the next chapter, I will propose one method to detect the fermion pairing using electromagnetically induced transparency. I will test this method using both the mean-field model and the pseudogap model. In the third chapter, the ultracold fermion with the spin-orbit coupling will be presented. I will do the calculation using the functional integral method. A single classical impurity in Fermi superfluids is studied in the fourth chapter.

1.1 The Mean Field Theory of the BEC-BCS Crossover

Leggett first gave the general solution for crossover problem at zero temperature[13]. He assumed the system should have a BCS type ground state. The main difference from the original BCS theory is that for crossover theory, we not only need to consider the gap profile but also need to conserve the total number. With both gap equation and number equation taken into account, we have the mean field theory which was introduced to the ultracold fermion system by many different groups[14, 15, 16].

The temperature is so low that we only need to consider s-wave scattering. For s-wave scattering, the cross section for fermions within the same hyperfine state is zero due to the Pauli exclusion principle. We only need to consider the interaction between different hyperfine states. We write the model Hamiltonian as:

$$H = \sum_{\mathbf{k},\sigma} \xi_{\mathbf{k}} c^{+}_{\mathbf{k}\sigma} c_{\mathbf{k}\sigma} + \sum_{\mathbf{k},\mathbf{k}',\mathbf{q}} V_{\mathbf{k}\mathbf{k}'}(\mathbf{q}) c^{+}_{\mathbf{k}+\mathbf{q}/2,\uparrow} c^{+}_{-\mathbf{k}+\mathbf{q}/2,\downarrow} c_{-\mathbf{k}'+\mathbf{q}/2,\downarrow} c_{\mathbf{k}'+\mathbf{q}/2,\uparrow} \tag{1.1}$$

where $\xi_{\mathbf{k}} = \epsilon_{\mathbf{k}} - \mu = \hbar^2\mathbf{k}^2/2m - \mu$ is the fermion energy measured from the chemical potential μ. m is the mass of the atom. Here we only consider the population balanced and mass balanced case. $V_{\mathbf{k}\mathbf{k}'}(\mathbf{q})$ describes the attractive interaction and as the temperature and density are both extremely low, the detailed structure of the

scattering potential does not come into play. We only consider the simplest scattering potential in the form of a contact interaction.

$$V_{\mathbf{k}\mathbf{k}'}(\mathbf{q}) = g \tag{1.2}$$

which in real space corresponds to $V(\mathbf{r}-\mathbf{r}') = g\delta(\mathbf{r}-\mathbf{r}')$. This leads to an ultraviolet divergence in three dimensions and we have to renormalize the bare interaction g to remove the divergence at high momentum. This renormalization is equivalent to introducing the zero-range pseudopotential $V(\mathbf{r}) = g\delta(\mathbf{r})\frac{\partial}{\partial \mathbf{r}}\mathbf{r}$ [17].

$$\frac{m}{4\pi\hbar^2 a_s} = \frac{1}{g} + \frac{1}{V}\sum_{\mathbf{k}}\frac{1}{2\epsilon_{\mathbf{k}}} \tag{1.3}$$

where a_s is the s-wave scattering length for fermions, V is the total volume. As we know from the scattering theory[18], for s-wave, the scattering amplitude is

$$f_0(k) = -\frac{1}{a_s^{-1} + ik - k^2 R_{eff}} \tag{1.4}$$

where R_{eff} is the effective range of scattering. In ultracold Fermi gases system, for broad Feshbach resonance, the effective range of scattering is much smaller than the inter particle spacing. We can neglect it and the s-wave scattering amplitude becomes $f_0(k) = -1/(a_s^{-1} + ik)$. In the BCS regime, the weak attractive interaction is characterized by a small, negative scattering length. In the BEC regime, the large attractive interaction is characterized by a small, positive scattering length. In between, there is unitarity where $|a_s| \to \infty$. The system has "universal" behavior near this point, since there is no scale other than the Fermi energy E_F[19].

In the weak coupling limit $|na_s^3| << 1$, the BCS pairs have large pairing size and overlap with each other. We can therefore use the usual BCS wave function:

$$|\Phi_{0s}\rangle = \prod_{\mathbf{k}}(u_{\mathbf{k}} + v_{\mathbf{k}} c^+_{\mathbf{k},\uparrow} c^+_{-\mathbf{k},\downarrow})|vac\rangle \tag{1.5}$$

where $u_{\mathbf{k}}^2 = \frac{1}{2}\frac{\xi_{\mathbf{k}}+E_{\mathbf{k}}}{E_{\mathbf{k}}}$, $v_{\mathbf{k}}^2 = -\frac{1}{2}\frac{\xi_{\mathbf{k}}-E_{\mathbf{k}}}{E_{\mathbf{k}}}$ and $E_{\mathbf{k}}^2 = \xi_{\mathbf{k}}^2 + \Delta^2$.

We can define the superfluid gap parameter,

$$\Delta = \sum_{\mathbf{k}} g\langle c_{\mathbf{k},\uparrow}^{+} c_{-\mathbf{k},\downarrow}^{+}\rangle \tag{1.6}$$

which obeys the self-consistency equation at zero temperature.

$$\Delta = \sum_{\mathbf{k}'} g\frac{\Delta}{2E_{\mathbf{k}'}} \tag{1.7}$$

which is the gap equation at zero temperature. Introducing the function $\psi_{\mathbf{k}} = \Delta/E_{\mathbf{k}}$, the gap equation can be written in the form of a Schrödinger equation

$$(\hbar^2\mathbf{k}^2/m - 2\mu)\psi_{\mathbf{k}} = (1-2n_{\mathbf{k}})\sum_{\mathbf{k}'} g\psi_{\mathbf{k}'} \tag{1.8}$$

where $n_{\mathbf{k}} = v_{\mathbf{k}}^2 = [1 - \frac{\xi_{\mathbf{k}}}{E_{\mathbf{k}}}]/2$.

When the attractive interaction is strong enough, bound pairs will form with the energy $w_{\mathbf{q}} = -\varepsilon_0 + \hbar^2\mathbf{q}^2/2M$, where ε_0 is the binding energy, $M = 2m$. In the strong coupling limit, $n_{\mathbf{k}} \ll 1$, the gap equation reduces to the Schrödinger equation for a single bound pair.

$$(\hbar^2\mathbf{k}^2/m - 2\mu)\psi_{\mathbf{k}} = \sum_{\mathbf{k}'} g\psi_{\mathbf{k}'} \tag{1.9}$$

The chemical potential 2μ plays the role of eigenvalue and $2\mu = -\varepsilon_0$ in zeroth order.

In the mean field theory, physical quantities are calculated from the gap equation together with the number equation. In the weak coupling limit, which is the BCS limit, $\mu = E_F$ and $\Delta = \frac{8}{e^2}e^{-\pi/2k_F|a_s|}$, where E_F is Fermi energy and k_F is Fermi momentum. When the interaction strength increases, μ begins to decrease and eventually becomes negative in the BEC regime. In the deep BEC side, $\mu = -\frac{\hbar^2}{2ma_s^2} + \frac{\pi\hbar^2 a_s n}{m} = -\frac{\varepsilon_0}{2} + \frac{\pi\hbar^2 a_s n}{m}$ and $\Delta = \sqrt{\frac{16}{3\pi}}\frac{E_F}{\sqrt{k_F a_s}}$. The second term is the repulsive interaction between molecules. From the mean field theory, the molecule-molecule

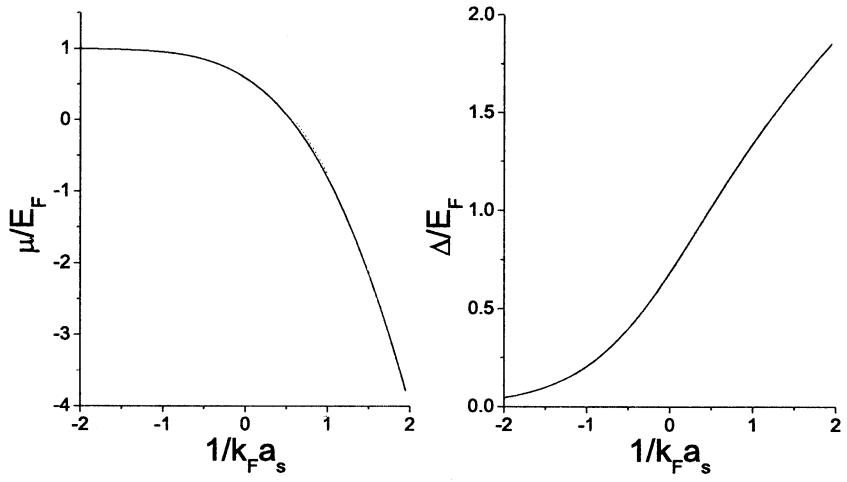

Figure 1.1 : Mean field results for chemical potential μ and gap Δ as functions of the interaction parameter $1/k_F a_s$.

scattering length $a_B = 2a_s$. In between, is called "pseudogap regime" (or "unitary regime", "resonant regime")[20, 21, 22]. Fig. 1.1 shows the evolvement of chemical potential and gap in the BEC-BCS crossover using the mean field theory. Both chemical potential and gap change smoothly from the BCS side (when $1/k_F a_S < 0$) to the BEC side (when $1/k_F a_S > 0$).

Now we introduce the ground state wave function in the BEC regime. The pair creation operator is:

$$b_{\mathbf{q}}^{+} = \sum_{\mathbf{k}} \phi_{\mathbf{k}} c_{\mathbf{k}+\mathbf{q}/2,\uparrow}^{+} c_{-\mathbf{k}+\mathbf{q}/2,\downarrow}^{+} \tag{1.10}$$

where $\phi_{\mathbf{k}}$ is the Fourier transform of the internal wave function. In the strong coupling limit, bound pairs can be viewed as molecular bosons and undergo Bose-Einstein Condensation. They will fall into a single state with the total momentum $\mathbf{q} = 0$ and the pair chemical potential μ_p reaches the bottom of the bound state band, $\mu_p = -\varepsilon_0$. We only need to consider b_0^{+} in the ground state.

$$[b_0, b_0^+] = \sum_{\mathbf{k}} |\phi_{\mathbf{k}}|^2 (1 - 2n_{\mathbf{k}}) \tag{1.11}$$

we can see that b_0^+ represents a bosonic operator in the strong coupling limit, when $n_{\mathbf{k}} \ll 1$, $\sum_{\mathbf{k}} |\phi_{\mathbf{k}}|^2 = 1$, $[b_0, b_0^+] = 1$.

The ground state is represented by

$$|\Phi_0\rangle = [\exp(N_p^{1/2} b_0^+)]|vac\rangle \tag{1.12}$$

where $N_p = N/2$ is the total number of pairs.

BCS superfluidity may be viewed as Bose-Einstein condensation of weakly bound Cooper pairs. The strong coupling limit expression Eq.(1.12) can be written in the BCS form Eq.(1.5) with

$$v_{\mathbf{k}} = \frac{N_p^{1/2} \phi_{\mathbf{k}}}{(1 + N_p |\phi_{\mathbf{k}}|^2)^{1/2}} \tag{1.13}$$

In this way, the ground state wave function varies smoothly from one limit to another and Eq.(1.5) provides a unified description of the many-body state over the whole regime.

This mean-field method for zero temperature gives us the basic idea for the crossover physics and is qualitatively correct compared with experiment. This simple method is consistent with the Bogoliubov-de Gennes theory at zero temperature and sets a starting point for many theories in population imbalanced system. Also this method connects to the Gross-Pitaevskii theory in the BEC regime.

One disadvantage of the mean field theory is that it omits fluctuations at zero temperature. The mean field theory drops Hartree shift in the BCS regime[23]; using the mean field theory, the scattering length between molecular bosons is $a_B = 2a_s$ in the BEC regime which does not agree with the exact result from the four-body problem[24] and quantum Monte Carlo calculation[25], where $a_B \approx 0.6a_s$. The ground

state energy density at the unitarity is of the form $E_g/N = (1+\beta)(3E_F/5)$, where $(1+\beta) = 0.44$ from quantum Monte Carlo calculation. In the mean field theory $(1+\beta) = 0.59$, which is about 34% larger than the quantum Monte Carlo result.

For finite temperature, the mean field calculation gives wrong physical picture on the BEC side. On the BCS side, transition temperature T_c is defined as the temperature at which pairs breaking starts to occur and the mean field theory gives the qualitatively correct answer. But on the BEC side the pairs are deeply bound and they form molecules and T_c should be defined as the temperature at which the total momentum $\mathbf{q} = 0$ state has macroscopic occupancy. While T_c in the mean field theory on the BEC side is actually the molecular dissociation temperature T^*.

1.2 Ladder Diagrams and Thouless Criterion

Generally speaking, all the methods beyond mean field have to consider pair fluctuation. Using diagram technique, one has to consider ladder diagrams, which describe the atom scattering accurately in the low density limit. In this section I will present results from calculating vertex function in ladder diagrams and derive Thouless criterion which provides a criterion for the onset of superfluidity[26]. In the next section I will introduce the pseudogap method. In chapter 3, the pair fluctuation using functional integral formalism is calculated.

The vertex function in ladder diagrams is also called T-matrix, which describes the multiple scattering process between two atoms in vacuum(two-body physics) or in medium(many-body physics). The diagram is shown in Fig. 1.2. Its form is

$$\Gamma(\mathbf{k},\mathbf{k}';q) = \frac{u(\mathbf{k},\mathbf{k}')}{\hbar} - \frac{1}{\hbar\beta V}\sum_{k''}\Gamma(\mathbf{k},\mathbf{k}'';q)G_{0\uparrow}(q/2+k'')G_{0\downarrow}(q/2-k'')u(\mathbf{k}'',\mathbf{k}') \quad (1.14)$$

where $G_{0\uparrow}$ is the free particle Green's function for spin-up atom, $G_{0\downarrow}$ is the free particle Green's function for spin-down atom. $k = (\mathbf{k}, iw_n)$ is fermionic four dimensional momentum, $w_n = (2n+1)\pi/\beta$ is fermionic Matsubara frequeny. $q = (\mathbf{q}, iv_m)$ is bosonic four dimensional momentum, $v_m = 2m\pi/\beta$ is bosonic Matsubara frequeny. These ladder diagrams describe accurately two particle scattering and are also important in many-body physics when the interaction between atoms is attractive. I take the interaction to be contact interaction $u(\mathbf{k},\mathbf{k}') = g$ which simplifies the formula

$$\Gamma(\mathbf{q}, iv_m) = \frac{g}{\hbar} - \frac{g}{V}\Gamma(\mathbf{q}, iv_m)\sum_{\mathbf{k}}\chi_0(\mathbf{k};q) \quad (1.15)$$

where

$$\chi_0(\mathbf{k};q) = \frac{1}{\beta\hbar^2}\sum_{iw_n}G_{0\uparrow}(\mathbf{q}/2+\mathbf{k}, iv_m/2+iw_n)G_{0\downarrow}(\mathbf{q}/2-\mathbf{k}, iv_m/2-iw_n) \quad (1.16)$$

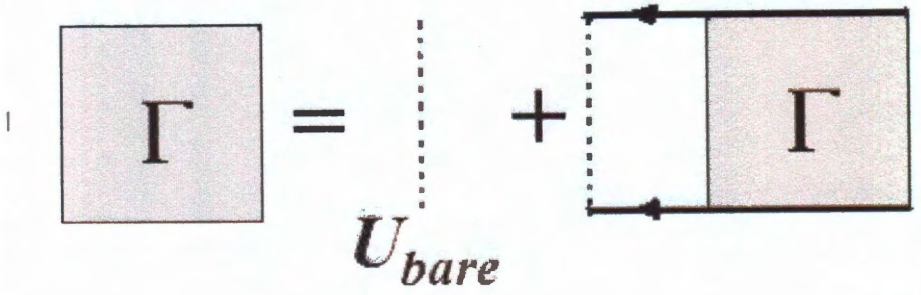

Figure 1.2 : Vertex function for ladder diagrams. The interaction part is the bare interaction.

From this we can derive the inverse of vertex function

$$\Gamma^{-1}(\mathbf{q}, iv_m) = \frac{\hbar}{g} + \frac{\hbar}{V}\sum_{\mathbf{k}}\chi_0(\mathbf{k};q) \tag{1.17}$$

To get rid of the ultraviolet divergence in the summation of momentum $\mathbf{k}$, we need to change it to

$$\Gamma^{-1}(\mathbf{q}, iv_m) = \frac{m}{4\pi\hbar a_s} + \frac{\hbar}{V}\sum_{\mathbf{k}}[\chi_0(\mathbf{k};q) - \frac{1}{2\epsilon_{\mathbf{k}}}] \tag{1.18}$$

Thouless criterion: the onset of superfluidity is signaled from the divergence of the vertex function at zero momentum and zero frequency. As we know when the inverse of the vertex function is zero, it means there is a bound state. Here we take into account the full Fermi sea, this is just the Cooper instability and the bound state is the Cooper pair.

$$\Gamma^{-1}(0,0) = \frac{m}{4\pi\hbar a_s} + \frac{\hbar}{V}\sum_{\mathbf{k}}[\chi_0(\mathbf{k};0) - \frac{1}{2\epsilon_{\mathbf{k}}}] = 0 \tag{1.19}$$

This gives us the gap equation at T_c when $(\Delta = 0)$. The reason why we take both the momentum and the frequency to be zero $\mathbf{q} = 0, iv_m = 0$, is that in this case $\sum_{\mathbf{k}}\chi_0(\mathbf{k};q)$ has the largest moduli, when the pairing occurs on the shell near the Fermi surface[27, 28].

1.3 Pseudogap Method

Using the Thouless criterion together with number conservation we can calculate the transition temperature for BCS-BEC crossover[29, 30]. In order to study the physics in superfluid phase, one way is to calculate the scattering process, the vertex function, in the symmetry-breaking phase[31, 32, 33]. Here I introduce another method which is called the pseudogap method[34, 35]. It gives a more clear description and although some approximations are made, it still catches most of the BCS-BEC physics.

Let us define the four dimensional form

$$\chi(q) = \frac{1}{V}\sum_{\mathbf{k}}[\chi_0(\mathbf{k};q) - \frac{1}{2\epsilon_{\mathbf{k}}}] \tag{1.20}$$

$$\Gamma(q) = \Gamma(\mathbf{q}, iv_m) \tag{1.21}$$

Here we only consider population balanced system.

$\Gamma^{-1}(0) = 0$ gives the gap equation. And in the superfluid region when $T \leq T_c$, the vertex function can be divided into two parts.

$$\Gamma(q) = \Gamma_{sc}(q) + \Gamma_{pg}(q) \tag{1.22}$$

where $\Gamma_{sc}(q)$ represents the condensed Cooper pairs part, $\Gamma_{pg}(q)$ represents pseudogap part which does not condense.

The superfluid vertex function and self energy are given, respectively, by

$$\begin{aligned}\Gamma_{sc}(q) &= -\beta\Delta_{sc}^2\delta(q) \\ \Sigma_{sc}(q) &= \frac{1}{\beta\hbar V}\sum_{q}\Gamma_{sc}(q)G_0(q-k) \\ &= -\frac{1}{\hbar}\Delta_{sc}^2 G_0(-k)\end{aligned} \tag{1.23}$$

This is consistent with BCS theory which gives

$$\begin{aligned} G_0(k) &= \frac{1}{iw_n - \frac{\xi_{\mathbf{k}}}{\hbar}} \\ G(k) &= \frac{u_{\mathbf{k}}^2}{iw_n - \frac{E_{\mathbf{k}}}{\hbar}} + \frac{v_{\mathbf{k}}^2}{iw_n + \frac{E_{\mathbf{k}}}{\hbar}} \\ &= \frac{iw_n + \frac{\xi_{\mathbf{k}}}{\hbar}}{(iw_n)^2 - \frac{E_{\mathbf{k}}^2}{\hbar^2}} \end{aligned} \tag{1.24}$$

where $E_{\mathbf{k}}^2 = \xi_{\mathbf{k}}^2 + \Delta_{sc}^2$. For this part, we consider the BCS pairing where the total momentum is zero. On the BCS side this part will form and condense at the same temperature. On the BEC side this part forms bound molecules and forms Bose-Einstein condensate at T_c. Similarly, the pseudogap vertex function and self energy are given, respectively, by

$$\Gamma_{pg}(q) = \frac{1}{\hbar}\frac{g}{1 + g\chi(q)} \tag{1.25}$$

$$\Sigma_{pg}(k) = \frac{1}{\beta\hbar V}\sum_q \Gamma_{pg}(q) G_0(q-k) \tag{1.26}$$

Due to the Thouless criterion, $\Gamma_{pg}(q)$ is highly peaked at $q = 0$, when $T \leq T_c$. We can introduce the approximation

$$\begin{aligned} \Sigma_{pg}(k) &\simeq [\frac{1}{\beta\hbar V}\sum_q \Gamma_{pg}(q)] G_0(-k) \\ &= -\frac{1}{\hbar}\Delta_{pg}^2 G_0(-k) \end{aligned} \tag{1.27}$$

where

$$\Delta_{pg}^2 \equiv -\frac{1}{\beta V}\sum_q \Gamma_{pg}(q) \tag{1.28}$$

For this part, its total momentum is not zero, it will form pairs but these pairs will never condense. This part is treated as pair fluctuation beyond mean field.

In all, the total pairing gap square is the combination of the BCS gap square and

the pseudogap square. we have

$$\begin{aligned} \Delta^2 &= \Delta_{sc}^2 + \Delta_{pg}^2 \\ E_{\mathbf{k}}^2 &= \xi_{\mathbf{k}}^2 + \Delta^2 \\ u_{\mathbf{k}}^2 &= \frac{1}{2}\frac{\xi_{\mathbf{k}} + E_{\mathbf{k}}}{E_{\mathbf{k}}} \\ v_{\mathbf{k}}^2 &= -\frac{1}{2}\frac{\xi_{\mathbf{k}} - E_{\mathbf{k}}}{E_{\mathbf{k}}} \end{aligned} \tag{1.29}$$

Finally we get

GAP equation

$$\Gamma^{-1}(0) = 0 \tag{1.30}$$

NUMBER equation

$$N = \frac{2}{\beta\hbar V}\sum_k G(k) \tag{1.31}$$

We use these two equations to get the total gap where the transition temperature relates to T^*.

PSEUDOGAP equation

$$\Delta_{pg}^2 = -\frac{1}{\beta V}\sum_q \Gamma_{pg}(q) \tag{1.32}$$

We use this equation to calculate the pseudogap. The real transition temperature T_c appears when

$$\Delta^2 = \Delta_{pg}^2 \tag{1.33}$$

This method catches the main physics in the BCS-BEC crossover and gives a qualitative picture both at zero temperature and above zero temperature.

1.4 Radio Frequency Experiment

The experimental signatures of fermionic pairing and superfluidity in ultracold gases of ^{40}K and ^{6}Li include measurements of the condensate momentum, density distribution [37, 38, 36], the pairing gap[39], and the observation of vortex lattices in rotating clouds[40]. Here we mainly introduce the observation of the pairing gap in a strongly interacting fermi gas using radio frequency spectroscopy(RF). This was first carried out in Rudolf Grimm's group in Innsbruck. They prepared their ultracold gas of fermionic ^{6}Li atoms in a balanced spin mixture of two lowest hyperfine states $|1\rangle$ and $|2\rangle$. A magnetic field B is applied for the Feshbach detuning through a broad resonance centered at $B_0 = 830G$. The superfluid state originates from pairings of atoms in states $|1\rangle$ and $|2\rangle$. Radio frequency(RF) fields are used for transferring atoms out of the superfluid state to a normal state. The field drives a transition from state $|2\rangle$ to an empty state $|3\rangle$ which is another hyperfine state and is not paired. This idea is closely related to observing the superconductor-normal metal current for electrons. It reflects the density of states and displays the excitation gap. The RF field detuning is $\delta = E_{RF} - (E_3 - E_2)$, where E_{RF}, E_3, and E_2 are the energies of the RF photon and of the states $|3\rangle$ and $|2\rangle$, respectively.

The radio frequency signal is shown by fractional loss in state $|2\rangle$ for various magnetic fields and temperatures. A signal of the pairing process is the emergence of a double-peak structure in the spectral response as a result for both the unpaired and paired atoms. When the temperature is high, there is no pairing, all the atoms in state $|2\rangle$ are unpaired and in normal state. This corresponds to a relatively narrow atomic peak at the original position in the spectra. When the temperature becomes lower, there appears another board peak which is located at a higher frequency. This is because energy is required for pair breaking. When temperature becomes even lower,

the unpaired narrow peak disappears. Now all the atoms in state $|2\rangle$ are paired.

In theory, transitions using the RF field is introduced as a perturbation and one can use the standard linear-response theory. A theoretic calculation using the method for two channel model and also adding the local density approximation can produce a similar picture[41]. On the BEC side, the energy difference between two peaks fails to be exactly the molecular binding energy but just relates to it, while on the BCS side it relates to the pairing gap.

This is called the first generation radio frequency experiment in ultracold fermions. The signal is averaged over the whole trap. The double peak structure may come from the trap inhomogeneity[42]. In the trap center, it is in superfluid phase while at the trap edge, due to small density, it is still in normal state. The first generation radio frequency experiment records both the signals from the trap center and edge.

Another phenomenon that will complicate the radio frequency spectrum is the final state effect. In above we have assumed state $|3\rangle$ is only connected to the system from radio frequency. As for ^6Li at magnetic field near $B_0 = 830G$, it is not the case. $|3\rangle$ has the big s-wave scattering length with state $|1\rangle$ and $|2\rangle$. So in modeling, we have to consider interactions between all three states, which makes the system complicated to handle[43, 44, 45, 46, 47, 48]. Fortunately, we can lessen the final state effect in some cases. For ^{40}K case, the final state effect is very small. For ^6Li, we can rearrange the experimental set up. For example, first make the superfluid state using state $|1\rangle$ and $|3\rangle$ and then use radio frequency to transport atoms from $|3\rangle$ to $|2\rangle$[49, 50]. In this way, the final state effect is small.

Complicated by the trap inhomogeneity and the final state effect, the first generation RF experiment is hard to interpret quantitatively. Then comes the second generation experiment. The JILA group use time-of-flight imaging to detect mo-

mentum distribution for state $|3\rangle$. In this way they get momentum resolved radio frequency spectroscopy[51, 52]. By varying momentum and detuning energy, they can get the graph for spectral function $A(k, w)$. Recently there is also proposal from their group that they can detect the signal only from trap center. In this way, they can get spectral function for a localized region, hence overcome the inhomogeneity problem.

Spatially resolved RF spectroscopy has been realized by the MIT group[53]. In their experiment, they use phase-contrast imaging to detect density differences between two hyperfine states. For example, if the RF field is shining along the y axis, they can get the two-dimensional density difference in the xz plane which has integrated density difference along the y axis. If there is cylindrical symmetry in the system along the z axis, one two-dimensional picture gives all the information. The three dimensional radial profile is calculated using the inverse Abel transformation from the two-dimensional profile. If there is no cylindrical symmetry along z axis, more two-dimensional information is needed along different directions in the xy plane. In this way, they can have the local radio frequency spectrum at each site. The spatial resolution is 1.4 um which is of the order of Fermi wavelength.

In chapter 2, we propose another measurement for the superfluid pairing. Furthermore, in chapter 4, we propose a modified RF experiment designed to allow direct determination of the local density of states.

Chapter 2

Detection of Fermi Pairing via Electromagnetically Induced Transparency

2.1 Introduction

A unique phenomenon of low temperature Fermi systems is the formation of correlated Fermi pairs when there is attractive interaction. How to detect pair formation in an indisputable fashion has remained a central problem in the study of ultracold atomic physics. Unlike the BEC transition of bosons for which the phase transition is accompanied by an easily detectable drastic change in atomic density profile, the onset of pairing in Fermi gases does not result in dramatic change that is measurable in fermion density. Early proposals sought the BCS pairing signature from the images of off-resonance scattered light [54, 55]. The underlying idea is that, in order to gain pairing information, measurement must go beyond the first-order coherence and, for example, use the density-density correlation. This is also the foundation for other detection methods such as spatial noise correlations in the image of the expanding gas [56], Bragg scattering [57, 58, 59, 60, 61, 62, 63], Raman spectroscopy [64, 65], Stokes scattering method [66], radio frequency (RF) spectroscopy [39, 41], optical detection of absorption [67], and interferometric method [68]. Among all these methods, RF spectroscopy [39, 41] has been the one of greatest use in current experiments [69, 70].

In this chapter, we propose an alternative detection scheme, whose principle of operation is illustrated in Fig. 2.1(a). In our scheme, we use two laser fields, a rela-

tively strong coupling and a weak probe laser field between the excited state $|e\rangle$ and, respectively, the ground state $|g\rangle$ and the spin up state $|\uparrow\rangle$, forming a Λ-type energy diagram, which facilitates the use of electromagnetically induced transparency (EIT) to determine the nature of pairing in the interacting Fermi gas of two hyperfine spin states: $|\uparrow\rangle$ and $|\downarrow\rangle$. EIT [71, 72] is defined as a probe laser field experiencing virtually no absorption but steep dispersion when operating around an atomic transition frequency. It has been at the forefront of many exciting developments in the field of quantum optics [73]. Such a phenomenon is based on quantum interference, which is absent in measurement schemes such as in Ref. [66], where lasers are tuned far away from single-photon resonance. In the context of ultracold atoms, an important example of EIT is the experimental demonstration of dramatic reduction of light speed in the EIT medium in the form of Bose condensate [74, 75]. This experiment has led to a renewed interest in EIT, motivated primarily by the prospect of the new possibilities that the slow speed and low intensity light may add to nonlinear optics [76] and quantum information processing [77, 78]. More recently, EIT has been used to spectroscopically probe ultracold Rydberg atoms [79]. In this chapter, we will show how EIT can be used to detect the nature of pairing in Fermi gases.

Before we go into detail, let us first compare the proposed EIT method with the RF spectroscopy method which is widely used nowadays in probing Fermi gases. In the RF experiment, an atomic sample is prepared and an RF pulse is applied to the sample which couples one of the pairing states, say state $|\uparrow\rangle$, to a third atomic level $|3\rangle$. This is followed by a destructive measurement of the transferred atom numbers using absorption laser imaging. The RF signal is defined as the average rate change of the population in state $|3\rangle$ during the RF pulse, which can be inferred from the measured loss of atoms in $|\uparrow\rangle$. This process is repeated for another RF

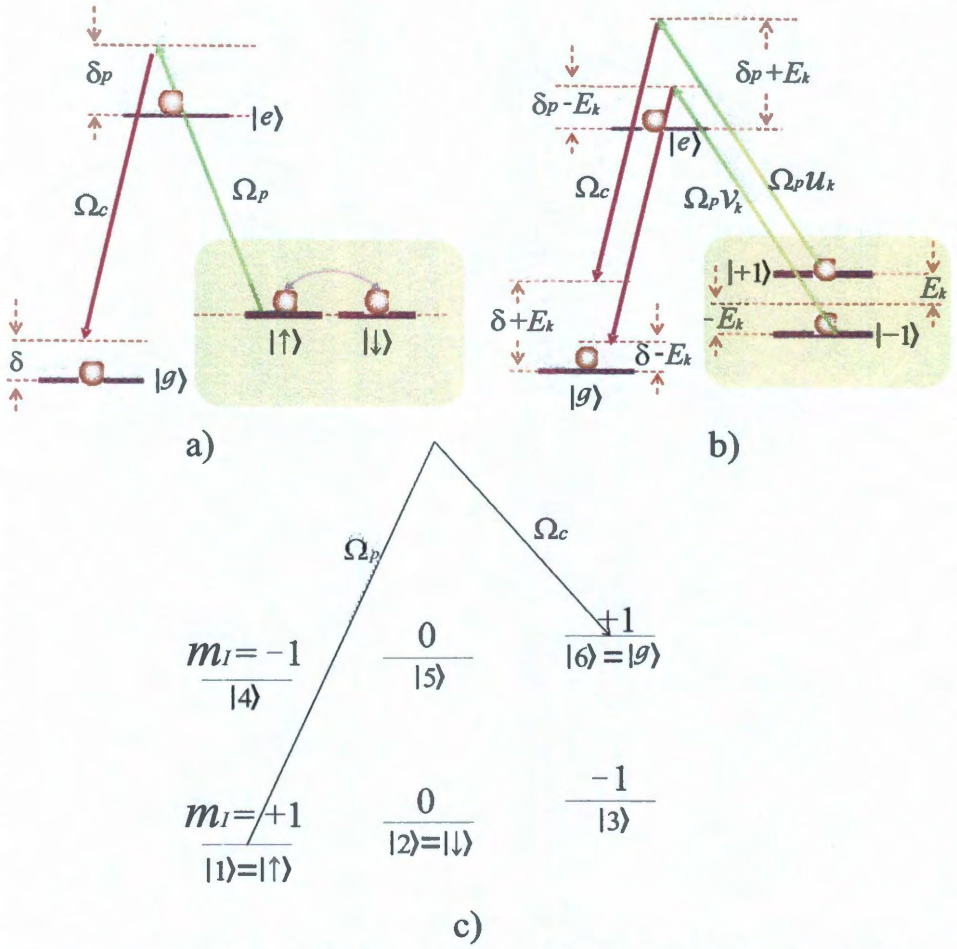

Figure 2.1 : (a) The bare state picture of our model. (b) The dressed state picture of our model equivalent to (a). (c) A possible realization in ^{6}Li. Here the states labelled by $|i\rangle$ $(i = 1, 2, ..., 6)$ are the 6 ground state hyperfine states. Most experiments involving ^{6}Li are performed with a magnetic field strength tuned near a Feshbach resonance at 834G. Under such a magnetic field, the magnetic quantum number for the nuclear spin m_I is, to a very good approximation, a good quantum number. The values of m_I are shown in the level diagrams. Two-photon transition can only occur between states with the same m_I. Any pair of the lower manifold ($|1\rangle$, $|2\rangle$, and $|3\rangle$) can be chosen to form the pairing states. In the example shown here, we choose $|1\rangle = |\uparrow\rangle$, $|2\rangle = |\downarrow\rangle$ and $|6\rangle = |g\rangle$. The excited state $|e\rangle$ (not shown) can be chosen properly as one of the electronic p state.

pulse with a different frequency. In addition to sparking many theoretical activities [43, 44, 45, 46, 47, 48], this method has recently been expanded into the imbalanced Fermi gas systems, where pairing can result in a number of interesting phenomena [80, 81]. A disadvantage of this method is its inefficiency: The sample must be prepared repeatedly for each RF pulse. In addition, as we mentioned in the first chapter, for the most commonly used fermionic atom species, i.e., ^{6}Li, the state $|3\rangle$ interacts strongly with the pairing states due to the fact that all three states involved have pairwise Feshbach resonances at relatively close magnetic field strengths. This leads to the so-called final state effect which greatly complicates the interpretation of the RF spectrum.

In the EIT method, by contrast, one can directly measure the absorption or transmission spectrum of the probe light. If we apply a frequency scan faster than the lifetime of the atomic sample to the weak probe field, the whole spectrum can be recorded continuously in a nearly non-destructive fashion to the atomic sample. Furthermore, the EIT signal results from quantum interference and is extremely sensitive to the two-photon resonance condition. The width of the EIT transparency window can be controlled by the coupling laser intensity and be made narrower than E_F. As we will show below, this property can be exploited to detect the onset of pairing as the pairing interaction shifts and destroys the two-photon resonance condition. In addition, due to different selection rules compared with the RF method, one can pick a different final state whose interaction with the pairing states are negligible [see Fig. 2.1(c)], hence avoiding the final state effects.

The chapter is organized as follows. In Sec. 2.2, we described the model under study and define the key quantity of the proposal — the absorption coefficient of the probe light. In Sec. 2.3, we present the expression of the probe absorption coef-

ficient and construct a quasiparticle picture that will become convenient to explain the features of the spectrum. In Sec. 2.4, we include the derivation of the pairing fluctuations in the framework of the pseudogap theory [35]. The results are presented in Sec. 2.5, where spectral features at different temperatures are explained. We also show how the EIT spectrum can be used to detect the onset of pairing.

2.2 Model

Let us now describe our model in more detail, beginning with the definition of ω_i and Ω_i as the temporal and Rabi frequencies of the probe ($i = p$) and coupling ($i = c$) laser field. The two laser fields have an almost identical wavevector $\mathbf{k}_L$ (along z direction). The system to be considered is a homogeneous one with a total volume V, and can thus be described by operators $\hat{a}_{\mathbf{k},i}$ ($\hat{a}^\dagger_{\mathbf{k},i}$) for annihilating (creating) a fermion in state $|i\rangle$ with momentum $\hbar\mathbf{k}$, and kinetic energy $\epsilon_k = \hbar^2 k^2/2m$, where m is the atomic mass. Here, $\hat{a}_{\mathbf{k},i}$ are defined in an interaction picture in which $\hat{a}_{\mathbf{k},e} = \hat{a}'_{\mathbf{k},e} e^{-i\omega_p t}$, $\hat{a}_{\mathbf{k},g} = \hat{a}'_{\mathbf{k},g} e^{i(\omega_c - \omega_p)t}$, and $\hat{a}_{\mathbf{k},\sigma} = \hat{a}'_{\mathbf{k},\sigma}$ ($\sigma = \uparrow, \downarrow$), where $\hat{a}'_{\mathbf{k},i}$ are the corresponding Schrödinger picture operators.

In a probe spectrum, the signal to be measured is the probe laser field, which is modified by a polarization having the same mathematical form as the probe field according to [82]

$$\frac{\partial \Omega_p}{\partial z} + \frac{1}{c}\frac{\partial \Omega_p}{\partial t} = i\frac{\mu_0 \omega_p c d_{e\uparrow}}{2} P_p \equiv \alpha \Omega_p \,, \tag{2.1}$$

where P_p is the slowly varying amplitude of that polarization, d_{ij} is the matrix element of the dipole moment operator between states $|i\rangle$ and $|j\rangle$, and μ_0 and c are the magnetic permeability and the speed of light in vacuum, respectively. The parameter α in Eq. (2.1) represents the complex absorption coefficient of the probe light [82]. By performing an ensemble average of the atomic dipole moment, we can express α

as

$$\alpha = i\frac{\alpha_0}{\Omega_p}\frac{1}{V}\sum_{\mathbf{k},\mathbf{q}}\left\langle \hat{a}^{\dagger}_{\mathbf{q},\uparrow}\hat{a}_{\mathbf{k}+\mathbf{k}_L,e}\right\rangle e^{i(\mathbf{k}-\mathbf{q})\cdot\mathbf{r}}, \tag{2.2}$$

where $\alpha_0 \equiv \mu_0\omega_p c\left|d_{e\uparrow}\right|^2$. The real and imaginary part of α correspond to the probe absorption spectrum and dispersion spectrum, respectively.

To determine the probe spectrum, we start from the grand canonical Hamiltonian $\hat{H} = \sum_{\mathbf{k}}\left(\hat{\mathcal{H}}_{1\mathbf{k}} + \hat{\mathcal{H}}_{2\mathbf{k}} + \hat{\mathcal{H}}_{3\mathbf{k}}\right)$, where

$$\begin{aligned}
\hat{\mathcal{H}}_{1\mathbf{k}} &= \left(\xi_k - \delta_p\right)\hat{a}^{\dagger}_{\mathbf{k},e}\hat{a}_{\mathbf{k},e} + \left(\xi_k - \delta\right)\hat{a}^{\dagger}_{\mathbf{k},g}\hat{a}_{\mathbf{k},g}\,,\\
\hat{\mathcal{H}}_{2\mathbf{k}} &= -\frac{1}{2}(\Omega_c\hat{a}^{\dagger}_{\mathbf{k}+\mathbf{k}_L,e}\hat{a}_{\mathbf{k},g} + \Omega_p\hat{a}^{\dagger}_{\mathbf{k}+\mathbf{k}_L,e}\hat{a}_{\mathbf{k},\uparrow}) - h.c\,,\\
\hat{\mathcal{H}}_{3\mathbf{k}} &= \sum_{\sigma}\xi_k\hat{a}^{\dagger}_{\mathbf{k},\sigma}\hat{a}_{\mathbf{k},\sigma} - (\Delta\hat{a}^{\dagger}_{\mathbf{k},\uparrow}\hat{a}^{\dagger}_{-\mathbf{k},\downarrow} + h.c)\,,
\end{aligned} \tag{2.3}$$

describe the bare atomic energies of states $|e\rangle$ and $|g\rangle$, the dipole interaction between atoms and laser fields, and the mean-field Hamiltonian for the spin up and down subsystem, respectively. Here, $\xi_k = \epsilon_k - \mu$ with μ being the chemical potential, $\delta_p = \hbar\left(\omega_p - \omega_{e\uparrow}\right)$ and $\delta_c = \hbar\left(\omega_c - \omega_{eg}\right)$ are the single-photon detunings, and $\delta = \delta_p - \delta_c$ is the two-photon detuning with ω_{ij} being the atomic transition frequency from level $|i\rangle$ to $|j\rangle$. In arriving at $\hat{\mathcal{H}}_{3\mathbf{k}}$, in order for the main physics to be most easily identified, we have expressed the collisions between atoms of opposite spins in terms of the gap parameter $\Delta = -UV^{-1}\sum_{\mathbf{k}}\langle\hat{a}_{-\mathbf{k},\downarrow}\hat{a}_{\mathbf{k},\uparrow}\rangle$ under the assumption of BCS paring, where U characterizes the contact interaction between $|\uparrow\rangle$ and $|\downarrow\rangle$ which, in the calculation, will be replaced in favor of the s-wave scattering length a_s via the regularization procedure:

$$\frac{m}{4\pi\hbar^2 a_s} = \frac{1}{U} + \frac{1}{V}\sum_{\mathbf{k}}\frac{1}{2\epsilon_k}\,. \tag{2.4}$$

A more complex model including the pseudo-gap physics [35] will be presented later in the chapter. Finally, we note that the effect of the collisions involving the final

state $|g\rangle$ in the RF spectrum has been a topic of much recent discussion. In our model, the spectra are not limited to the RF regime, and this may provide us with more freedom to choose $|g\rangle$ (and $|e\rangle$) that minimizes the final state effect. In what follows, for the sake of simplicity, we ignore the collisions involving states $|g\rangle$ (and $|e\rangle$). In practice, the effects of final state interaction can be minimized by choosing the proper atomic species [51] or hyperfine spin states [50]. In the example shown in Fig. 2.1(c), it is indeed expected that $|g\rangle$ does not interact strongly with either of the pairing state.

2.3 Quasiparticle Picture

The part of the Hamiltonian describing the pairing of the fermions can be diagonalized using the standard Bogoliubov transformation:

$$\begin{aligned} \hat{a}_{\mathbf{k},\uparrow} &= u_k \hat{\alpha}_{\mathbf{k},\uparrow} + v_k \hat{\alpha}^{\dagger}_{-\mathbf{k},\downarrow}\,, \\ \hat{a}^{\dagger}_{-\mathbf{k},\downarrow} &= -v_k \hat{\alpha}_{\mathbf{k},\uparrow} + u_k \hat{\alpha}^{\dagger}_{-\mathbf{k},\downarrow}\,, \end{aligned} \tag{2.5}$$

where $u_k = \sqrt{(E_k + \xi_k)/2E_k}, v_k = \sqrt{(E_k - \xi_k)/2E_k}$, and $E_k = \sqrt{\xi_{\mathbf{k}}^2 + \Delta^2}$ is the quasiparticle energy dispersion. Now we introduce two sets of quasiparticle states $|\pm 1_{\mathbf{k}}\rangle$, representing the electron and hole branches, respectively. The corresponding field operators are defined as

$$\hat{\alpha}_{\mathbf{k},+1} \equiv \hat{\alpha}_{\mathbf{k},\uparrow}\,, \quad \hat{\alpha}_{\mathbf{k},-1} \equiv \hat{\alpha}^{\dagger}_{-\mathbf{k},\downarrow}\,, \tag{2.6}$$

in terms of which, the grand canonical Hamiltonian can be written as

$$\hat{H} = \sum_{\mathbf{k}} \Big[(\xi_k - \delta_p)\, \hat{a}^{\dagger}_{\mathbf{k},e} \hat{a}_{\mathbf{k},e} + (\xi_k - \delta)\, \hat{a}^{\dagger}_{\mathbf{k},g} \hat{a}_{\mathbf{k},g} + E_k \hat{\alpha}^{\dagger}_{\mathbf{k},+1} \hat{\alpha}_{\mathbf{k},+1} - E_k \hat{\alpha}^{\dagger}_{\mathbf{k},-1} \hat{\alpha}_{\mathbf{k},-1}$$
$$- \left(\frac{\Omega_c}{2} \hat{a}^{\dagger}_{\mathbf{k}+\mathbf{k}_L,e} \hat{a}_{\mathbf{k},g} + h.c. \right) - \left(\frac{\Omega_p u_k}{2} \hat{a}^{\dagger}_{\mathbf{k}+\mathbf{k}_L,e} \hat{\alpha}_{\mathbf{k},+1} + h.c \right) - \left(\frac{\Omega_p v_k}{2} \hat{a}^{\dagger}_{\mathbf{k}+\mathbf{k}_L,e} \hat{\alpha}_{\mathbf{k},-1} + h.c \right) \Big] . \tag{2.7}$$

A physical picture emerges from this Hamiltonian very nicely. The state $|+1_{\mathbf{k}}\rangle$ ($|-1_{\mathbf{k}}\rangle$) has an energy dispersion $+E_k$ ($-E_k$) and is coupled to the excited state $|e\rangle$ by an effective Rabi frequency $\Omega_p u_k$ ($\Omega_p v_k$), which is now a function of k. In the quasiparticle picture, our model becomes a double Λ system as illustrated in Fig. 2.1(b). Let $+\Lambda$ ($-\Lambda$) denote the Λ configuration involving $|+1_{\mathbf{k}}\rangle$ ($|-1_{\mathbf{k}}\rangle$). The $+\Lambda$ ($-\Lambda$) system is characterized with a single-photon detuning of $\delta_p + E_k$ ($\delta_p - E_k$) and a two-photon detuning of $\delta + E_k$ ($\delta - E_k$). In thermal equilibrium at temperature T (in the absence of the probe field), we have

$$\langle \hat{\alpha}^{\dagger}_{\mathbf{k},+1} \hat{\alpha}_{\mathbf{k}',+1} \rangle = \delta_{\mathbf{k},\mathbf{k}'} - \langle \hat{\alpha}^{\dagger}_{\mathbf{k},-1} \hat{\alpha}_{\mathbf{k}',-1} \rangle = \delta_{\mathbf{k},\mathbf{k}'} f(E_k) , \tag{2.8}$$

where

$$f(\omega) = [\exp(\omega / k_B T) + 1]^{-1} , \tag{2.9}$$

is the standard Fermi-Dirac distribution for quasiparticles. Thus, as temperature increases from zero, the probability of finding a quasiparticle in state $|+1_{\mathbf{k}}\rangle$ increases while that in state $|-1_{\mathbf{k}}\rangle$ decreases but the total probability within each momentum group remains unchanged. Similarly, in the quasiparticle picture, the probe spectrum receives contributions from two transitions

$$\alpha = i \frac{\alpha_0}{\Omega_p} \frac{1}{V} \sum_{\mathbf{k},\mathbf{q}} e^{i(\mathbf{k}-\mathbf{q})\cdot\mathbf{r}} \times$$
$$[u_q \rho_{e,+1}(\mathbf{k}+\mathbf{k}_L, \mathbf{q}) + v_q \rho_{e,-1}(\mathbf{k}+\mathbf{k}_L, \mathbf{q})] , \tag{2.10}$$

where $\rho_{i,\pm1}(\mathbf{k},\mathbf{k}') = \left\langle \hat{\alpha}^{\dagger}_{\mathbf{k}',\pm1}\hat{a}_{\mathbf{k},i} \right\rangle$ are the off-diagonal density matrix elements in momentum space.

The equations for the density matrix elements can be obtained by averaging, with respect to the thermal equilibrium defined in Eq. (2.8), the corresponding Heisenberg's equations of motion based upon Hamiltonian (2.3). In the regime where the linear response theory holds, the terms at the second order and higher can be ignored, and the density matrix elements correct up to the first order in Ω_p are then found to be governed by the following coupled equations:

$$i\hbar\frac{d}{dt}\begin{bmatrix} \rho_{e,\eta}(\mathbf{k}+\mathbf{k}_L,\mathbf{q}) \\ \rho_{g,\eta}(\mathbf{k},\mathbf{q}) \end{bmatrix} = M_\eta \begin{bmatrix} \rho_{e,\eta}(\mathbf{k}+\mathbf{k}_L,\mathbf{q}) \\ \rho_{g,\eta}(\mathbf{k},\mathbf{q}) \end{bmatrix} - \frac{\Omega_p}{2}\Lambda_\eta(\mathbf{k})\,\delta_{\mathbf{k},\mathbf{q}},\ (\eta=\pm1), \tag{2.11}$$

where

$$\Lambda_{+1}(\mathbf{k}) = \begin{pmatrix} u_k f(E_k) \\ 0 \end{pmatrix}, \Lambda_{-1}(\mathbf{k}) = \begin{pmatrix} v_k f(-E_k) \\ 0 \end{pmatrix}, \tag{2.12}$$

and

$$M_\eta = \begin{bmatrix} \xi_k - \delta_p - \eta E_k - i\gamma & -\frac{\Omega_c}{2} \\ -\frac{\Omega_c^*}{2} & \xi_k - \delta - \eta E_k \end{bmatrix}. \tag{2.13}$$

Here we have introduced phenomenologically the parameter γ which represents the decay rate of the excited state $|e\rangle$. Inserting the steady-state solution from Eq. (2.11) into Eq. (2.10), we immediately arrive at $\alpha(\delta_c,\delta) = \alpha_{+1}(\delta_c,\delta) + \alpha_{-1}(\delta_c,\delta)$, where

$$\alpha_{\pm1}(\delta_c,\delta) = i\frac{\alpha_0}{2V}\sum_{\mathbf{k}} w_{\mathbf{k}}(\delta_c,\delta,\pm E_k)\, f(\pm E_k) \begin{cases} u_k^2 \\ v_k^2 \end{cases}, \tag{2.14}$$

with

$$w_{\mathbf{k}}(\delta_c,\delta,\omega) = \frac{\xi_k - \delta - \omega}{\lambda_{\mathbf{k}}(\delta_c,\delta,\omega)(\xi_k - \delta - \omega) - \left|\frac{\Omega_c}{2}\right|^2}, \tag{2.15}$$

and $\lambda_{\mathbf{k}}(\delta_c,\delta,\omega) = \xi_{\mathbf{k}+\mathbf{k}_L} - \delta_c - \delta - i\gamma - \omega$.

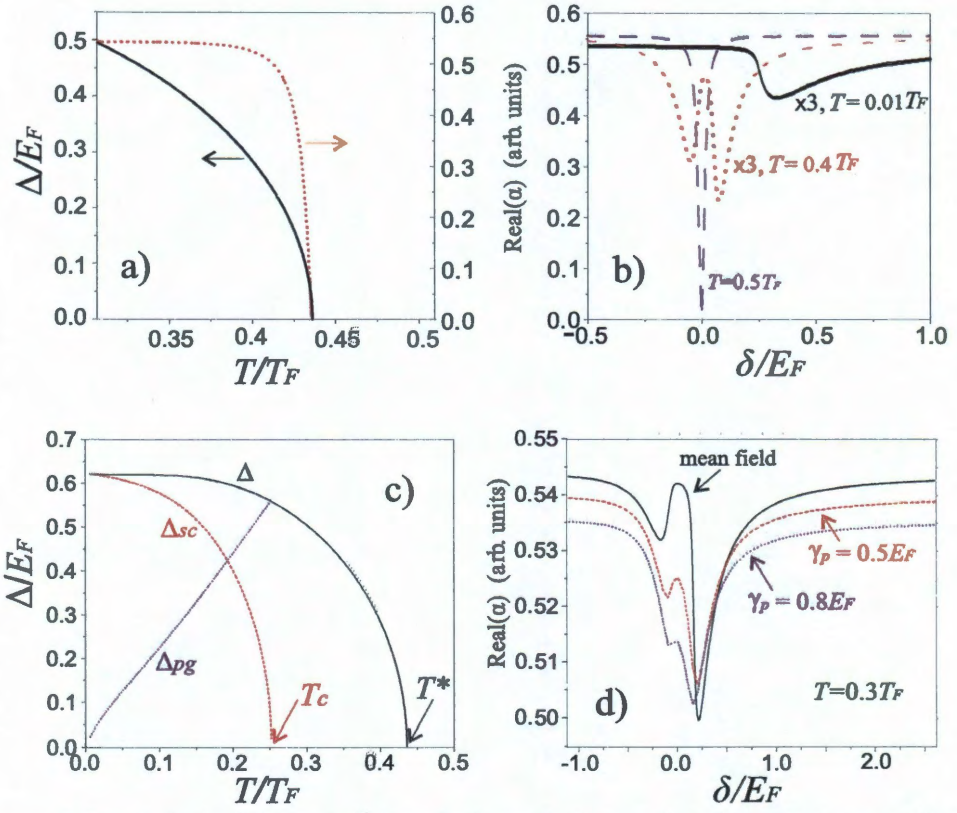

Figure 2.2 : (a) Δ (black solid curve) and the probe absorption coefficient real(α) at $\delta = 0$ (red dotted curve) as functions of T, obtained from the mean-field BCS theory. (b) Real(α) as a function of δ (absorption spectrum) at different T. (c) Δ, Δ_{sc} and Δ_{pg} as functions of T obtained from the pseudogap approach. ($\Delta_{sc} = 0$ and $\Delta = \Delta_{pg}$ when $T_c < T < T^*$). (d) A comparison of various absorption spectra at $T = 0.3T_F$. The parameters are $\delta_c = 0$, $\gamma = 380E_F$ ($\sim$ 10MHz), $\Omega_c = 5E_F$ ($\sim$ 0.1MHz), and $1/(k_F a_s) = -0.1$.

2.4 Pseudogap Picture

In this section, we generalize the result of Eq. (2.2) for α from the mean-field BCS pairing to a more realistic situation where pair fluctuations are included in the form of a pseudogap. The process uses the linear response theory [83] which is familiar in the field of condensed matter physics.

First, let us highlight the results of pseudogap theory [35] that are relevant to our EIT spectrum calculation. When pairing fluctuations at finite temperature are included in the framework of the pseudogap model [35], the BCS gap equation and number equation are still valid. However, the gap Δ is now regarded as the total gap divided into a BCS gap Δ_{sc} for condensed (BCS) pairs below T_c and a pseudogap Δ_{pg} for preformed (finite momentum) pairs:

$$\Delta^2 = \Delta_{sc}^2 + \Delta_{pg}^2 . \tag{2.16}$$

The onset of the total gap Δ occurs at temperature T^*, which is greater than T_c. The system with preformed pairs is described by the Green's function

$$G^{-1}(\mathbf{k}, iw_n) = G_0^{-1}(\mathbf{k}, iw_n) - \Sigma(\mathbf{k}, iw_n), \tag{2.17}$$

where the non-interacting Green's function

$$G_0(\mathbf{k}, iw_n) = (i\omega_n - \xi_{\mathbf{k}})^{-1} , \tag{2.18}$$

and the self energy

$$\begin{aligned} \Sigma(\mathbf{k}, iw_n) &= \Sigma_{sc}(\mathbf{k}, iw_n) + \Sigma_{pg}(\mathbf{k}, iw_n) \\ &= \frac{\Delta_{sc}^2}{iw_n + \xi_k} + \frac{\Delta_{pg}^2}{iw_n + \xi_k + i\gamma_p} , \end{aligned} \tag{2.19}$$

with w_n being the Fermi Matsubara frequency and γ_p^{-1} the finite lifetime of pseudogap pairs. The spectral function $A(\mathbf{k}, \omega)$ can be obtained from the Green's function via

the relation

$$A(\mathbf{k},\omega) = -2\,\mathrm{Im}\,G\left(\mathbf{k},\omega+i0^{+}\right), \tag{2.20}$$

which, with the help of Eqs. (2.17), (2.18), and (2.19), is found to be given by

$$A(\mathbf{k},\omega) = \frac{2(\omega+\xi_k)^2\gamma_p\Delta_{pg}^2}{[\omega^2-E_k^2]^2(\omega+\xi_k)^2+\gamma_p^2[\omega^2-E_k^{sc2}]^2}, \tag{2.21}$$

where $E_k^{sc}=\sqrt{{\xi_k}^2+\Delta_{sc}^2}$. In the limit of $\gamma_p\to 0$ and $E_k^{sc}\to E_k$, we recover from Eq. (2.21) the spectral function under the BCS paring

$$A(\mathbf{k},w) = 2\pi[u_k^2\delta(\omega-E_k)+v_k^2\delta(\omega+E_k)]. \tag{2.22}$$

In order to use the linear response theory, we first divide our system into a "left part" comprising two hyperfine spin states: $|\uparrow\rangle$ and $|\downarrow\rangle$, a "right part" consisting of the coupling laser field and states $|g\rangle$ and $|e\rangle$, described by the Hamiltonian

$$\begin{aligned}\hat{H}_R = &\sum_{\mathbf{k}}\left[(\xi_k-\delta_p)\hat{a}^{\dagger}_{\mathbf{k},e}\hat{a}_{\mathbf{k},e}+(\xi_k-\delta)\hat{a}^{\dagger}_{\mathbf{k},g}\hat{a}_{\mathbf{k},g}\right]\\ &-\left(\frac{\Omega_c}{2}\sum_{k}\hat{a}^{\dagger}_{\mathbf{k}+\mathbf{k}_L,e}\hat{a}_{\mathbf{k},g}+h.c.\right),\end{aligned} \tag{2.23}$$

and finally the coupling between the two parts induced by the probe field, described by the tunneling Hamiltonian

$$\begin{aligned}\hat{H}_T &= -\frac{\Omega_p}{2}\sum_{\mathbf{k}}\hat{a}^{\dagger}_{\mathbf{k}+\mathbf{k}_L,e}\hat{a}_{\mathbf{k},\uparrow}+h.c\\ &\equiv \hat{A}+\hat{A}^{\dagger}.\end{aligned} \tag{2.24}$$

Next, we change H_R into a diagonal form

$$H_R = \sum_{\mathbf{k}}\left[E_k^{\alpha}\hat{\alpha}^{\dagger}_{\mathbf{k}}\hat{\alpha}_{\mathbf{k}}+E_k^{\beta}\hat{\beta}^{\dagger}_{\mathbf{k}}\hat{\beta}_{\mathbf{k}}\right], \tag{2.25}$$

in terms of a pair of dressed state operators, $\hat{\alpha}$ and $\hat{\beta}$, defined via the transformation

$$\begin{bmatrix}\hat{a}_{\mathbf{k}+\mathbf{k}_L,e}\\ \hat{a}_{\mathbf{k},g}\end{bmatrix} = \begin{bmatrix}u_k^{\alpha} & u_k^{\beta}\\ v_k^{\alpha} & v_k^{\beta}\end{bmatrix}\begin{bmatrix}\hat{\alpha}_{\mathbf{k}}\\ \hat{\beta}_{\mathbf{k}}\end{bmatrix}, \tag{2.26}$$

where

$$(u_k^{\alpha,\beta})^2 = (v_k^{\beta,\alpha})^2 = \frac{1}{2}\left(1 \pm \frac{\zeta_k - \eta_k}{\sqrt{(\zeta_k - \eta_k)^2 + |\Omega_c|^2}}\right), \tag{2.27}$$

$$E_k^{\alpha,\beta} = \frac{1}{2}\left(\zeta_k + \eta_k \pm \sqrt{(\zeta_k - \eta_k)^2 + |\Omega_c|^2}\right), \tag{2.28}$$

with $\zeta_k = \xi_{k+k_L} - \delta_p$ and $\eta_k = \xi_k - \delta$. In terms of the dressed state operators, $\hat{A}$ becomes

$$\hat{A} = -\frac{\Omega_p}{2}\sum_{\mathbf{k}}\left[u_k^{\alpha}\hat{\alpha}_{\mathbf{k}}^{\dagger}\hat{a}_{\mathbf{k},\uparrow} + u_k^{\beta}\hat{\beta}_{\mathbf{k}}^{\dagger}\hat{a}_{\mathbf{k},\uparrow}\right] \tag{2.29}$$

and is in a form to which the linear response theory [83] is directly applicable. Following the standard practice, we then find

$$\langle\hat{A}\rangle = \frac{\Omega_p^2}{4}\sum_{\mathbf{k}}\sum_{\eta=\alpha,\beta}(u_k^{\eta})^2\int_{-\infty}^{+\infty}\frac{d\omega_L}{2\pi}A_L(\mathbf{k},\omega_L)$$
$$\int_{-\infty}^{+\infty}\frac{d\omega_R}{2\pi}A_R^{\eta}(\mathbf{k},\omega_R)\frac{f(\omega_R) - f(\omega_L)}{\omega_R - \omega_L + i0^+}. \tag{2.30}$$

In Eq. (2.30), $A_L(\mathbf{k},\omega_L)$ is same as $A(\mathbf{k},\omega_L)$ defined in Eq. (2.21), while $A_R^{\eta}(\mathbf{k},\omega_R)$ is given by $2\pi\delta\left(\omega_R - E_k^{\eta}\right)$ because the right part is in a normal state described by the Green's function $G_{\eta}^{-1}\left(\mathbf{k}, iw_n\right) = iw_n - E_k^{\eta}$. Integrating over ω_R, we change Eq. (2.30) into

$$\langle\hat{A}\rangle = \frac{\Omega_p^2}{4}\sum_{\mathbf{k}}\sum_{\eta=\alpha,\beta}(u_k^{\eta})^2\int_{-\infty}^{+\infty}\frac{d\omega}{2\pi}A(\mathbf{k},\omega)\frac{f(E_k^{\eta}) - f(\omega)}{E_k^{\eta} - \omega + i0^+}, \tag{2.31}$$

where the dummy variable ω_L has been changed into ω. We now include the effect of the decay of the excited state phenomenologically by replacing δ_p with $\delta_p - i\gamma$. We see that E_k^{η} now becomes imaginary which signals the inability of the dressed states to hold populations. This along with the fact that the dressed states here are the superpositions of the initially empty states provide us with the justification to set

$f(E_k^\eta) = 0$ in Eq. (2.31). With these considerations, we finally arrive at

$$\langle \hat{A} \rangle = -\frac{\Omega_p^2}{4} \sum_{\mathbf{k}} \int_{-\infty}^{+\infty} \frac{d\omega}{2\pi} A(\mathbf{k}, \omega) f(\omega) w_{\mathbf{k}} (\delta_c, \delta, \omega) \tag{2.32}$$

where the use of Eqs. (2.27) and (2.28) is made. It is clear that α is proportional to $i\langle A \rangle$ in Eq. (2.32).

2.5 Results

Fig. 2.2(a) and (b) shows examples of the probe absorption coefficient, Re(α). For the results shown in this chapter, we choose $1/(k_F a_s) = -0.1$ where we denote that E_F, k_F, and $T_F = E_F/k_B$ be the Fermi energy, Fermi wavenumber, and Fermi temperature, respectively, for the non-interacting case. The black solid line in Fig. 2.2(a) represents the gap parameter in the mean-field calculation, from which we can see that the critical temperature below which the system exhibits pairing is given by $T_c = 0.435 T_F$ for the parameters chosen. The dotted red curve in Fig. 2.2(a) represents the absorption coefficient at two-photon resonance $\delta = 0$. We can see that it remains at zero for $T > T_c$ but increases sharply once the temperature drops below T_c. We note that this feature can be used as a sensitive gauge for detecting the onset of Fermi pairing. With this being emphasized, we now turn to explain the main spectroscopic features displayed in Fig. 2.2(b).

First, as long as $T > T_c$ where $\Delta = 0$, one can show that the spectrum is essentially independent of T and

$$\mathrm{Re}(\alpha) \propto \frac{\delta^2}{[(\delta + \delta_c)\delta - |\Omega_c/2|^2]^2 + \delta^2 \gamma^2} \,. \tag{2.33}$$

From this expression, one can easily see that there exists around $\delta = 0$ a narrow transparency window with a width determined by the optical pumping rate $\Gamma_{op} =$

$|\Omega_c|^2 \gamma / [4(\delta_c^2 + \gamma^2)]$ [see the blue dashed curve for $T = 0.5T_F$ in Fig. 2.2(b)]. So for normal gas there is electromagnetically induced transparency. This feature can be most easily understood from the bare state picture [Fig. 2.1(a)], where state $|\uparrow\rangle$ is decoupled from state $|\downarrow\rangle$ so that the spectrum is of EIT type for a Λ system involving $|e\rangle$, $|g\rangle$, and $|\uparrow\rangle$. Further, because states $|g\rangle$ and $|\uparrow\rangle$ share the same energy dispersion ξ_k, the two-photon resonance condition $\delta = 0$ holds for atoms of any velocity groups; the absence of absorption at $\delta = 0$ signals the existence of a coherent population trapping state.

As T decreases below T_c, transparency is broken and a double-peak structure develops [see the red dotted line for $T = 0.4T_F$ in Fig. 2.2(b)]. The two peaks can be understood as contributed by the quasiparticle state $|+1_{\mathbf{k}}\rangle$ and $|-1_{\mathbf{k}}\rangle$, respectively. In the limit where T is far below T_c [see the black solid line for $T = 0.01T_F$ in Fig. 2.2(b)], $+\Lambda$ system has negligible contribution to the probe spectrum because there exist virtually no quasiparticles in state $|+1_{\mathbf{k}}\rangle$. Thus, the spectrum is solely contributed by the $-\Lambda$ system, resulting in a single-peak structure. However, unlike the situations above T_c, and though the dispersion of an atom in state $|g\rangle$ continues to be ξ_k, the dispersion of a dressed particle in state $|-1_{\mathbf{k}}\rangle$ is $-E_k$. As a result, the effective two-photon resonance condition $\xi_k - \delta + E_k = 0$ is now momentum dependent. Aside from a shift, the transparency window becomes inhomogeneously broadened with a linewidth on the order of E_F. A consequence of the momentum-dependence of the two-photon resonance condition is that, for any given probe laser frequency, only atoms with the 'right' momentum result in perfect destructive quantum interference. Consequently, $\mathrm{Re}(\alpha)$ can no longer be zero for any probe frequency. This underlies the sharp increase of the probe absorption at $\delta = 0$ below T_c as shown in Fig. 2.2(a).

We also want to emphasize that the spectrum shown in Fig. 2.2(b) can be obtained

by scanning the probe laser frequency over a range on the order of $E_F \sim 0.1$MHz. We may take typical spectral features of the Fermi gas to be $\delta\omega \sim 0.1E_F \sim 10$KHz. To resolve such features, using the energy-time uncertainty relation, we can use a scan rate of 10KHz/0.1ms, then the total scan time can be estimated to be around 1 ms. As this time is much shorter compared with the typical lifetime of the Fermi gas, this method can be regarded as nearly non-destructive. This demonstrates the great efficiency of the EIT probe.

In a more realistic model where pair fluctuations are included, the gap Δ is divided into a BCS gap Δ_{sc} for condensed (BCS) pairs below T_c and a pseudogap Δ_{pg} for preformed (finite momentum) pairs below temperature T^* according to $\Delta^2 = \Delta_{sc}^2 + \Delta_{pg}^2$ [35]. Results including pseudogap physics are illustrated in Fig. 2.2(c) and (d). In contrast to the weakly interacting regime, where T^* is virtually the same as T_c, T^* is much higher than T_c in strongly interacting regime as is clearly the case of present study according to Fig. 2.2(c). It needs to be stressed that pair fluctuations can result in a finite lifetime γ_p^{-1} for preformed pairs which tends to broaden the spectral features, so that only when γ_p is sufficiently small can the double-peak spectroscopic structure be resolved as Fig. 2.2(d) demonstrates. Finally, the two-photon resonance here is only sensitive to Δ because E_k depends on the total gap Δ [35]. As a result, like its RF counterpart, the EIT method cannot distinguish between Δ_{sc} and Δ_{pg}. However, the qualitative features of Fig. 2.2(a) are not changed as long as we regard the corresponding critical temperature as T^*.

Chapter 3

Rashba Spin-Orbit Coupled Atomic Fermi Gases

3.1 Introduction

Since its recent realization in cold atomic systems [84, 85, 86, 87, 88], the artificial gauge field has received tremendous attention. The concept of a gauge field is ubiquitous, a classical example of which is electromagnetism. In NIST experiments, they used a pair of Raman lasers to couple different hyperfine states in a ^{87}Rb atom together with an external Zeeman field to split hyperfine states energy levels. By changing the properties of laser beams and the Zeeman field, they could get a uniform vector gauge field[84], synthetic magnetic field[85], synthetic electric field[86] and synthetic non-abelian gauge field in the form of spin-orbit coupling[87]. The achievement of the above mentioned experiments allows us to simulate charged particles moving in electromagnetic fields using neutral atoms. The more recent realization of a non-Abelian gauge field in a system of ^{87}Rb condensate [87] provides us a system of spinor quantum gas whose internal (pseudo-)spin degrees of freedom and external spatial degrees of freedom are intimately coupled. Novel quantum states will emerge in such spin-orbit coupled systems [89]. Although experiments on artificial gauge fields have so far only been carried out in bosonic systems, we have no reason to doubt that they will soon be extended to fermionic systems. Theoretically, there have been a number of papers focusing on the interesting properties of spin-orbit coupled Fermi gases [90, 91, 92, 93, 94, 95, 96, 97, 98, 99, 100, 101, 102].

The salient features of spin-orbit coupled fermions include: enhanced pairing field [91, 92, 95], mixed spin pairing [103], non-trivial topological order [95, 104], and possible existence of Majorana fermion [105], etc. The purpose of the chapter is to provide a detailed description of the theoretical techniques and by including the effect of a Zeeman field which not only breaks the population balance, but also may induce topological phase transitions in the system. We start from a discussion of the two-body problem, followed by a detailed study of the many-body system. We present our calculations of various important physical observables such as the single-particle spectrum, density of states, spin structure factors, etc., which may be used to characterize the system experimentally.

3.2 Model and General Technique

In this section, we first present the model Hamiltonian of interest and then give a detailed description of the functional integral formalism employed in deriving the relevant equations. We choose this formalism as it allows us to present a unified treatment for both the two-body and the many-body physics.

3.2.1 Model Hamiltonian

Here we consider the BEC-BCS crossover theory in the presence of the spin-orbit (SO) coupling, together with an external Zeeman field $h\hat{\sigma}_z$. The spin-orbit coupling is Rashba type in the $x-y$ plane, which has the from $\lambda(\hat{k}_y\hat{\sigma}_x - \hat{k}_x\hat{\sigma}_y)$. Here the Pauli matrix $\hat{\sigma}_i$ $(i = 0, x, y, z)$ describes the spin degrees of freedom. The momentum $\hat{k}_\alpha$ $(\alpha = x, y, z)$ should be regarded as the operators in real space. The Zeeman field acts as the chemical potential difference which breaks the population balance between the two spin components of the fermions. The second-quantized Hamiltonian for a uniform system reads,

$$\begin{aligned}\mathcal{H} &= \int d\mathbf{r}\left\{\psi^{+}\left[\xi_{\mathbf{k}} + h\hat{\sigma}_z + \lambda(\hat{k}_y\hat{\sigma}_x - \hat{k}_x\hat{\sigma}_y)\right]\psi\right. \\ &\left. + U_0\psi_{\uparrow}^{+}(\mathbf{r})\,\psi_{\downarrow}^{+}(\mathbf{r})\,\psi_{\downarrow}(\mathbf{r})\,\psi_{\uparrow}(\mathbf{r})\right\}, \qquad (3.1)\end{aligned}$$

where $\xi_{\mathbf{k}} = \hbar^2\hat{k}^2/(2m) - \mu$ with μ being the chemical potential, and $\psi(\mathbf{r}) = [\psi_{\uparrow}(\mathbf{r}), \psi_{\downarrow}(\mathbf{r})]^T$, $\psi_\sigma(\mathbf{r})$ is the fermionic annihilation operator for spin-σ atom. Here h is the strength of the Zeeman field and λ is the Rashba SO coupling constant. Without loss of generality, we take both h and λ to be non-negative. The last term in Eq. (3.1) represents the two-body contact s-wave interaction between un-like spins.

3.2.2 Functional Integral Method

We employ the functional integral method [106, 107, 32, 23] to study the problem. The reason to use the functional integral method is that it directly calculates the partition function and thermodynamical potential which are directly related to experimental quantities. Also it naturally introduces the pairing order parameter and provides a systematic way of treating fluctuation. The partition function is given by,

$$\mathcal{Z} = \int \mathcal{D}[\psi(\mathbf{r},\tau), \bar{\psi}(\mathbf{r},\tau)] \exp\left\{-S\left[\psi(\mathbf{r},\tau), \bar{\psi}(\mathbf{r},\tau)\right]\right\}, \tag{3.2}$$

where the action

$$S\left[\psi,\bar{\psi}\right] = \int_0^\beta d\tau \left[\int d\mathbf{r} \sum_\sigma \bar{\psi}_\sigma(\mathbf{r},\tau)\,\partial_\tau \psi_\sigma(\mathbf{r},\tau) + \mathcal{H}\left(\psi,\bar{\psi}\right)\right]. \tag{3.3}$$

is written as an integral over imaginary time τ. Here $\beta = 1/(k_B T)$ is the inverse temperature and $\mathcal{H}\left(\psi,\bar{\psi}\right)$ is obtained by replacing the field operators ψ^+ and ψ with the Grassmann variables $\bar{\psi}$ and ψ, respectively. We can use the Hubbard-Stratonovich transformation to transform the quartic interaction term into the quadratic form as:

$$e^{-U_0 \int dx d\tau \bar{\psi}_\uparrow \bar{\psi}_\downarrow \psi_\downarrow \psi_\uparrow} = \int \mathcal{D}\left[\Delta,\bar{\Delta}\right] \exp\left\{\int_0^\beta d\tau \int d\mathbf{r} \left[\frac{|\Delta(\mathbf{r},\tau)|^2}{U_0} + \left(\bar{\Delta}\psi_\downarrow\psi_\uparrow + \Delta\bar{\psi}_\uparrow\bar{\psi}_\downarrow\right)\right]\right\}, \tag{3.4}$$

from which the pairing field $\Delta(\mathbf{r},\tau)$ is introduced.

Let us now formally introduce the 4-dimensional Nambu spinor $\Phi(\mathbf{r},\tau) \equiv [\psi_\uparrow, \psi_\downarrow, \bar{\psi}_\uparrow, \bar{\psi}_\downarrow]^T$ and rewrite the action as,

$$\begin{aligned}\mathcal{Z} = \int \mathcal{D}[\Phi,\bar{\Phi};\Delta,\bar{\Delta}] \exp\Bigg\{ &- \int d\tau \int d\mathbf{r} \int d\tau' \int d\mathbf{r}' \left[-\frac{1}{2}\bar{\Phi}(\mathbf{r},\tau)\mathcal{G}^{-1}\Phi(\mathbf{r}',\tau')\right. \\ &\left. - \frac{|\Delta(\mathbf{r},\tau)|^2}{U_0}\delta(\mathbf{r}-\mathbf{r}')\delta(\tau-\tau')\right] - \frac{\beta}{V}\sum_{\mathbf{k}}\xi_{\mathbf{k}}\Bigg\},\end{aligned} \tag{3.5}$$

where V is the quantization volume and the single-particle Green function is given by,

$$\mathcal{G}^{-1} = \begin{bmatrix} -\partial_\tau - \xi_{\mathbf{k}} - h\hat{\sigma}_z - \lambda(k_y\hat{\sigma}_x - k_x\hat{\sigma}_y) & i\Delta\hat{\sigma}_y \\ -i\bar{\Delta}\hat{\sigma}_y & -\partial_\tau + \xi_{\mathbf{k}} + h\hat{\sigma}_z - \lambda(k_y\hat{\sigma}_x + k_x\hat{\sigma}_y) \end{bmatrix} \delta(\mathbf{r}-\mathbf{r}')\delta(\tau-\tau'), \tag{3.6}$$

Integrating out the original fermionic fields, we may rewrite the partition function as

$$\mathcal{Z} = \int \mathcal{D}[\Delta,\bar{\Delta}] \exp\left\{-S_{\text{eff}}\left[\Delta,\bar{\Delta}\right]\right\}, \tag{3.7}$$

where the effective action is given by

$$\begin{aligned} S_{\text{eff}}\left[\Delta,\bar{\Delta}\right] &= \int_0^\beta d\tau \int d\mathbf{r} \left\{-\frac{|\Delta(\mathbf{r},\tau)|^2}{U_0}\right\} \\ &\quad -\frac{1}{2}\text{Tr}\ln\left[-\mathcal{G}^{-1}\right] + \frac{\beta}{V}\sum_{\mathbf{k}}\xi_{\mathbf{k}}. \end{aligned} \tag{3.8}$$

where the trace is over all the spin, spatial, and temporal degrees of freedom. We expand $\Delta(\mathbf{r},\tau) = \Delta_0 + \delta\Delta(\mathbf{r},\tau)$. To proceed, we restrict to the gaussian fluctuation. The effective action is then decomposed accordingly as $S_{\text{eff}} = S_0 + \Delta S$, where the saddle-point action is

$$S_0 = \int_0^\beta d\tau \int d\mathbf{r} \left(-\frac{\Delta_0^2}{U_0}\right) - \frac{1}{2}\text{Tr}\ln\left[-\mathcal{G}_0^{-1}\right] + \frac{\beta}{V}\sum_{\mathbf{k}}\xi_{\mathbf{k}}, \tag{3.9}$$

where $\mathcal{G}_0^{-1}$ has the same form as $\mathcal{G}^{-1}$ in Eq. (3.6) with Δ replaced by Δ_0, and the fluctuating action takes the form

$$\Delta S = \int_0^\beta d\tau \int d\mathbf{r} \left\{-\frac{|\delta\Delta(\mathbf{r},\tau)|^2}{U_0} + \frac{1}{2}\left(\frac{1}{2}\right)\text{Tr}\left(\mathcal{G}_0\Sigma\right)^2\right\},$$

with

$$\Sigma = \begin{pmatrix} 0 & i\delta\Delta\hat{\sigma}_y \\ -i\delta\bar{\Delta}\hat{\sigma}_y & 0 \end{pmatrix}. \tag{3.10}$$

being the self energy.

3.2.3 Vertex Function

The low-energy effective two-body interaction is characterized by the vertex function, which we derive in this section. At the gaussian fluctuation level, the vertex function corresponds to atom multiple scattering in the particle-particle channel which is represented by the ladder diagrams introduced in sec. 1.2. We shall consider the normal state where the pairing field vanishes, i.e., $\Delta_0 = 0$. In this case, the inverse Green function $\mathcal{G}_0^{-1}$ has a diagonal form and can be easily inverted to give :

$$\mathcal{G}_0(k) = \begin{pmatrix} \hat{g}_+(k) & 0 \\ 0 & \hat{g}_-(k) \end{pmatrix}, \tag{3.11}$$

where $k \equiv (\mathbf{k}, i\omega_m)$ and

$$\begin{aligned} \hat{g}_+(k) &= \frac{1}{i\omega_m - \xi_{\mathbf{k}} - h\hat{\sigma}_z - \lambda(k_y\hat{\sigma}_x - k_x\hat{\sigma}_y)} \\ &= \frac{i\omega_m - \xi_{\mathbf{k}} + h\hat{\sigma}_z + \lambda(k_y\hat{\sigma}_x - k_x\hat{\sigma}_y)}{(i\omega_m - \xi_{\mathbf{k}})^2 - \left[h^2 + \lambda^2\left(k_x^2 + k_y^2\right)\right]}, \end{aligned} \tag{3.12}$$

$$\begin{aligned} \hat{g}_-(k) &= \frac{1}{i\omega_m + \xi_{\mathbf{k}} + h\hat{\sigma}_z - \lambda(k_y\hat{\sigma}_x + k_x\hat{\sigma}_y)} \\ &= \frac{i\omega_m + \xi_{\mathbf{k}} - h\hat{\sigma}_z + \lambda(k_y\hat{\sigma}_x + k_x\hat{\sigma}_y)}{(i\omega_m + \xi_{\mathbf{k}})^2 - \left[h^2 + \lambda^2\left(k_x^2 + k_y^2\right)\right]}. \end{aligned} \tag{3.13}$$

After some algebra, we may obtain the fluctuating part of the action as

$$\Delta S = k_B T \frac{1}{V} \sum_{q=\mathbf{q}, i\nu_n} \left[-\Gamma^{-1}(q)\right] \delta\Delta(q)\delta\bar{\Delta}(q), \tag{3.14}$$

where the inverse vertex function is given by

$$\begin{aligned} \Gamma^{-1}(q) &= \frac{1}{U_0} + k_B T \frac{1}{V} \sum_{\mathbf{k}, i\omega_m} \left[\frac{1/2}{(i\omega_m - \epsilon_{\mathbf{k},+})(i\nu_n - i\omega_m - \epsilon_{\mathbf{q}-\mathbf{k},+})} \right. \\ &\left. + \frac{1/2}{(i\omega_m - \epsilon_{\mathbf{k},-})(i\nu_n - i\omega_m - \epsilon_{\mathbf{q}-\mathbf{k},-})} - A_{res} \right], \end{aligned} \tag{3.15}$$

where $\epsilon_{\mathbf{k},\pm}$ are the single-particle spectrum $\epsilon_{\mathbf{k},\pm} = \xi_{\mathbf{k}} \pm \sqrt{h^2 + \lambda^2 k_\perp^2}$ and

$$A_{res} = \frac{\sqrt{h^2+\lambda^2 k_\perp^2}\sqrt{h^2+\lambda^2\left(\mathbf{q}-\mathbf{k}\right)_\perp^2} + h^2 + \lambda^2 k_x\left(q_x - k_x\right) + \lambda^2 k_y\left(q_y - k_y\right)}{\left(i\omega_m - \epsilon_{\mathbf{k},+}\right)\left(i\omega_m - \epsilon_{\mathbf{k},-}\right)\left(i\nu_n - i\omega_m - \epsilon_{\mathbf{q}-\mathbf{k},+}\right)\left(i\nu_n - i\omega_m - \epsilon_{\mathbf{q}-\mathbf{k},-}\right)}. \tag{3.16}$$

The summation over $i\omega_m$ in Eq. (3.15) can be done explicitly, after which we find that,

$$\begin{aligned}\Gamma^{-1}(q) &= \frac{m}{4\pi\hbar^2 a_s} + \frac{1}{2V}\sum_{\mathbf{k}}\left[\frac{f\left(\epsilon_{\mathbf{q}/2+\mathbf{k},+}\right) + f\left(\epsilon_{\mathbf{q}/2-\mathbf{k},+}\right) - 1}{i\nu_n - \epsilon_{\mathbf{q}/2+\mathbf{k},+} - \epsilon_{\mathbf{q}/2-\mathbf{k},+}}\right. \\ &\quad \left. + \frac{f\left(\epsilon_{\mathbf{q}/2+\mathbf{k},-}\right) + f\left(\epsilon_{\mathbf{q}/2-\mathbf{k},-}\right) - 1}{i\nu_n - \epsilon_{\mathbf{q}/2+\mathbf{k},-} - \epsilon_{\mathbf{q}/2-\mathbf{k},-}} - \frac{1}{\epsilon_{\mathbf{k}}}\right] \\ &\quad - \frac{1}{4V}\sum_{\mathbf{k}}\left[1 + \frac{h^2 + \lambda^2\left(q_\perp^2/4 - k_\perp^2\right)}{\sqrt{h^2+\lambda^2\left(\mathbf{q}/2+\mathbf{k}\right)_\perp^2}\sqrt{h^2+\lambda^2\left(\mathbf{q}/2-\mathbf{k}\right)_\perp^2}}\right] \\ &\quad C_{res}(\mathbf{q}, i\nu_n; \mathbf{k}),\end{aligned} \tag{3.17}$$

where $f(x) = 1/(e^{\beta x}+1)$ is the Fermi distribution function and

$$\begin{aligned}C_{res} &= \frac{\left[f\left(\epsilon_{\mathbf{q}/2+\mathbf{k},+}\right) + f\left(\epsilon_{\mathbf{q}/2-\mathbf{k},+}\right) - 1\right]}{i\nu_n - \epsilon_{\mathbf{q}/2+\mathbf{k},+} - \epsilon_{\mathbf{q}/2-\mathbf{k},+}} + \frac{\left[f\left(\epsilon_{\mathbf{q}/2+\mathbf{k},-}\right) + f\left(\epsilon_{\mathbf{q}/2-\mathbf{k},-}\right) - 1\right]}{i\nu_n - \epsilon_{\mathbf{q}/2+\mathbf{k},-} - \epsilon_{\mathbf{q}/2-\mathbf{k},-}} \\ &\quad \frac{\left[f\left(\epsilon_{\mathbf{q}/2+\mathbf{k},+}\right) + f\left(\epsilon_{\mathbf{q}/2-\mathbf{k},-}\right) - 1\right]}{i\nu_n - \epsilon_{\mathbf{q}/2+\mathbf{k},+} - \epsilon_{\mathbf{q}/2-\mathbf{k},-}} - \frac{\left[f\left(\epsilon_{\mathbf{q}/2+\mathbf{k},-}\right) + f\left(\epsilon_{\mathbf{q}/2-\mathbf{k},+}\right) - 1\right]}{i\nu_n - \epsilon_{\mathbf{q}/2+\mathbf{k},-} - \epsilon_{\mathbf{q}/2-\mathbf{k},+}}\end{aligned} \tag{3.18}$$

In writing the above equations, we have replaced the bare interaction strength U_0 in favor of the s-wave scattering length a_s using

$$\frac{1}{U_0} = \frac{m}{4\pi\hbar^2 a_s} - \frac{1}{V}\sum_{\mathbf{k}}\frac{1}{2\epsilon_{\mathbf{k}}} \tag{3.19}$$

with $\epsilon_{\mathbf{k}} = \hbar^2 k^2/(2m)$.

3.3 Results on Two-Body Problem

Let us first consider the two-body problem. The SO coupling term has some interesting effects on the single-particle physics even for non-interacting case. The single-particle spectrum (i.e., the eigenenergy of the dressed states) can be straightforwardly obtained as

$$\epsilon_{\mathbf{k},\pm} = \xi_{\mathbf{k}} \pm \sqrt{h^2 + \lambda^2 k_\perp^2}\,, \tag{3.20}$$

where $k_\perp = \sqrt{k_x^2 + k_y^2}$ is the magnitude of the transverse momentum. The lowest single-particle state occurs at $k_z = 0$ and

$$k_\perp = \begin{cases} \sqrt{m^2\lambda^2/\hbar^4 - h^2/\lambda^2}\,, & h < m\lambda^2/\hbar^2 \\ 0\,, & \text{otherwise} \end{cases}, \tag{3.21}$$

with the corresponding lowest single-particle energy as (taking $\mu = 0$):

$$\epsilon_{\min} = \begin{cases} -m\lambda^2/(2\hbar^2) - \hbar^2 h^2/(2m\lambda^2)\,, & h < m\lambda^2/\hbar^2 \\ -h\,, & \text{otherwise} \end{cases}. \tag{3.22}$$

Hence for h smaller than a threshold value $m\lambda^2/\hbar^2$, the single-particle ground state is infinitely degenerate and occurs along a ring in momentum space centered at $\mathbf{k} = 0$ and lies in the transverse plane. This increases the density of states. The radius of the 'Rashba ring' decreases as h increases and vanishes when h exceeds the threshold value, in which case the ground state becomes non-degenerate and occurs at momentum $\mathbf{k} = 0$.

The corresponding two-body inverse vertex function can be obtained from Eq. (3.17) by discarding the Fermi distribution function and by setting chemical potential $\mu = 0$. This leads to

$$\Gamma_{2b}^{-1}(q) = \frac{m}{4\pi\hbar^2 a_s} - \frac{1}{2V}\sum_{\mathbf{k}}\left[\frac{1}{i\nu_n - \epsilon_{\mathbf{q}/2+\mathbf{k},+} - \epsilon_{\mathbf{q}/2-\mathbf{k},+}} + \frac{1}{i\nu_n - \epsilon_{\mathbf{q}/2+\mathbf{k},-} - \epsilon_{\mathbf{q}/2-\mathbf{k},-}} + \frac{1}{\epsilon_{\mathbf{k}}}\right] + \frac{1}{4V}\sum_{\mathbf{k}}\left[1 + \frac{h^2 + \lambda^2\left(q_\perp^2/4 - k_\perp^2\right)}{\sqrt{h^2 + \lambda^2(\mathbf{q}/2+\mathbf{k})_\perp^2}\sqrt{h^2 + \lambda^2(\mathbf{q}/2-\mathbf{k})_\perp^2}}\right] \bar{C}_{res}^{2b}(\mathbf{q}, i\nu_n; \mathbf{k}), \tag{3.23}$$

where

$$\bar{C}_{res}^{2b} = +\frac{1}{i\nu_n - \epsilon_{\mathbf{q}/2+\mathbf{k},+} - \epsilon_{\mathbf{q}/2-\mathbf{k},+}} + \frac{1}{i\nu_n - \epsilon_{\mathbf{q}/2+\mathbf{k},-} - \epsilon_{\mathbf{q}/2-\mathbf{k},-}} - \frac{1}{i\nu_n - \epsilon_{\mathbf{q}/2+\mathbf{k},+} - \epsilon_{\mathbf{q}/2-\mathbf{k},-}} - \frac{1}{i\nu_n - \epsilon_{\mathbf{q}/2+\mathbf{k},-} - \epsilon_{\mathbf{q}/2-\mathbf{k},+}}. \tag{3.24}$$

3.3.1 Bound State

One important question concerning the two-body system is whether there exist bound states. The zero-momentum bound state energy E_B can be determined from the vertex function using the following relation ($i\nu_n \to \omega + i0^+$):

$$\mathrm{Re}\left[\Gamma_{2b}^{-1}(\mathbf{q} = 0; \omega = E_B) = 0\right], \tag{3.25}$$

from which we may derive the equation for the bound state energy as

$$0 = \frac{m}{4\pi\hbar^2 a_s} - \frac{1}{2V}\sum_{\mathbf{k}}\left[\frac{1}{E_B - 2\epsilon_{\mathbf{k},+}} + \frac{1}{E_B - 2\epsilon_{\mathbf{k},-}} + \frac{1}{\epsilon_{\mathbf{k}}}\right] + \frac{1}{V}\sum_{\mathbf{k}}\frac{4h^2}{\left(E_B - 2\epsilon_{\mathbf{k}}\right)\left(E_B - 2\epsilon_{\mathbf{k},+}\right)\left(E_B - 2\epsilon_{\mathbf{k},-}\right)} \tag{3.26}$$

A bound state exists if its energy satisfies

$$E_B < 2\epsilon_{\min}, \tag{3.27}$$

where $\epsilon_{\min}$ is the lowest single-particle energy defined in Eq. (3.22). It is very natural that the molecular bound state energy should be less than twice the single-particle ground state energy.

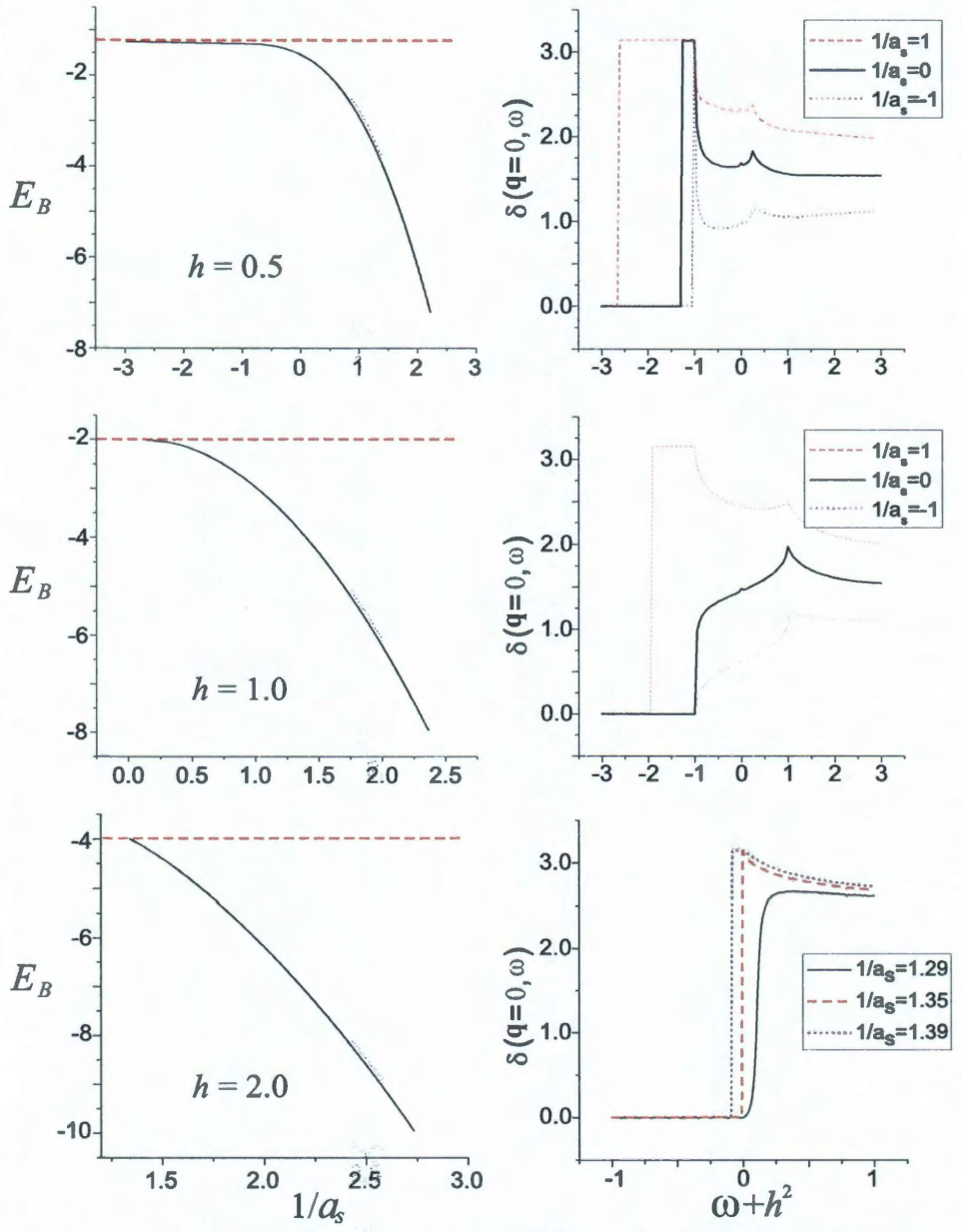

Figure 3.1 : Left panel: Bound state energies E_B as functions of scattering length for different Zeeman field h. The horizontal dashed lines represent the threshold energy $2\epsilon_{\min}$. Right panel: Corresponding two-body phase shifts $\delta(\mathbf{q}=0,\omega)$ for different Zeeman field h. E_B and h are in units of $m\lambda^2/\hbar^2$, a_s is in units of $\hbar^2/(m\lambda)$.

We solve Eq. (3.26) numerically to find E_B and the results are shown in the left panel of Fig. 3.1, where we plot E_B as a function of the contact interaction strength for three different values of the Zeeman field ($h = 0.5$, 1.0 and $2.0\,m\lambda^2/\hbar^2$). For $h < m\lambda^2/\hbar^2$, i.e., when the Rashba ring exists as the lowest single-particle state [see Eq. (3.21)], we always find one bound state solution regardless of the sign of a_s. It is well known that, in the absence of the SO coupling, a two-body bound state does not exist on the BCS side (i.e., $a_s < 0$). The existence of the Rashba ring induced by the SO coupling enhances the density of states near the single-particle ground state and favors the formation of a bound state [90]. By contrast, for $h \geq m\lambda^2/\hbar^2$, the Rashba ring collapses to a point and a two-body bound state only occurs on the BEC side. Furthermore, the larger the h is, the stronger attractive interaction (i.e., larger a_s^{-1}) is required to have a bound state. For example, at $h = 1.0\,m\lambda^2/\hbar^2$, the bound state exists for $a_s^{-1} > 0$; at $h = 2.0\,m\lambda^2/\hbar^2$, the bound state exists only for $a_s^{-1} > 1.35\,m\lambda/\hbar^2$ (see Fig. 3.1).

A bound state can be examined by calculating the phase shift [29, 108]

$$\delta(\mathbf{q},\omega) = -\,\mathrm{Im}\left\{\ln[-\Gamma_{2\mathrm{b}}^{-1}(\mathbf{q}, i\nu_n \to \omega + i0^+)]\right\} . \tag{3.28}$$

In the right panel of Fig. 3.1, we display the phase shift at $\mathbf{q} = 0$. When a bound state occurs, the phase shift will have a discontinuous jump of π when the frequency is equal to the corresponding bound state energy as can be seen in the figure. When the frequency is larger than $2\epsilon_{\mathrm{min}}$ the molecular bound state breaks and the phase shift comes from the usual atom atom scattering. The phase shift calculation via Eq. (3.28) and the bound state energy calculation via Eq. (3.26) thus corroborate each other.

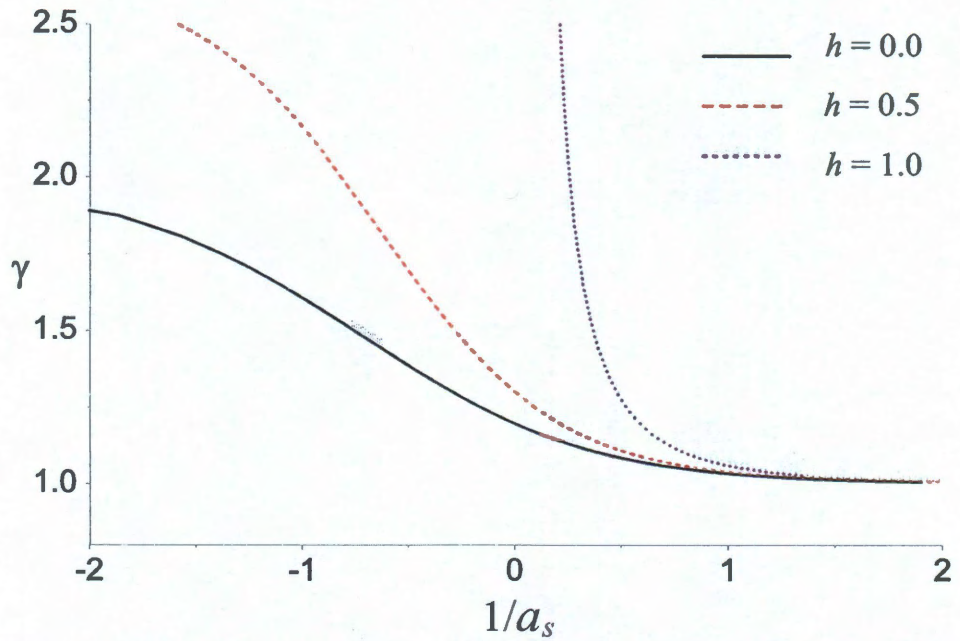

Figure 3.2 : Effective mass $\gamma \equiv M_\perp/(2m)$ as functions of scattering length for different Zeeman field h. h is in units of $m\lambda^2/\hbar^2$, and a_s is in units of $\hbar^2/(m\lambda)$. For $h \geq 1$, the two-body bound state only exists for $a_s > 0$.

3.3.2 Effective Mass

An important quantity that characterizes the properties of the bound state is its effective mass. At small momentum $|\mathbf{q}|$, we may assume that the bound state has a well-defined dispersion, $\epsilon^B_{\mathbf{q}} = \hbar^2 q_\perp^2/(2M_\perp) + \hbar^2 q_z^2/(4m)$, where $M_\perp$ is the effective mass in the transverse plane. Due to the nature of the Rashba SO coupling, the effective mass of the bound state along the z-axis is simple twice of the atomic mass and is not affected by the spin-orbit term. For a given $\mathbf{q}$, we determine $\epsilon^B_{\mathbf{q}}$ from the equation: $\mathrm{Re}\left[\Gamma^{-1}_{2b}\left(\mathbf{q}; \omega = E_B + \epsilon^B_{\mathbf{q}}\right) = 0\right]$. By Taylor expanding the two-body inverse vertex function around $|\mathbf{q}| = 0$, and after some tedious but straightforward calculation, we obtain:

$$\frac{1}{\gamma} \equiv \frac{2m}{M_\perp} = 1 - \frac{4m\lambda^2}{\hbar^2}\frac{Y}{X}, \tag{3.29}$$

where

$$X = \frac{1}{V}\sum_{\mathbf{k}}\left\{\left[\frac{2h^2}{h^2+\lambda^2k_\perp^2}\right]\frac{1}{\left(E_B-2\epsilon_{\mathbf{k}}\right)^2}+\frac{\lambda^2k_\perp^2}{h^2+\lambda^2k_\perp^2}\left[\frac{1}{\left(E_B-2\epsilon_{\mathbf{k},+}\right)^2}+\frac{1}{\left(E_B-2\epsilon_{\mathbf{k},-}\right)^2}\right]\right\}, \tag{3.30}$$

$$Y = \frac{1}{V}\sum_{\mathbf{k}}\left\{\frac{\lambda^2k_\perp^2\left(3h^2+\lambda^2k_\perp^2\right)}{\left(h^2+\lambda^2k_\perp^2\right)^2}\frac{1}{\left(E_B-2\epsilon_{\mathbf{k},+}\right)\left(E_B-2\epsilon_{\mathbf{k},-}\right)}\frac{1}{\left(E_B-2\epsilon_{\mathbf{k}}\right)}-\frac{h^2\lambda^2k_\perp^2}{\left(h^2+\lambda^2k_\perp^2\right)^2}\frac{1}{\left(E_B-2\epsilon_{\mathbf{k}}\right)^3}-\frac{\lambda^2k_\perp^2(2h^2+\lambda^2k_\perp^2)}{\left(h^2+\lambda^2k_\perp^2\right)^2}\left[\frac{\left(E_B-2\epsilon_{\mathbf{k}}\right)}{\left(E_B-2\epsilon_{\mathbf{k},+}\right)^2\left(E_B-2\epsilon_{\mathbf{k},-}\right)^2}\right]\right\}. \tag{3.31}$$

Figure 3.2 displays the effective mass $M_\perp$ as functions of the scattering length a_s for several values of the Zeeman field strength (h). $M_\perp$ monotonically decreases as $1/a_s$ increases. In the BEC limit where $a_s \to 0^+$, $M_\perp \to 2m$ independent of the value of h.

3.4 Results on Many-Body Problem

We now turn to the discussion of the many-body properties. Here, we only consider the mean-field properties of the system, while the effect of fluctuations will be studied in the future. In the mean-field level, the order parameter Δ_0 is a constant and the corresponding momentum space single-particle Green function takes the form $(k = \mathbf{k}, i\omega_m)$,

$$\mathcal{G}_0^{-1}(k) = \begin{bmatrix} i\omega_m - \xi_{\mathbf{k}} - h\hat{\sigma}_z - \lambda(k_y\hat{\sigma}_x - k_x\hat{\sigma}_y) & i\Delta_0\hat{\sigma}_y \\ -i\Delta_0\hat{\sigma}_y & i\omega_m + \xi_{\mathbf{k}} + h\hat{\sigma}_z - \lambda(k_y\hat{\sigma}_x + k_x\hat{\sigma}_y) \end{bmatrix}. \tag{3.32}$$

Plugging this into Eq. (3.9), we may obtain the thermodynamic potential as

$$\Omega_0 = \frac{1}{V}\sum_{\mathbf{k}}\left(\xi_{\mathbf{k}} - \frac{E_{\mathbf{k}+} + E_{\mathbf{k}-}}{2}\right) - \frac{\Delta_0^2}{U_0} - k_BT\sum_{\mathbf{k},\alpha=\pm}\ln\left[1 + e^{-E_{\mathbf{k}\alpha}/k_BT}\right]. \tag{3.33}$$

where $E_{\mathbf{k}\pm} = \sqrt{\xi_{\mathbf{k}}^2 + \Delta_0^2 + h^2 + \lambda^2k_\perp^2 \pm 2\sqrt{(h^2 + \lambda^2k_\perp^2)\xi_{\mathbf{k}}^2 + h^2\Delta_0^2}}$ is the quasi-particle dispersion. The chemical potential and order parameter should be determined by,

$$0 = \frac{\partial\Omega_0}{\partial\Delta_0}, \quad N = -\frac{\partial\Omega_0}{\partial\mu},$$

from which we derive the gap and the number equations as follows:

$$\frac{1}{U_0} = \frac{1}{V}\sum_{\mathbf{k},\alpha=\pm}\frac{2f(E_{\mathbf{k}\alpha}) - 1}{4E_{\mathbf{k}\alpha}}\left[1 + \alpha\frac{h^2}{\sqrt{(h^2 + \lambda^2k_\perp^2)\xi_{\mathbf{k}}^2 + h^2\Delta_0^2}}\right], \tag{3.34}$$

$$n = \frac{1}{V}\sum_{\mathbf{k}}\left\{1 + \sum_{\alpha=\pm}\frac{\xi_{\mathbf{k}}[2f(E_{\mathbf{k}\alpha}) - 1]}{2E_{\mathbf{k}\alpha}}\left[1 + \alpha\frac{h^2 + \lambda^2k_\perp^2}{\sqrt{(h^2 + \lambda^2k_\perp^2)\xi_{\mathbf{k}}^2 + h^2\Delta_0^2}}\right]\right\} \tag{3.35}$$

In the following, we will show various quantities of physical interest, obtained from solving Eqs. (3.34) and (3.35) self-consistently. We focus on the zero-temperature case, although Eqs. (3.34) and (3.35) are valid for finite temperatures.

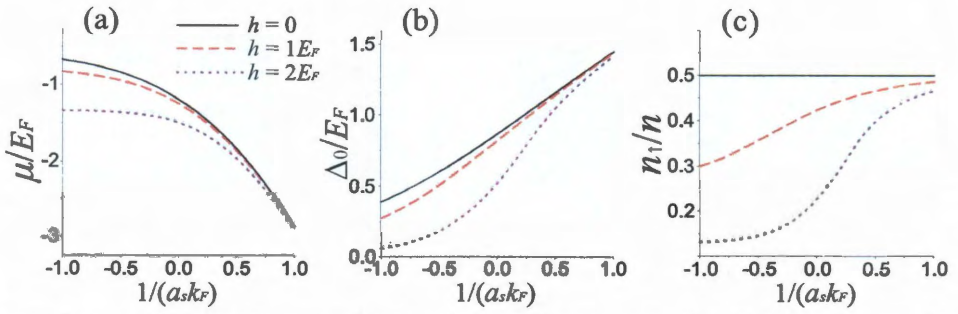

Figure 3.3 : Chemical potential μ (a), pairing gap Δ_0 (b), and population of spin-up component $n_\uparrow$ (c) as functions of scattering length a_s for different values of the Zeeman field h at $\lambda k_F/E_F = 2$. Here $k_F = (3\pi^2 n)^{1/3}$ and $E_F = \hbar^2 k_F^2/(2m)$ are the Fermi momentum and Fermi energy, respectively.

3.4.1 Chemical Potential and Gap

We show in Fig. 3.3(a) and (b) the chemical potential μ and the pairing gap Δ_0, respectively, as functions of the scattering length for different values of the Zeeman field. Without the Zeeman field, as spin-orbit coupling increases the density of states, it increases BCS pairing in both the BCS region and the unitarity region. With the Zeeman field, as it can be treated as the chemical potential difference of the two species. The bigger external Zeeman field means the more imbalanced in the system. The Zeeman field makes BCS pairing for the $k,\uparrow$ atom different from the $k,\downarrow$ atoms as the Fermi surfaces for the two species mismatch. It suppresses the pairing gap. In Fig. 3.3(c), we plot the population of the spin-up component. For zero Zeeman field, we always have equal population in both spin components. For $h > 0$, the spin-up component has less population. In all cases, the effects of the Zeeman field together with the spin orbit coupling reduce as the BEC limit (i.e., $1/a_s \to +\infty$) is approached.

3.4.2 Quasi-particle Spectrum

The quasi-particle dispersion $E_{\mathbf{k}\pm}$ is plotted in Fig. 3.4. The spectrum is sensitive to the polar angle θ of the momentum vector $\mathbf{k}$. For $\mathbf{k}$ along the z-axis (i.e., $\theta = 0$ and $k_\perp = 0$), $E_{\mathbf{k}-}$ may become zero at certain values of k when h is sufficiently large, signaling a gapless dispersion. The points at which $E_{\mathbf{k}-} = 0$ are called Fermi points. The value of the Zeeman field at which new Fermi points appear represents a quantum critical point for topological phase transition [95, 102]. For $\mu > 0$, the system may support 0, 2 or 4 Fermi points along the k_z-axis as h is increased. For $\mu < 0$ which is the case illustrated in Fig. 3.4, there can be either 0 or 2 Fermi points [96]. For $\lambda k_F/E_F = 2$, the critical Zeeman field is $h_c \approx 1.5E_F$. For $h < h_c$, the system is a topologically trivial gapped superfluid; for $h > h_c$, the system possesses two Fermi points and represents a topologically nontrivial gapless superfluid. Note that the quasi-particle dispersion has been measured in recent experiments on ultracold Fermi gases [51, 52] using momentum resolved radio frequency spectroscopy.

3.4.3 Pairing Profile

Even though in our model the interaction has a contact s-wave form, due to the presence of the SO coupling, pairing can occur in both singlet and triplet channels [103]. The singlet pairing field between unlike spins can be calculated as:

$$\langle \psi_{\mathbf{k}\uparrow}\psi_{-\mathbf{k}\downarrow}\rangle = -\Delta_0 \left\{ \sum_{\alpha=\pm} \frac{2f(E_{\mathbf{k}\alpha})-1}{4E_{\mathbf{k}\alpha}} [1 + \alpha \frac{h^2}{\sqrt{(h^2+\lambda^2 k_\perp^2)\xi_{\mathbf{k}}^2 + h^2\Delta_0^2}}] \right\} \quad (3.36)$$

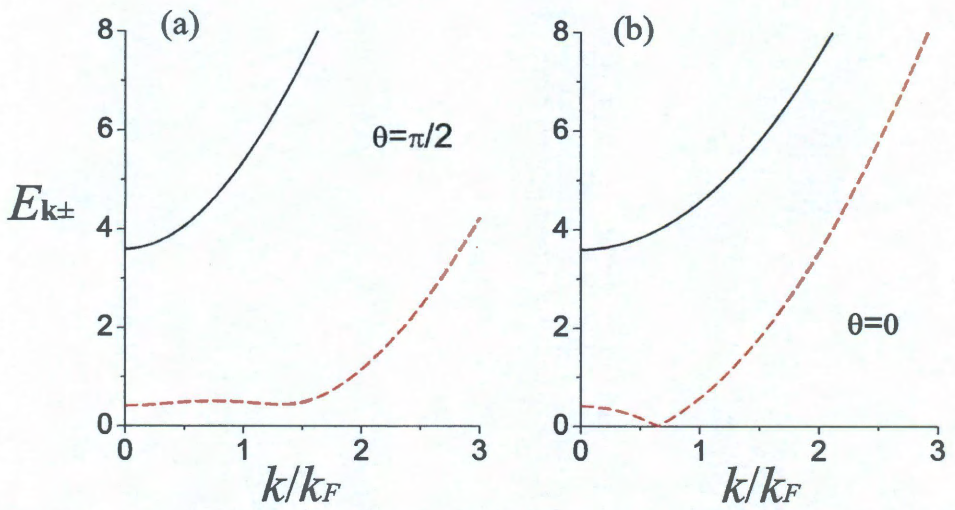

Figure 3.4 : Quasi-particle dispersion spectrum $E_{\mathbf{k}+}$ (solid lines) and $E_{\mathbf{k}-}$ (dashed lines) shown in in units of E_F for $\mathbf{k}$ in the transverse plane (a, $\theta = \pi/2$) and along the z-axis (b, $\theta = 0$) for $\lambda k_F/E_F = 2$, $h/E_F = 2$.

while the triplet pairing fields between like spins are given by:

$$\langle \psi_{\mathbf{k}\uparrow}\psi_{-\mathbf{k}\uparrow}\rangle = \Delta_0 \frac{\lambda(k_y + ik_x)(\xi_{\mathbf{k}} - h)}{\sqrt{(h^2 + \lambda^2 k_\perp^2)\xi_{\mathbf{k}}^2 + h^2\Delta_0^2}} \left[\frac{2f(E_{\mathbf{k}+}) - 1}{4E_{\mathbf{k}+}} - \frac{2f(E_{\mathbf{k}-}) - 1}{4E_{\mathbf{k}-}}\right] \quad (3.37)$$

$$\langle \psi_{\mathbf{k}\downarrow}\psi_{-\mathbf{k}\downarrow}\rangle = -\Delta_0 \frac{\lambda(k_y - ik_x)(\xi_{\mathbf{k}} + h)}{\sqrt{(h^2 + \lambda^2 k_\perp^2)\xi_{\mathbf{k}}^2 + h^2\Delta_0^2}} \left[\frac{2f(E_{\mathbf{k}+}) - 1}{4E_{\mathbf{k}+}} - \frac{2f(E_{\mathbf{k}-}) - 1}{4E_{\mathbf{k}-}}\right] \quad (3.38)$$

We plot in Fig. 3.5 the absolute value of the various pairing fields. One can see that the effect of the Zeeman field is to reduce the singlet pairing while enhancing the triplet pairing.

3.4.4 Density of States

From the single-particle Green's function, one can immediately obtain the density of states which is an important quantity characterizing the nature of the quantum state.

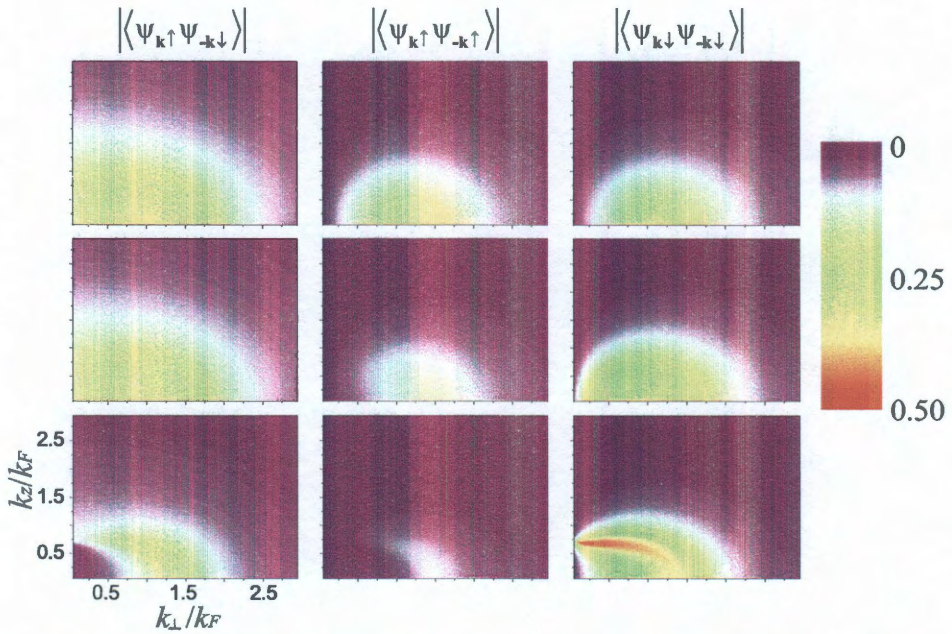

Figure 3.5 : Pairing fields at unitarity (i.e., $1/a_s = 0$) for $h = 0$ (top row), $h = 1E_F$ (middle row), $h = 2E_F$ (bottom row) and $\lambda k_F/E_F = 2$. In each row, from left to right, we display $|\langle\psi_{\mathbf{k}\uparrow}\psi_{-\mathbf{k}\downarrow}\rangle|$, $|\langle\psi_{\mathbf{k}\uparrow}\psi_{-\mathbf{k}\uparrow}\rangle|$ and $|\langle\psi_{\mathbf{k}\downarrow}\psi_{-\mathbf{k}\downarrow}\rangle|$ (all in units of E_F), respectively.

We invert Eq. (3.32) to get

$$\mathcal{G}_0\left(\mathbf{k}, i\omega_m\right) = \begin{bmatrix} \hat{g}(\mathbf{k}, i\omega_m) & \hat{f}(\mathbf{k}, i\omega_m) \\ \left[\hat{f}(+\mathbf{k}, -i\omega_m)\right]^+ & -\left[\hat{g}(-\mathbf{k}, -i\omega_m)\right]^T \end{bmatrix}, \tag{3.39}$$

where $\hat{g}$ and $\hat{f}$ are both 2×2 matrices whose expressions are.

$$\begin{aligned} \hat{g}(\mathbf{k}, i\omega_m) &= \left[i\omega_m + \xi_{\mathbf{k}} - h\hat{\sigma}_z + \lambda(k_y\hat{\sigma}_x - k_x\hat{\sigma}_y)\right]\mathcal{D}_+/M, \\ \hat{f}(\mathbf{k}, i\omega_m) &= \left[-i\Delta_0\hat{\sigma}_y\right]\mathcal{D}_-/M. \end{aligned} \tag{3.40}$$

with

$$M = \left[(i\omega_m - h)^2 - \xi_{\mathbf{k}}^2 - \Delta_0^2 - \lambda^2 k_\perp^2\right]\left[(i\omega_m + h)^2 - \xi_{\mathbf{k}}^2 - \Delta_0^2 - \lambda^2 k_\perp^2\right] - 4\lambda^2 k_\perp^2\left(\xi_{\mathbf{k}}^2 - h^2\right), \tag{3.41}$$

and

$$\mathcal{D}_+ = \begin{bmatrix} (i\omega_m + h)^2 - \xi_{\mathbf{k}}^2 - \Delta_0^2 - \lambda^2 k_\perp^2 & \lambda\left(k_y + ik_x\right)\left[2\left(\xi_{\mathbf{k}} + h\right)\right] \\ \lambda\left(k_y - ik_x\right)\left[2\left(\xi_{\mathbf{k}} - h\right)\right] & (i\omega_m - h)^2 - \xi_{\mathbf{k}}^2 - \Delta_0^2 - \lambda^2 k_\perp^2 \end{bmatrix} \tag{3.42}$$

$$\mathcal{D}_- = \begin{bmatrix} (i\omega_m - h)^2 - \xi_{\mathbf{k}}^2 - \Delta_0^2 - \lambda^2 k_\perp^2 & -\lambda\left(k_y - ik_x\right)\left[2\left(\xi_{\mathbf{k}} + h\right)\right] \\ -\lambda\left(k_y + ik_x\right)\left[2\left(\xi_{\mathbf{k}} - h\right)\right] & (i\omega_m + h)^2 - \xi_{\mathbf{k}}^2 - \Delta_0^2 - \lambda^2 k_\perp^2 \end{bmatrix} \tag{3.43}$$

In greater detail, we find that,

$$\hat{g}(\mathbf{k}, i\omega_m) = \begin{bmatrix} \hat{g}_{11}\left(\mathbf{k}, i\omega_m\right) & \hat{g}_{12}\left(\mathbf{k}, i\omega_m\right) \\ \hat{g}_{12}^*\left(\mathbf{k}, -i\omega_m\right) & \hat{g}_{22}\left(\mathbf{k}, i\omega_m\right) \end{bmatrix}, \tag{3.44}$$

where,

$$\begin{aligned} M\hat{g}_{11}\left(\mathbf{k}, i\omega_m\right) &= \left[i\omega_m + \xi_{\mathbf{k}} - h\right]\left[(i\omega_m + h)^2 - \xi_{\mathbf{k}}^2 - \Delta_0^2 - \lambda^2 k_\perp^2\right] \\ &\quad + 2\lambda^2 k_\perp^2\left(\xi_{\mathbf{k}} - h\right), \end{aligned} \tag{3.45}$$

$$M\hat{g}_{12}\left(\mathbf{k}, i\omega_m\right) = \lambda\left(k_y + ik_x\right)\left[(i\omega_m + \xi_{\mathbf{k}})^2 - h^2 - \Delta_0^2 - \lambda^2 k_\perp^2\right], \tag{3.46}$$

$$\begin{aligned} M\hat{g}_{22}\left(\mathbf{k}, i\omega_m\right) &= \left[i\omega_m + \xi_{\mathbf{k}} + h\right]\left[(i\omega_m - h)^2 - \xi_{\mathbf{k}}^2 - \Delta_0^2 - \lambda^2 k_\perp^2\right] \\ &\quad + 2\lambda^2 k_\perp^2\left(\xi_{\mathbf{k}} + h\right), \end{aligned} \tag{3.47}$$

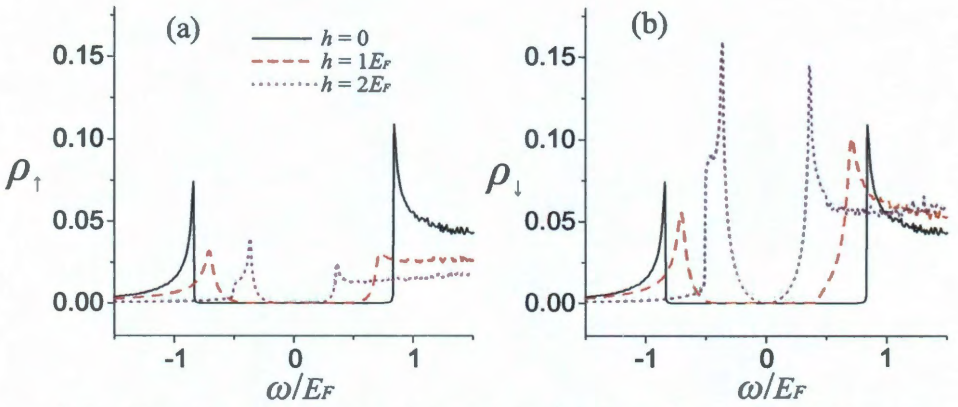

Figure 3.6 : Density of states $\rho_\uparrow$ (a) and $\rho_\downarrow$ (b) at unitarity and $\lambda k_F/E_F = 2$.

and

$$\hat{f}(\mathbf{k}, i\omega_m) = \frac{\Delta_0}{M}\begin{bmatrix} \lambda(k_y + ik_x)\left[2(\xi_\mathbf{k} - h)\right] & -\left[(i\omega_m + h)^2 - \xi_\mathbf{k}^2 - \Delta_0^2 - \lambda^2 k_\perp^2\right] \\ \left[(i\omega_m - h)^2 - \xi_\mathbf{k}^2 - \Delta_0^2 - \lambda^2 k_\perp^2\right] & -\lambda(k_y - ik_x)\left[2(\xi_\mathbf{k} + h)\right] \end{bmatrix}. \tag{3.48}$$

The density of states are related to the $\hat{g}$ matrix as

$$\rho_\uparrow(\omega) = -\frac{1}{\pi}\mathrm{Im}\left[\frac{1}{V}\sum_\mathbf{k} g_{11}(k, \omega + i0^+)\right], \tag{3.49}$$

$$\rho_\downarrow(\omega) = -\frac{1}{\pi}\mathrm{Im}\left[\frac{1}{V}\sum_\mathbf{k} g_{22}(k, \omega + i0^+)\right]. \tag{3.50}$$

where the expressions of g_{11} and g_{22} can be found in Eqs. (3.45) and (3.47).

We show in Fig. 3.6 the density of states at different Zeeman fields. At $h = 0$, $\rho_\uparrow$ and $\rho_\downarrow$ are identical, both exhibiting a large gapped region. As h increases, the gapped region shrinks. Furthermore, the density of states for the majority component (which is the spin down component for our choice of positive h) becomes more V-shaped near $\omega = 0$ when there are Fermi points in the spectrum. A V-shaped density of states comes from the node of the pairing which is the characteristic feature of many unconventional superconductors with non-s-wave pairing. Here it is due to the

pairing resulting from the SO coupling together with the Zeeman field. The density of states may be measured in experiment using the scheme proposed in Ref. [109].

3.4.5 Spin Structure Factor

Finally, let us consider the spin structure factor [58, 60] which is related to the dynamic spin susceptibility $\chi_S(\mathbf{q}, i\nu_n)$, which is the Fourier transformation of the spin-spin correlation function

$$\chi_S(\mathbf{x}, \tau) = -\langle \mathrm{T}_\tau \delta n_S(\mathbf{x}, \tau)\, \delta n_S(\mathbf{0}, 0)\rangle \ . \tag{3.51}$$

where the spin density is given by $\delta n_S = n_\uparrow - n_\downarrow$. Using the Nambu spinor notation, the spin density can be written as,

$$\delta n_S = \frac{1}{2}\Phi^+ \begin{bmatrix} 1 & 0 & 0 & 0 \\ 0 & -1 & 0 & 0 \\ 0 & 0 & -1 & 0 \\ 0 & 0 & 0 & 1 \end{bmatrix} \Phi = \frac{1}{2}\Phi^+ \left[\hat{\tau}_z \otimes \hat{\sigma}_z\right] \Phi. \tag{3.52}$$

where $\hat{\tau}_i$ are the Pauli matrices describing the Nambu spinor degrees of freedom. Within the static Bogoliubov approximation, we have,

$$\chi_S(\mathbf{q}, i\nu_n) = \frac{1}{4} k_B T \sum_{\mathbf{k}, i\omega_m} \mathrm{Tr}\left\{\hat{\tau}_z \otimes \hat{\sigma}_z \mathcal{G}_0(\mathbf{k}, i\omega_m)\, \hat{\tau}_z \otimes \hat{\sigma}_z \mathcal{G}_0(\mathbf{k}+\mathbf{q}, i\omega_m + i\nu_n)\right\}. \tag{3.53}$$

The zero-momentum dynamic spin structure factor is given by

$$S_S(\mathbf{q}=\mathbf{0}, \omega) = -\frac{1}{1 - e^{-\omega/k_B T}} \frac{1}{\pi} \mathrm{Im}\left[\chi_S\left(\mathbf{q}=\mathbf{0}, i\nu_n \to \omega + i0^+\right)\right] \ , \tag{3.54}$$

via analytic continuation and the fluctuation-dissipation theorem.

Here we only consider the zero temperature case.

$$\begin{aligned}\chi_s(0,iv_n) &= \frac{1}{2}\frac{1}{\beta V}\sum_{k,iw_n}\{g_{11}(k,iw_n)g_{11}(k,iw_n+iv_n)-g_{12}(k,iw_n)g_{21}(k,iw_n+iv_n)\\ &\quad -g_{21}(k,iw_n)g_{12}(k,iw_n+iv_n)+g_{22}(k,iw_n)g_{22}(k,iw_n+iv_n)\\ &\quad -f_{11}(k,iw_n)f^*_{11}(k,-iw_n-iv_n)+f_{12}(k,iw_n)f^*_{12}(k,-iw_n-iv_n)\\ &\quad +f_{21}(k,iw_n)f^*_{21}(k,-iw_n-iv_n)-f_{22}(k,iw_n)f^*_{22}(k,-iw_n-iv_n)\}\end{aligned} \tag{3.55}$$

$$\begin{aligned}S_s(0,w) &= \frac{1}{16}\frac{1}{V}\sum_k\delta(w-2E_{k+})[u^0_{11}(k_+)v^0_{11}(k_+)+u^1_{11}(k_+)v^1_{11}(k_+)\\ &\quad -u_{12}(k_+)v_{12}(k_+)-p^2_+(k)+q^2(k)+\frac{\Delta^2(\zeta_k^2+h^2)\lambda^2k_\perp^2}{[(h^2+\lambda^2k_\perp^2)\zeta_k^2+h^2\Delta^2]E^2_{k+}}]\\ &\quad +\frac{1}{16}\frac{1}{V}\sum_k\delta(w-2E_{k-})[u^0_{11}(k_-)v^0_{11}(k_-)+u^1_{11}(k_-)v^1_{11}(k_-)\\ &\quad -u_{12}(k_-)v_{12}(k_-)-p^2_-(k)+q^2(k)+\frac{\Delta^2(\zeta_k^2+h^2)\lambda^2k_\perp^2}{[(h^2+\lambda^2k_\perp^2)\zeta_k^2+h^2\Delta^2]E^2_{k-}}]\\ &\quad -v_{12}(k_+)v_{12}(k_-)+2p_+(k)p_-(k)-2q^2(k)+\frac{2\Delta^2(\zeta_k^2+h^2)\lambda^2k_\perp^2}{[(h^2+\lambda^2k_\perp^2)\zeta_k^2+h^2\Delta^2]E_{k+}E_{k-}}]\\ &\quad +\frac{1}{16}\frac{1}{V}\sum_k\delta(w-E_{k+}-E_{k-})[u^0_{11}(k_+)v^0_{11}(k_-)+v^0_{11}(k_+)u^0_{11}(k_-)\\ &\quad +u^1_{11}(k_+)v^1_{11}(k_-)+v^1_{11}(k_+)u^1_{11}(k_-)-u_{12}(k_+)v_{12}(k_-)-v_{12}(k_+)u_{12}(k_-)\\ &\quad -2p_+(k)p_-(k)-2q^2(k)-\frac{2\Delta^2(\zeta_k^2+h^2)\lambda^2k_\perp^2}{[(h^2+\lambda^2k_\perp^2)\zeta_k^2+h^2\Delta^2]E_{k+}E_{k-}}]\end{aligned} \tag{3.56}$$

where

$$\begin{aligned}u^0_{11}(k_+) &= 1+\frac{\zeta_k}{E_{k+}}+\frac{\zeta_k(h^2+\lambda^2k_\perp^2)}{E_{k+}\sqrt{(h^2+\lambda^2k_\perp^2)\zeta_k^2+h^2\Delta^2}}\\ v^0_{11}(k_+) &= 1-\frac{\zeta_k}{E_{k+}}-\frac{\zeta_k(h^2+\lambda^2k_\perp^2)}{E_{k+}\sqrt{(h^2+\lambda^2k_\perp^2)\zeta_k^2+h^2\Delta^2}}\\ u^0_{11}(k_-) &= 1+\frac{\zeta_k}{E_{k-}}-\frac{\zeta_k(h^2+\lambda^2k_\perp^2)}{E_{k-}\sqrt{(h^2+\lambda^2k_\perp^2)\zeta_k^2+h^2\Delta^2}}\\ v^0_{11}(k_-) &= 1-\frac{\zeta_k}{E_{k-}}+\frac{\zeta_k(h^2+\lambda^2k_\perp^2)}{E_{k-}\sqrt{(h^2+\lambda^2k_\perp^2)\zeta_k^2+h^2\Delta^2}}\end{aligned} \tag{3.57}$$

$$
\begin{aligned}
u^1_{11}(k_+) &= \frac{h}{E_{k+}} + \frac{\zeta_k h}{\sqrt{(h^2+\lambda^2 k_\perp^2)\zeta_k^2 + h^2\Delta^2}} + \frac{h(\zeta_k^2+\Delta^2)}{E_{k+}\sqrt{(h^2+\lambda^2 k_\perp^2)\zeta_k^2 + h^2\Delta^2}} \\
v^1_{11}(k_+) &= -\frac{h}{E_{k+}} + \frac{\zeta_k h}{\sqrt{(h^2+\lambda^2 k_\perp^2)\zeta_k^2 + h^2\Delta^2}} - \frac{h(\zeta_k^2+\Delta^2)}{E_{k+}\sqrt{(h^2+\lambda^2 k_\perp^2)\zeta_k^2 + h^2\Delta^2}} \\
u^1_{11}(k_-) &= \frac{h}{E_{k-}} - \frac{\zeta_k h}{\sqrt{(h^2+\lambda^2 k_\perp^2)\zeta_k^2 + h^2\Delta^2}} - \frac{h(\zeta_k^2+\Delta^2)}{E_{k-}\sqrt{(h^2+\lambda^2 k_\perp^2)\zeta_k^2 + h^2\Delta^2}} \\
v^1_{11}(k_-) &= \frac{h}{E_{k-}} - \frac{\zeta_k h}{\sqrt{(h^2+\lambda^2 k_\perp^2)\zeta_k^2 + h^2\Delta^2}} + \frac{h(\zeta_k^2+\Delta^2)}{E_{k-}\sqrt{(h^2+\lambda^2 k_\perp^2)\zeta_k^2 + h^2\Delta^2}}
\end{aligned} \tag{3.58}
$$

$$
\begin{aligned}
u_{12}(k_+) &= \frac{\lambda k_\perp}{E_{k+}}\left[1 + \frac{\zeta_k(\zeta_k + E_{k+})}{\sqrt{(h^2+\lambda^2 k_\perp^2)\zeta_k^2 + h^2\Delta^2}}\right] \\
v_{12}(k_+) &= -\frac{\lambda k_\perp}{E_{k+}}\left[1 + \frac{\zeta_k(\zeta_k - E_{k+})}{\sqrt{(h^2+\lambda^2 k_\perp^2)\zeta_k^2 + h^2\Delta^2}}\right] \\
u_{12}(k_-) &= \frac{\lambda k_\perp}{E_{k-}}\left[1 - \frac{\zeta_k(\zeta_k + E_{k-})}{\sqrt{(h^2+\lambda^2 k_\perp^2)\zeta_k^2 + h^2\Delta^2}}\right] \\
v_{12}(k_-) &= -\frac{\lambda k_\perp}{E_{k-}}\left[1 - \frac{\zeta_k(\zeta_k - E_{k-})}{\sqrt{(h^2+\lambda^2 k_\perp^2)\zeta_k^2 + h^2\Delta^2}}\right]
\end{aligned} \tag{3.59}
$$

$$
\begin{aligned}
p_+(k) &= -\frac{\Delta}{E_{k+}}\left[1 + \frac{h^2}{\sqrt{(h^2+\lambda^2 k_\perp^2)\zeta_k^2 + h^2\Delta^2}}\right] \\
p_-(k) &= -\frac{\Delta}{E_{k-}}\left[1 - \frac{h^2}{\sqrt{(h^2+\lambda^2 k_\perp^2)\zeta_k^2 + h^2\Delta^2}}\right] \\
q(k) &= -\frac{h\Delta}{\sqrt{(h^2+\lambda^2 k_\perp^2)\zeta_k^2 + h^2\Delta^2}}
\end{aligned} \tag{3.60}
$$

It can be explicitly shown that the dynamic spin structure factor vanishes when $\lambda = 0$, i.e., in the absence of the SO coupling. Hence a nonzero spin structure factor is a direct consequence of triplet pairing. Fig. 3.7(a) shows the dynamic spin structure factor at different Zeeman fields. At $h = 0$, $S_S(0,\omega)$ exhibits a broad peak. For finite h, an additional narrower peak appears at smaller energy. The corresponding static

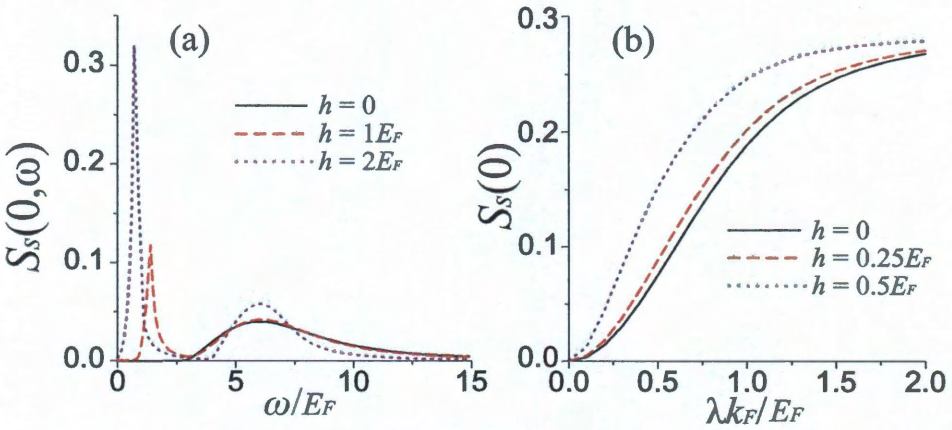

Figure 3.7 : (a) Zero temperature dynamic spin structure factor $S_S(0,\omega)$ at unitarity and $\lambda k_F/E_F = 2$. (b) Static spin structure factor $S_S(0)$ as functions of the SO coupling strength.

spin structure factor is given by

$$S_S(0) = \int d\omega\, S_S(0,\omega)\,,$$

which is plotted in Fig. 3.7(b) as a function of the SO coupling strength. The spin structure factor may be directly measured in experiments using the Bragg spectroscopic method [61, 62, 63].

Chapter 4

Single Impurity In Ultracold Fermi Superfluids

4.1 Model

The development of ultracold atoms provide us with selective experimental controls of many-body quantum system. In ultracold atoms, both the sign and value of the interaction can be accurately tuned using laser lights or magnetic fields. This shows a great advantage compared with the conventional quantum many-body system such as a condensed matter system. In condensed matter experiments, one big problem is the defects contained in the material. The defect comes so naturally in experiments people almost can not avoid them. The only way is to understand the physics of defects in many-body problems. Then comes the theory for impurities in many-body system, which turns out to be a great treasure in condensed matter physics. Impurities can be used as the detector of quantum effects [110, 111]. Single impurities have been employed in the detection of superconducting pairing symmetry within unconventional superconductors [112] and to demonstrate Friedel oscillations [113]. In strongly correlated systems, they may be used to pin one of the competing orders [114]. Even though cold atom systems are intrinsically clean, the effects of impurities may be simulated by employing laser speckles or quasiperiodic lattices [115]. Controllable manipulation of individual impurities in cold atom systems can also be realized using off-resonant laser light or another species of atoms/ions [116, 117, 118, 119]. With some notable advantages in cold atom systems, we anticipate important contributions

for cold atom systems from the study of impurities. Such impurities can be either localized or extended and either static or dynamic. The unprecedented access to accurately tune these artificial impurities provides an exciting possibility to probe and manipulate the properties of cold atoms.

In this chapter, we demonstrate this possibility using a single classical static impurity in an s-wave Fermi superfluid. By 'classical' we refer to the treatment of the impurity as a scattering potential which has no internal degrees of freedom. We focus on both a single non-magnetic impurity and a magnetic impurity. For the non-magnetic impurity, it scatters each spin species equally while for the magnetic impurity it scatters differently. We study both a local impurity and an extended impurity in one-dimension(1D) and three-dimensions(3D). From our self-consistent Bogoliubov-de Gennes calculations we show for the first time in a trapped three-dimensional geometry that the long sought Fulde-Ferrell-Larkin-Ovchinnikov (FFLO) phase, which supports many mid-gap bound states, may be induced through such an impurity at experimentally accessible parameters. Furthermore, we propose that these bound states can be probed using a modified radio-frequency (RF) spectroscopy technique that is the analog of the widely used scanning tunneling microscope (STM) in solid state and that this can serve as a powerful general tool in probing and manipulating quantum gases.

For computational simplicity, we first focus on a one-dimensional system and verify the essential physics at higher dimensions in later paragraphs. Consider the following Hamiltonian at zero temperature,

$$\begin{aligned} H &= \sum_{\sigma=\uparrow,\downarrow} \int dx\, \psi_\sigma^\dagger \left[-\frac{\hbar^2}{2m}\frac{d^2}{dx^2} - \mu_\sigma + V_T \right] \psi_\sigma \\ &\quad + g \int dx\, \psi_\uparrow^\dagger \psi_\downarrow^\dagger \psi_\downarrow \psi_\uparrow + \sum_{\sigma=\uparrow,\downarrow} \int dx\, \psi_\sigma^\dagger U_\sigma \psi_\sigma, \end{aligned} \tag{4.1}$$

where $\psi_\sigma^\dagger(x)$ and $\psi_\sigma(x)$ are, respectively, the fermionic creation and annihilation operators for spin species σ. $V_T(x)$ is a harmonic trapping potential and g is the strength of the inter-atomic interaction. In this work, we take g to be small and negative so that the system is a superfluid at low temperatures and, as for theory, mean field calculation is still valid in the weak interaction case. The last term of the Hamiltonian describes the effect of the impurity which is represented by a scattering potential, $U_\sigma(x)$. For a non-magnetic impurity, $U_\uparrow(x) = U_\downarrow(x)$; while for a magnetic impurity, $U_\uparrow(x) = -U_\downarrow(x)$. Note that a general impurity potential can be decomposed into a sum of magnetic and non-magnetic parts. Here we focus on both non-magnetic and magnetic impurities which can be either localized or extended.

In the next two sections, I will introduce two methods to treat the impurity problem.

4.2 T-Matrix Method

The T-Matrix for single impurity is a perturbation theory. It describes multiple scattering process between an atom and an impurity. It is an exact method for a single impurity as it covers all the diagrams. It is analytically solvable when the perturbation term is independent of momentum $\mathbf{k}$. For the localized impurity which can be described as a contact impurity, The T-matrix method is an exact solvable method[120, 121].

The Hamiltonian for a contact impurity in an s-wave superfluid can be written in momentum space as:

$$\begin{aligned} H &= H_0 + W = \sum_{\mathbf{k},\sigma} \xi_{\mathbf{k}} c^+_{\mathbf{k},\sigma} c_{\mathbf{k},\sigma} + \sum_{\mathbf{k}} (\Delta c^+_{\mathbf{k},\uparrow} c^+_{-\mathbf{k},\downarrow} + h.c.) \\ &\quad + \frac{u}{V} \sum_{\mathbf{k},\mathbf{q}} c^+_{\mathbf{k}+\mathbf{q},\sigma} c_{\mathbf{k},\sigma} \end{aligned} \tag{4.2}$$

Here $c^+_{\mathbf{k},\sigma}$ is a fermion creation operator for a "spin σ" atom, $c_{\mathbf{k},\sigma}$ is a fermion annihilation operator for a "spin σ" atom. $W = \frac{u}{V} \sum_{\mathbf{k},\mathbf{q}} c^+_{\mathbf{k}+\mathbf{q},\sigma} c_{\mathbf{k},\sigma}$ represents the impurity potential which is $\int d\mathbf{r} U(\mathbf{r}) \psi^+(\mathbf{r}) \psi(\mathbf{r})$ and when $U(\mathbf{r})$ is a contact potential $U(\mathbf{r}) = u\delta(\mathbf{r})$. We assume the impurity is located at the origin. We consider the definition of the Green's Function:

$$\begin{aligned} G(iw_n) &= \frac{1}{iw_n - H} = \frac{1}{iw_n - H_0 - W} \\ &= \frac{1}{G_0(iw_n)^{-1} - W} \end{aligned} \tag{4.3}$$

Here W is just like the self-energy in the interaction case as we can treat the self-energy as an external field. This is just Dyson's equation. We can rewrite the form

as a series expansion and get:

$$\begin{aligned} G(iw_n) &= G_0(iw_n) + G_0(iw_n)WG(iw_n) \\ &= G_0(iw_n) + G_0(iw_n)WG_0(iw_n) \\ &\quad + G_0(iw_n)WG_0(iw_n)WG_0(iw_n) + ... \end{aligned} \tag{4.4}$$

In the momentum basis, we have

$$\begin{aligned} G(\mathbf{k},\mathbf{k}',iw_n) &= \langle \mathbf{k}|G(iw_n)|\mathbf{k}'\rangle \\ &= G_0(\mathbf{k},iw_n)\delta_{\mathbf{k},\mathbf{k}'} + G_0(\mathbf{k},iw_n)\frac{u}{V}G_0(\mathbf{k}',iw_n) \\ &\quad + G_0(\mathbf{k},iw_n)\frac{u}{V}\sum_{\mathbf{k}_1}G_0(\mathbf{k}_1,iw_n)\frac{u}{V}G_0(\mathbf{k}',iw_n) + ... \\ &= G_0(\mathbf{k},iw_n)\delta_{\mathbf{k},\mathbf{k}'} + \frac{1}{V}G_0(\mathbf{k},iw_n)T(iw_n)G_0(\mathbf{k}',iw_n) \end{aligned} \tag{4.5}$$

Here, as the impurity breaks translational symmetry, the system is no longer homogeneous. The Green's function will have two momentum labels $\mathbf{k}$, $\mathbf{k}'$.

Let us define the T-matrix as:

$$\begin{aligned} T(iw_n) &= u + u\sum_{\mathbf{k}_1}G_0(\mathbf{k}_1,iw_n)\frac{u}{V} + u[\sum_{\mathbf{k}_1}G_0(\mathbf{k}_1,iw_n)\frac{u}{V}]^2 + ... \\ &= \frac{u}{1-\sum_{\mathbf{k}_1}G_0(\mathbf{k}_1,iw_n)\frac{u}{V}} \end{aligned} \tag{4.6}$$

Due to the use of a contact impurity, the T-matrix can be written as the sum of a geometric series and is independent of momentum. This greatly simplifies the calculation and in this way we can evaluate the T-matrix analytically.

$$T(iw_n)^{-1} = u^{-1} - G_0(0,iw) \tag{4.7}$$

where:

$$G_0(\mathbf{r},iw) = \frac{1}{V}\sum_{\mathbf{k}_1}e^{i\mathbf{k}_1\mathbf{r}}G_0(\mathbf{k}_1,iw) \tag{4.8}$$

$G_0(\mathbf{r}, iw)$ is the Green's function for a homogeneous system in real space. For the Green's function for an inhomogeneous system in real space, we get

$$\begin{aligned} G(\mathbf{r}, \mathbf{r}, iw) &= \frac{1}{V}\sum_{\mathbf{k},\mathbf{k}'} e^{i\mathbf{k}\mathbf{r}-i\mathbf{k}'\mathbf{r}} G(\mathbf{k}, \mathbf{k}', iw) \\ &= G_0(0, iw) + G_0(\mathbf{r}, iw)T(iw)G_0(-\mathbf{r}, iw) \end{aligned} \tag{4.9}$$

from which we can calculate the local density of states(LDOS):

$$\rho(\mathbf{r}, E) = -\frac{1}{\pi}\mathrm{Im}G(\mathbf{r}, \mathbf{r}, E + i0^+) \tag{4.10}$$

For the superfluid phase, we write the BCS mean field Hamiltonian in Nambu notation as a 2×2 matrix:

$$\begin{aligned} H &= H_0 + W \\ &= \sum_{\mathbf{k}} (c^+_{\mathbf{k}\uparrow}, c_{-\mathbf{k}\downarrow}) \begin{pmatrix} \epsilon(\mathbf{k}) & \Delta(\mathbf{k}) \\ \Delta(\mathbf{k})^* & -\epsilon(\mathbf{k}) \end{pmatrix} \begin{pmatrix} c_{\mathbf{k}\uparrow} \\ c^+_{-\mathbf{k}\downarrow} \end{pmatrix} \\ &\quad + \frac{1}{V}\sum_{\mathbf{k},\mathbf{k}'} (c^+_{\mathbf{k}\uparrow}, c_{-\mathbf{k}\downarrow}) \begin{pmatrix} u & 0 \\ 0 & -u \end{pmatrix} \begin{pmatrix} c_{\mathbf{k}'\uparrow} \\ c^+_{-\mathbf{k}'\downarrow} \end{pmatrix} \end{aligned} \tag{4.11}$$

Here we introduce the Nambu spinor: $(c^+_{\mathbf{k}\uparrow}, c_{-\mathbf{k}\downarrow})$. The impurity potential here is non-magnetic and has the form of $u\tau_3$. For a magnetic impurity, it has the form of $u\tau_0$.

Let us define the matrix Green's function as:

$$G(\mathbf{k}, \mathbf{k}, \tau) = -\langle T_\tau \begin{pmatrix} c_{\mathbf{k}\uparrow}(\tau)c^+_{\mathbf{k}\uparrow}(0) & c_{\mathbf{k}\uparrow}(\tau)c_{-\mathbf{k}\downarrow}(0) \\ c^+_{-\mathbf{k}\downarrow}(\tau)c^+_{\mathbf{k}\uparrow}(0) & c^+_{-\mathbf{k}\downarrow}(\tau)c_{-\mathbf{k}\downarrow}(0) \end{pmatrix} \rangle \tag{4.12}$$

We are interested in the local density of states, which is given by

$$\rho(\mathbf{r}, E) = -\frac{1}{\pi}\mathrm{Im}G_{11}(\mathbf{r}, \mathbf{r}, E + i0^+) + \frac{1}{\pi}\mathrm{Im}G_{22}(\mathbf{r}, \mathbf{r}, -E - i0^+) \tag{4.13}$$

Where the first term corresponds to the local density of states for spin up atoms and the second term for spin down atoms. Since the local density of states is independent of spin directions in the balanced case with non-magnetic impurities, we have:

$$-\frac{1}{\pi}\mathrm{Im}G_{11}(\mathbf{r},\mathbf{r},E+i0^+)=\frac{1}{\pi}\mathrm{Im}G_{22}(\mathbf{r},\mathbf{r},-E-i0^+) \tag{4.14}$$

We now calculate the unperturbed Green's function:

$$\begin{aligned} G_0(\mathbf{k},iw_n) &= \langle\mathbf{k}|\frac{1}{iw_n-H_0}|\mathbf{k}\rangle = \begin{pmatrix} iw_n-\xi_{\mathbf{k}} & -\Delta \\ -\Delta^* & iw_n+\xi_{\mathbf{k}} \end{pmatrix}^{-1} \\ &= \frac{1}{(iw_n)^2-\xi_{\mathbf{k}}^2-\Delta}\begin{pmatrix} iw_n+\xi_{\mathbf{k}} & \Delta \\ \Delta^* & iw_n-\xi_{\mathbf{k}} \end{pmatrix} \end{aligned} \tag{4.15}$$

The T matrix is

$$\begin{aligned} T(iw_n) &= u\tau_3+u\tau_3G_0(0,iw_n)u\tau_3+u\tau_3G_0(0,iw_n)u\tau_3G_0(0,iw_n)u\tau_3+\cdots \\ &= u\tau_3+u\tau_3G_0(0,iw_n)T(iw_n) \\ &= (1-u\tau_3G_0(0,iw_n))^{-1}u\tau_3 \end{aligned} \tag{4.16}$$

So

$$\begin{aligned} T^{-1}(iw_n) &= \frac{1}{u}\tau_3(1-u\tau_3G_0(0,iw_n)) \\ &= \frac{1}{u}\tau_3-G_0(0,iw_n) \end{aligned} \tag{4.17}$$

where

$$\begin{aligned} G_0(0,iw_n) &= \frac{1}{V}\sum_{\mathbf{k}}G_0(\mathbf{k},iw_n) \\ &= \begin{bmatrix} \frac{1}{V}\sum_{\mathbf{k}}\frac{iw_n+\xi_{\mathbf{k}}}{(iw_n)^2-\xi_{\mathbf{k}}^2-\Delta^2} & \frac{1}{V}\sum_{\mathbf{k}}\frac{\Delta}{(iw_n)^2-\xi_{\mathbf{k}}^2-\Delta^2} \\ \frac{1}{V}\sum_{\mathbf{k}}\frac{\Delta^*}{(iw_n)^2-\xi_{\mathbf{k}}^2-\Delta^2} & \frac{1}{V}\sum_{\mathbf{k}}\frac{iw_n-\xi_{\mathbf{k}}}{(iw_n)^2-\xi_{\mathbf{k}}^2-\Delta^2} \end{bmatrix} \end{aligned} \tag{4.18}$$

So the inverse of the T-matrix can be written as

$$T^{-1}(iw_n) = \begin{bmatrix} \frac{1}{u} - \frac{1}{V}\sum_{\mathbf{k}} \frac{iw_n+\xi_{\mathbf{k}}}{(iw_n)^2-\xi_{\mathbf{k}}^2-\Delta^2} & -\frac{1}{V}\sum_{\mathbf{k}} \frac{\Delta}{(iw_n)^2-\xi_{\mathbf{k}}^2-\Delta^2} \\ -\frac{1}{V}\sum_{\mathbf{k}} \frac{\Delta^*}{(iw_n)^2-\xi_{\mathbf{k}}^2-\Delta^2} & -\frac{1}{u} - \frac{1}{V}\sum_{\mathbf{k}} \frac{iw_n-\xi_{\mathbf{k}}}{(iw_n)^2-\xi_{\mathbf{k}}^2-\Delta^2} \end{bmatrix} \tag{4.19}$$

The problem now is to do the integral. This can be analytically calculated using a contour integral. Here I show the results for the 1D superfluid. The results for 3D are similar. As for the BEC-BCS crossover, the chemical potential can be both positive and negative. We have to divide the integral into many cases.

Case 1. when $|w| < \Delta$

We can define $\epsilon = \sqrt{-w^2+\Delta^2}$

We find that all the imaginary parts are zero. This is true because here we are considering s-wave pairing which does not have nodes. Inside the gap, the imaginary part of Green's function should be zero.

Case 1.1 when $\mu > 0$

$$\mathrm{Re}G_0(0, w+i0^+)_{11} = \frac{(\epsilon+w)\cos(\frac{1}{2}\arctan(\frac{\mu}{\epsilon})) - (\epsilon-w)\sin(\frac{1}{2}\arctan(\frac{\mu}{\epsilon}))}{2\sqrt{2}\epsilon(\epsilon^2+\mu^2)^{1/4}} \tag{4.20}$$

$$\mathrm{Re}G_0(0, w+i0^+)_{12} = \frac{\Delta[\sqrt{\epsilon\mu(\epsilon+\sqrt{\epsilon^2+\mu^2})} + (\epsilon^2+\mu^2)^{1/4}\sqrt{\frac{\epsilon\mu^3}{\mu^2+\epsilon(\epsilon+\sqrt{\epsilon^2+\mu^2})}}]}{4\sqrt{\epsilon^3\mu(\epsilon^2+\mu^2)}} \tag{4.21}$$

$$\mathrm{Re}G_0(0, w+i0^+)_{22} = \frac{(\epsilon-w)\cos(\frac{1}{2}\arctan(\frac{\mu}{\epsilon})) - (\epsilon+w)\sin(\frac{1}{2}\arctan(\frac{\mu}{\epsilon}))}{2\sqrt{2}\epsilon(\epsilon^2+\mu^2)^{1/4}} \tag{4.22}$$

Case 1.2 when $\mu < 0$

$$\mathrm{Re}G_0(0, w+i0^+)_{11} = -\frac{1}{2}\sqrt{\frac{-\mu+\sqrt{\epsilon^2+\mu^2}}{2(\epsilon^2+\mu^2)}} + \frac{w\sin[\frac{1}{2}\arctan(\frac{\epsilon}{\mu})]}{2\epsilon(\epsilon^2+\mu^2)^{1/4}} \tag{4.23}$$

$$\mathrm{Re}G_0(0, w+i0^+)_{12} = \frac{\Delta\sin[\frac{1}{2}\arctan(\frac{\epsilon}{\mu})]}{2\epsilon(\epsilon^2+\mu^2)^{1/4}} \tag{4.24}$$

$$\mathrm{Re}G_0(0, w+i0^+)_{22} = \frac{1}{2}\sqrt{\frac{-\mu+\sqrt{\epsilon^2+\mu^2}}{2(\epsilon^2+\mu^2)}} + \frac{w\sin[\frac{1}{2}\arctan(\frac{\epsilon}{\mu})]}{2\epsilon(\epsilon^2+\mu^2)^{1/4}} \tag{4.25}$$

Case 2. when $|w| > \Delta$

Define $\varepsilon_{\pm} = \pm\sqrt{w^2 - \Delta^2}$

For imaginary parts, we have to deal with the delta function using

$$\delta(f(x)) = \sum_i \frac{\delta(x - x_i)}{|f'(x_i)|} \tag{4.26}$$

where the x_i are roots for $f(x) = 0$. We get

Case 2.1 when $-\mu > \varepsilon_+$

The imaginary parts are zero.

$$\mathrm{Re}G_0(0, w + i0^+)_{11} = -\frac{\varepsilon_+(\frac{1}{\sqrt{-\varepsilon_+ - \mu}} + \frac{1}{\sqrt{\varepsilon_+ - \mu}}) + w(\frac{1}{\sqrt{-\varepsilon_+ - \mu}} - \frac{1}{\sqrt{\varepsilon_+ - \mu}})}{4\varepsilon_+} \tag{4.27}$$

$$\mathrm{Re}G_0(0, w + i0^+)_{12} = \frac{\Delta(\sqrt{-\varepsilon_+ - \mu} - \sqrt{\varepsilon_+ - \mu})}{4\varepsilon_+\sqrt{-\varepsilon_+^2 + \mu^2}} \tag{4.28}$$

$$\mathrm{Re}G_0(0, w + i0^+)_{22} = \frac{\varepsilon_+(\frac{1}{\sqrt{-\varepsilon_+ - \mu}} + \frac{1}{\sqrt{\varepsilon_+ - \mu}}) + w(-\frac{1}{\sqrt{-\varepsilon_+ - \mu}} + \frac{1}{\sqrt{\varepsilon_+ - \mu}})}{4\varepsilon_+} \tag{4.29}$$

Case 2.2 when $\varepsilon_- < -\mu < \varepsilon_+$

$$\mathrm{Re}G_0(0, w + i0^+)_{11} = \frac{-\varepsilon_+ + w}{4\varepsilon_+\sqrt{\varepsilon_+ - \mu}} \tag{4.30}$$

$$\mathrm{Re}G_0(0, w + i0^+)_{12} = \frac{\Delta}{4\varepsilon_+\sqrt{\varepsilon_+ - \mu}} \tag{4.31}$$

$$\mathrm{Re}G_0(0, w + i0^+)_{22} = \frac{\varepsilon_+ + w}{4\varepsilon_+\sqrt{\varepsilon_+ - \mu}} \tag{4.32}$$

when $w < 0$

$$\mathrm{Im}G_0(0, w + i0^+)_{11} = \frac{1}{\sqrt{\varepsilon_+ + \mu}}\frac{w + \varepsilon_+}{4\varepsilon_+} \tag{4.33}$$

$$\mathrm{Im}G_0(0, w + i0^+)_{12} = \frac{1}{\sqrt{\varepsilon_+ + \mu}}\frac{\Delta}{4\varepsilon_+} \tag{4.34}$$

$$\mathrm{Im}G_0(0, w + i0^+)_{22} = \frac{1}{\sqrt{\varepsilon_+ + \mu}}\frac{w - \varepsilon_+}{4\varepsilon_+} \tag{4.35}$$

when $w > 0$

$$\mathrm{Im}G_0(0, w + i0^+)_{11} = -\frac{1}{\sqrt{\varepsilon_+ + \mu}} \frac{w + \varepsilon_+}{4\varepsilon_+} \tag{4.36}$$

$$\mathrm{Im}G_0(0, w + i0^+)_{12} = -\frac{1}{\sqrt{\varepsilon_+ + \mu}} \frac{\Delta}{4\varepsilon_+} \tag{4.37}$$

$$\mathrm{Im}G_0(0, w + i0^+)_{22} = -\frac{1}{\sqrt{\varepsilon_+ + \mu}} \frac{w - \varepsilon_+}{4\varepsilon_+} \tag{4.38}$$

Case 2.3 when $-\mu < \varepsilon_-$

All the real parts are zero.

when $w < 0$

$$\mathrm{Im}G_0(0, w + i0^+)_{11} = \frac{1}{\sqrt{\varepsilon_+ + \mu}} \frac{w + \varepsilon_+}{4\varepsilon_+} + \frac{1}{\sqrt{-\varepsilon_+ + \mu}} \frac{w - \varepsilon_+}{4\varepsilon_+} \tag{4.39}$$

$$\mathrm{Im}G_0(0, w + i0^+)_{12} = \frac{1}{\sqrt{\varepsilon_+ + \mu}} \frac{\Delta}{4\varepsilon_+} + \frac{1}{\sqrt{-\varepsilon_+ + \mu}} \frac{\Delta}{4\varepsilon_+} \tag{4.40}$$

$$\mathrm{Im}G_0(0, w + i0^+)_{22} = \frac{1}{\sqrt{\varepsilon_+ + \mu}} \frac{w - \varepsilon_+}{4\varepsilon_+} + \frac{1}{\sqrt{-\varepsilon_+ + \mu}} \frac{w + \varepsilon_+}{4\varepsilon_+} \tag{4.41}$$

when $w > 0$

$$\mathrm{Im}G_0(0, w + i0^+)_{11} = -\frac{1}{\sqrt{\varepsilon_+ + \mu}} \frac{w + \varepsilon_+}{4\varepsilon_+} - \frac{1}{\sqrt{-\varepsilon_+ + \mu}} \frac{w - \varepsilon_+}{4\varepsilon_+} \tag{4.42}$$

$$\mathrm{Im}G_0(0, w + i0^+)_{12} = -\frac{1}{\sqrt{\varepsilon_+ + \mu}} \frac{\Delta}{4\varepsilon_+} - \frac{1}{\sqrt{-\varepsilon_+ + \mu}} \frac{\Delta}{4\varepsilon_+} \tag{4.43}$$

$$\mathrm{Im}G_0(0, w + i0^+)_{22} = -\frac{1}{\sqrt{\varepsilon_+ + \mu}} \frac{w - \varepsilon_+}{4\varepsilon_+} - \frac{1}{\sqrt{-\varepsilon_+ + \mu}} \frac{w + \varepsilon_+}{4\varepsilon_+} \tag{4.44}$$

With all these we can first get the inverse of T-matrix. Then by using the form for Green's function, we can get Green's function at the impurity point. Using the T-matrix method we can get analytical results. This T-matrix method can only solve analytically for the case of a contact impurity. For a more general impurity, we need a more efficient method, that is, the Bogoliubov-de Gennes(B-dG) method.

4.3 The Hybrid Bogoliubov-de Gennes Method

The Bogoliubov-de Gennes(B-dG) method is a powerful tool to calculate the pairing gap and other physical properties for inhomogeneous systems[122, 123, 124, 125, 126]. It is extremely useful in cold atoms as the system is in the trap. Here I derive the hybrid B-dG method which deals with the renormalization and is more efficient. This method introduces an energy cut-off E_c in the calculation. Below the cut-off, it uses the standard B-dG to discretize the system; above the cut-off, it uses the local density approximation(LDA) to solve the system continuously. In this chapter, we use the B-dG method to treat both a localized impurity and an extended impurity.

4.3.1 Below Cut-off: Bogoliubov-de Gennes Method

As we will introduce the magnetic impurity, it breaks population balance in the system. The chemical potentials are different for different species.

We start from the the Hamiltonian

$$\begin{aligned} H &= \sum_{\sigma} \int d\mathbf{r} \psi_{\sigma}^{+}(\mathbf{r})[-\frac{\hbar^2\nabla^2}{2m} - \mu_{\sigma} - V(\mathbf{r})]\psi_{\sigma}(\mathbf{r}) \\ &\quad + g \int d\mathbf{r} \psi_{\uparrow}^{+}(\mathbf{r})\psi_{\downarrow}^{+}(\mathbf{r})\psi_{\downarrow}(\mathbf{r})\psi_{\uparrow}(\mathbf{r}) \end{aligned} \tag{4.45}$$

where ψ_{σ}^{+} is Fermion creation operator for "spin σ" atom, ψ_{σ} is Fermion annihilation operator for "spin σ" atom, g is the contact interaction strength.

We treat this first part as H_0, $H = H_0 + V$. We use the set of eigenstates $\{\eta\}$ for H_0, then the first part can be written as:

$$H_0 = \sum_{\eta,\sigma} \varepsilon_{\eta\sigma}^{0} c_{\eta\sigma}^{+} c_{\eta\sigma} \tag{4.46}$$

where $\psi_{\sigma}(\mathbf{r}) = \sum_{\eta} \langle \mathbf{r}|\eta\rangle c_{\eta\sigma}$. In a cold atom system, the basis set is the one for the harmonic trap potential.

The interaction part can be written as

$$V = \sum_{\eta_1\eta_2\eta_3\eta_4} \langle \eta_1\eta_2|U|\eta_3\eta_4\rangle c^+_{\eta_1\uparrow} c^+_{\eta_2\downarrow} c_{\eta_3\downarrow} c_{\eta_4\uparrow} \tag{4.47}$$

where we define

$$\langle \eta_1\eta_2|U|\eta_3\eta_4\rangle = g \int d\mathbf{r} \langle \eta_1|\mathbf{r}\rangle\langle \eta_2|\mathbf{r}\rangle\langle \mathbf{r}|\eta_3\rangle\langle \mathbf{r}|\eta_4\rangle \tag{4.48}$$

Here we adopt the mean-field approximation. As there is no spin flip mechanism in the Hamiltonian, there is no Fock term. We define the Hartree term

$$U_\sigma(\eta\eta') = \sum_{\eta_1\eta_2} \langle \eta_1\eta|U|\eta'\eta_2\rangle\langle c^+_{\eta_1\sigma} c_{\eta_2\sigma}\rangle \tag{4.49}$$

and the pairing term

$$\Delta^*(\eta\eta') = -\sum_{\eta_1\eta_2} \langle \eta_1\eta_2|U|\eta\eta'\rangle\langle c^+_{\eta_1\uparrow} c^+_{\eta_2\downarrow}\rangle \tag{4.50}$$

The mean-field Hamiltonian has the form:

$$\begin{aligned} H_{eff} &= \sum_{\eta,\sigma} \varepsilon^0_{\eta\sigma} c^+_{\eta\sigma} c_{\eta\sigma} + \sum_{\eta\eta'} [U_\uparrow(\eta\eta') c^+_{\eta\downarrow} c_{\eta'\downarrow} + U_\downarrow(\eta\eta') c^+_{\eta\uparrow} c_{\eta'\uparrow} \\ &\quad -\Delta^*(\eta\eta') c_{\eta\downarrow} c_{\eta'\uparrow} - \Delta(\eta\eta') c^+_{\eta\uparrow} c^+_{\eta'\downarrow}] \end{aligned} \tag{4.51}$$

Here we have omitted the constant terms. Defining

$$\begin{aligned} V_\uparrow(\eta\eta') &= \varepsilon^0_{\eta\uparrow}\delta_{\eta\eta'} + U_\downarrow(\eta\eta') \\ V_\downarrow(\eta\eta') &= \varepsilon^0_{\eta\downarrow}\delta_{\eta\eta'} + U_\uparrow(\eta\eta') \end{aligned} \tag{4.52}$$

we can write the Hamiltonian using the Nambu spinor.

$$\begin{aligned} H_{eff} &= \sum_{\eta\eta'} [V_\uparrow(\eta\eta') c^+_{\eta\uparrow} c_{\eta'\uparrow} - V_\downarrow(\eta'\eta) c_{\eta\downarrow} c^+_{\eta'\downarrow} \\ &\quad -\Delta^*(\eta\eta') c_{\eta\downarrow} c_{\eta'\uparrow} - \Delta(\eta\eta') c^+_{\eta\uparrow} c^+_{\eta'\downarrow}] \\ &= \sum_{\eta\eta'} [c^+_{\eta\uparrow}, c_{\eta\downarrow}] \begin{bmatrix} V_\uparrow(\eta\eta') & -\Delta(\eta\eta') \\ -\Delta^*(\eta\eta') & -V_\downarrow(\eta'\eta) \end{bmatrix} \begin{bmatrix} c_{\eta'\uparrow} \\ c^+_{\eta'\downarrow} \end{bmatrix} \end{aligned} \tag{4.53}$$

We need to diagonalize this matrix, but first we need a cut-off for the system. Say we only consider the lowest N There are $2N$ eigenvalues. The maximum(minimum) value should be equal to the cut-off energy E_c(In real numerical calculations, due to the computational accuracy, we usually diagonalize a much larger matrix, and only consider states with energy less than cut-off energy).

To diagonalize the matrix, we introduce a unitary transform U.

$$H_{eff} = \sum_{\eta\eta'=1,N} [c^+_{\eta\uparrow}, c_{\eta\downarrow}] UU^+ \begin{bmatrix} V_\uparrow(\eta\eta') & -\Delta(\eta\eta') \\ -\Delta^*(\eta\eta') & -V_\downarrow(\eta'\eta) \end{bmatrix} UU^+ \begin{bmatrix} c_{\eta'\uparrow} \\ c^+_{\eta'\downarrow} \end{bmatrix} \tag{4.54}$$

Assume

$$\begin{bmatrix} V_\uparrow(\eta\eta') & -\Delta(\eta\eta') \\ -\Delta^*(\eta\eta') & -V_\downarrow(\eta'\eta) \end{bmatrix}_{2N\times 2N} \begin{bmatrix} u_{\eta'} \\ v_{\eta'} \end{bmatrix}_{2N\times 1} = E \begin{bmatrix} u_\eta \\ v_\eta \end{bmatrix}_{2N\times 1} \tag{4.55}$$

where E is eigenvalue, $u_{\eta'}, v_{\eta'}$ are eigenstates with $\sum_{\eta'}(|u_{\eta'}|^2 + |v_{\eta'}|^2) = 1$. It has $2N$ sets of eigenvalues and eigenstates. Defining the unitary matrix:

$$U = \begin{bmatrix} u_{\eta n} \\ v_{\eta n} \end{bmatrix} \tag{4.56}$$

where $\eta = 1, ...N$, $n = 1, ...2N$.

$$U^+ = [u^*_{n\eta}, v^*_{n\eta}] \tag{4.57}$$

We have

$$\begin{bmatrix} \gamma_{\eta\uparrow} \\ \gamma^+_{\eta\downarrow} \end{bmatrix} = U^+ \begin{bmatrix} c_{\eta\uparrow} \\ c^+_{\eta\downarrow} \end{bmatrix} \tag{4.58}$$

$$\tag{4.59}$$

We get

$$\begin{aligned} c_{\eta\uparrow} &= \sum_{n=1,N} u_{\eta n}\gamma_{n\uparrow} + \sum_{n=1,N} u_{\eta,N+n}\gamma^{+}_{n\downarrow} \\ c^{+}_{\eta\uparrow} &= \sum_{n=1,N} u^{*}_{\eta n}\gamma^{+}_{n\uparrow} + \sum_{n=1,N} u^{*}_{\eta,N+n}\gamma_{n\downarrow} \\ c^{+}_{\eta\downarrow} &= \sum_{n=1,N} v_{\eta n}\gamma_{n\uparrow} + \sum_{n=1,N} v_{\eta,N+n}\gamma^{+}_{n\downarrow} \\ c_{\eta\downarrow} &= \sum_{n=1,N} v^{*}_{\eta n}\gamma^{+}_{n\uparrow} + \sum_{n=1,N} v^{*}_{\eta,N+n}\gamma_{n\downarrow} \end{aligned} \tag{4.60}$$

The mean-field Hamiltonian can be diagonalized

$$\begin{aligned} H_{eff} &= \sum_{\eta\eta'} [\gamma^{+}_{\eta\uparrow}, \gamma_{\eta\downarrow}] \begin{bmatrix} \cdot & 0 & 0 \\ 0 & E & 0 \\ 0 & 0 & \cdot \end{bmatrix} \begin{bmatrix} \gamma_{\eta'\uparrow} \\ \gamma^{+}_{\eta'\downarrow} \end{bmatrix} \\ &= \sum_{\eta=1,N} E_{\eta}\gamma^{+}_{\eta\uparrow}\gamma_{\eta\uparrow} - \sum_{\eta=1,N} E_{N+\eta}\gamma^{+}_{\eta\downarrow}\gamma_{\eta\downarrow} \end{aligned} \tag{4.61}$$

Now we derive the density profile for different species.

$$\langle n_{\uparrow}(x)\rangle = \sum_{n=1,2N} (\sum_{\eta} \langle \eta|x\rangle u^{*}_{\eta n})(\sum_{\eta'} \langle x|\eta'\rangle u_{\eta' n}) f(E_n) \tag{4.62}$$

$$\langle n_{\downarrow}(x)\rangle = \sum_{n=1,2N} (\sum_{\eta} \langle \eta|x\rangle v_{\eta n})(\sum_{\eta'} \langle x|\eta'\rangle v^{*}_{\eta' n}) f(-E_n) \tag{4.63}$$

The gap profile is

$$\Delta(x) = -g \sum_{n=1,2N} (\sum_{\eta} \langle x|\eta\rangle v^{*}_{\eta n})(\sum_{\eta'} \langle x|\eta'\rangle u_{\eta' n}) f(E_n) \tag{4.64}$$

and the local density of states(LDOS) is given by

$$\rho_{\uparrow}(r, iw_n \rightarrow w + i0^{+}) = \sum_{\eta,\eta'} \langle r|\eta\rangle\langle\eta'|r\rangle \sum_{n=1,2N} u_{\eta n}u^{*}_{\eta' n}\delta(w - E_n) \tag{4.65}$$

4.3.2 Above Cut-off: Local Density Approximation

For the local density approximation(LDA), we assume at each site the system is homogeneous and the momentum is a good quantum number. The trapping potential can be put in the chemical potential $\mu(\mathbf{r}) = \mu - V_{trap}(\mathbf{r})$.

For an imbalanced system, the chemical potential is different for different species. $\mu_\uparrow(\mathbf{r}) = \mu(\mathbf{r}) + \delta\mu$, $\mu_\downarrow(\mathbf{r}) = \mu(\mathbf{r}) - \delta\mu$. We have the Hamiltonian at each site

$$H = \sum_{\mathbf{k}} [c^+_{\mathbf{k}\uparrow}, c_{-\mathbf{k}\downarrow}] \begin{bmatrix} \epsilon_{\mathbf{k}} - \mu(\mathbf{r}) - \delta\mu & -\Delta(\mathbf{r}) \\ -\Delta(\mathbf{r})^* & -\epsilon_{\mathbf{k}} + \mu(\mathbf{r}) - \delta\mu \end{bmatrix} \begin{bmatrix} c_{\mathbf{k}\uparrow} \\ c^+_{-\mathbf{k}\downarrow} \end{bmatrix} \tag{4.66}$$

We can calculate the eigenstate

$$\begin{bmatrix} \epsilon_{\mathbf{k}} - \mu(\mathbf{r}) - \delta\mu - E(\mathbf{r}) & -\Delta(\mathbf{r}) \\ -\Delta(\mathbf{r})^* & -\epsilon_{\mathbf{k}} + \mu(\mathbf{r}) - \delta\mu - E(\mathbf{r}) \end{bmatrix} \begin{bmatrix} u_{\mathbf{k}}(\mathbf{r}) \\ v_{\mathbf{k}}(\mathbf{r}) \end{bmatrix} = 0 \tag{4.67}$$

We get

$$\begin{aligned} E &= -\delta\mu \pm E_{\mathbf{k}} \\ &= -\delta\mu \pm \sqrt{(\epsilon_{\mathbf{k}} - \mu)^2 + |\Delta|^2} \end{aligned} \tag{4.68}$$

The first eigenvalue and eigenstate:

$$\begin{aligned} E_1(\mathbf{r}) &= -\delta\mu + E_{\mathbf{k}}(\mathbf{r}) \\ u_1(\mathbf{r}) &= \frac{-\Delta(\mathbf{r})}{\sqrt{2E_{\mathbf{k}}(\mathbf{r})(E_{\mathbf{k}}(\mathbf{r}) - \epsilon_{\mathbf{k}} + \mu(\mathbf{r}))}} \\ v_1(\mathbf{r}) &= \frac{E_{\mathbf{k}}(\mathbf{r}) - \epsilon_{\mathbf{k}} + \mu(\mathbf{r})}{\sqrt{2E_{\mathbf{k}}(\mathbf{r})(E_{\mathbf{k}}(\mathbf{r}) - \epsilon_{\mathbf{k}} + \mu(\mathbf{r}))}} \end{aligned} \tag{4.69}$$

The second eigenvalue and eigenstate:

$$\begin{aligned} E_2(\mathbf{r}) &= -\delta\mu - E_{\mathbf{k}}(\mathbf{r}) \\ u_2(\mathbf{r}) &= \frac{\Delta(\mathbf{r})}{\sqrt{2E_{\mathbf{k}}(\mathbf{r})(E_{\mathbf{k}}(\mathbf{r}) + \epsilon_{\mathbf{k}} - \mu(\mathbf{r}))}} \\ v_2(\mathbf{r}) &= \frac{E_{\mathbf{k}}(\mathbf{r}) + \epsilon_{\mathbf{k}} - \mu(\mathbf{r})}{\sqrt{2E_{\mathbf{k}}(\mathbf{r})(E_{\mathbf{k}}(\mathbf{r}) + \epsilon_{\mathbf{k}} - \mu(\mathbf{r}))}} \end{aligned} \tag{4.70}$$

where $E_{\mathbf{k}}(\mathbf{r}) = \sqrt{(\epsilon_{\mathbf{k}} - \mu(\mathbf{r}))^2 + |\Delta(\mathbf{r})|^2}$

The density and gap are given by.

$$\begin{aligned}
\langle n_{\mathbf{k}\uparrow}(\mathbf{r})\rangle &= |u_1(\mathbf{r})|^2 f(E_{\mathbf{k}}(\mathbf{r}) - \delta\mu) + |u_2(\mathbf{r})|^2[1 - f(E_{\mathbf{k}}(\mathbf{r}) + \delta\mu)] \\
&\overset{T=0}{=} |u_2(\mathbf{r})|^2 \theta(E_{\mathbf{k}}(\mathbf{r}) + \delta\mu) \\
&= \frac{1}{2}(1 - \frac{\epsilon_{\mathbf{k}} - \mu(\mathbf{r})}{E_{\mathbf{k}}(\mathbf{r})})\theta(E_{\mathbf{k}}(\mathbf{r}) + \delta\mu) \qquad (4.71)
\end{aligned}$$

$$\begin{aligned}
\langle n_{\mathbf{k}\downarrow}(\mathbf{r})\rangle &= |v_1(\mathbf{r})|^2[1 - f(\mathbf{k}_k(\mathbf{r}) - \delta\mu)] + |v_2(\mathbf{r})|^2 f(E_{\mathbf{k}}(\mathbf{r}) + \delta\mu) \\
&\overset{T=0}{=} |v_1(\mathbf{r})|^2 \theta(E_{\mathbf{k}}(\mathbf{r}) - \delta\mu) \\
&= \frac{1}{2}(1 - \frac{\epsilon_{\mathbf{k}} - \mu(\mathbf{r})}{E_{\mathbf{k}}(\mathbf{r})})\theta(E_{\mathbf{k}}(\mathbf{r}) - \delta\mu) \qquad (4.72)
\end{aligned}$$

$$\begin{aligned}
\Delta(\mathbf{r}) &= -g\sum_{\mathbf{k}} \langle c_{-\mathbf{k}\downarrow} c_{\mathbf{k}\uparrow}\rangle \\
&= -g\sum_{\mathbf{k}} \frac{\Delta(\mathbf{r})}{2E_{\mathbf{k}}(\mathbf{r})}(E_{\mathbf{k}}(\mathbf{r}) + \delta\mu) \qquad (4.73)
\end{aligned}$$

4.3.3 Summary

Below is a summary of the whole procedure of the hybrid Bogoliubov-de Gennes method.

(a). Start with an initial guess of $\Delta(\mathbf{r})$ and $\langle n_\sigma(\mathbf{r})\rangle$. We can calculate the gap component and Hartree component for the B-dG part.

$$\begin{aligned}
\Delta(\eta\eta') &= \int d\mathbf{r}\langle\eta|\mathbf{r}\rangle\langle\eta'|\mathbf{r}\rangle\Delta(\mathbf{r}) \\
U_\sigma(\eta\eta') &= g\int d\mathbf{r}\langle\eta|\mathbf{r}\rangle\langle\mathbf{r}|\eta'\rangle\langle n_\sigma(\mathbf{r})\rangle \qquad (4.74)
\end{aligned}$$

(b). Diagonalize the matrix:

$$\begin{bmatrix} V_\uparrow(\eta\eta') & -\Delta(\eta\eta') \\ -\Delta^*(\eta\eta') & -V_\downarrow(\eta'\eta) \end{bmatrix}_{2N\times 2N} \begin{bmatrix} u_{\eta'} \\ v_{\eta'} \end{bmatrix}_{2N\times 1} = E \begin{bmatrix} u_\eta \\ v_\eta \end{bmatrix}_{2N\times 1} \qquad (4.75)$$

to get $2N$ sets of eigenvalues and eigenstates.

(c). Calculate the new $\Delta(\mathbf{r})$ and $\langle n_\sigma(\mathbf{r})\rangle$

$$\Delta(\mathbf{r})_d = -g \sum_{n=1,2N} (\sum_{\eta} \langle \mathbf{r}|\eta\rangle v^*_{\eta n})(\sum_{\eta'} \langle \mathbf{r}|\eta'\rangle u_{\eta' n}) f(E_n) \tag{4.76}$$

$$\langle n_\uparrow(\mathbf{r})\rangle_d = \sum_{n=1,2N} (\sum_{\eta} \langle \eta|\mathbf{r}\rangle u^*_{\eta n})(\sum_{\eta'} \langle \mathbf{r}|\eta'\rangle u_{\eta' n}) f(E_n) \tag{4.77}$$

$$\langle n_\downarrow(\mathbf{r})\rangle_d = \sum_{n=1,2N} (\sum_{\eta} \langle \eta|\mathbf{r}\rangle v_{\eta n})(\sum_{\eta'} \langle \mathbf{r}|\eta'\rangle v^*_{\eta' n}) f(-E_n) \tag{4.78}$$

Above the cut-off, we have

$$\Delta(\mathbf{r})_c = -g \sum_{\mathbf{k}} \frac{\Delta(\mathbf{r})}{2E_{\mathbf{k}}(\mathbf{r})} \theta(E_{\mathbf{k}}(\mathbf{r}) + \delta\mu - E_c) \tag{4.79}$$

$$\langle n_\uparrow(\mathbf{r})\rangle_c = \sum_{\mathbf{k}} \frac{1}{2}(1 - \frac{\epsilon_{\mathbf{k}} - \mu(\mathbf{r})}{E_{\mathbf{k}}(\mathbf{r})}) \theta(E_{\mathbf{k}}(\mathbf{r}) + \delta\mu - E_c) \tag{4.80}$$

$$\langle n_\downarrow(\mathbf{r})\rangle_c = \sum_{\mathbf{k}} \frac{1}{2}(1 - \frac{\epsilon_{\mathbf{k}} - \mu(\mathbf{r})}{E_{\mathbf{k}}(\mathbf{r})}) \theta(E_{\mathbf{k}}(\mathbf{r}) - \delta\mu - E_c) \tag{4.81}$$

where $E_{\mathbf{k}} = \sqrt{(\epsilon_{\mathbf{k}} - \mu(\mathbf{r}))^2 + |\Delta(\mathbf{r})|^2}$. As $\Delta(\mathbf{r}) = \Delta(\mathbf{r})_d + \Delta(\mathbf{r})_c$ and $\langle n_\sigma(\mathbf{r})\rangle = \langle n_\sigma(\mathbf{r})\rangle_d + \langle n_\sigma(\mathbf{r})\rangle_c$.

$$\Delta(\mathbf{r}) = -g^{eff} \sum_{n=1,2N} (\sum_{\eta} \langle \mathbf{r}|\eta\rangle v^*_{\eta n})(\sum_{\eta'} \langle \mathbf{r}|\eta'\rangle u_{\eta' n}) f(E_n) \tag{4.82}$$

where

$$\frac{1}{g^{eff}} = \frac{1}{g} + \sum_{\mathbf{k}} \frac{1}{2E_{\mathbf{k}}(\mathbf{r})} \theta(E_{\mathbf{k}}(\mathbf{r}) + \delta\mu - E_c) \tag{4.83}$$

We can repeat all the procedures until the process converges. The chemical potentials μ and $\delta\mu$ are also adjusted in each iterative step to make the number conserve. By using this B-dG method, we take into account the trapping potential and the impurity completely self-consistently.

4.4 Localized Impurity

Let us first consider a localized impurity with $U_\sigma(x) = u_\sigma \delta(x)$ in a one dimensional system. If we restrict ourselves to the vicinity of the impurity, we may neglect the trapping potential and use the T-matrix formalism. As a result of the δ-function impurity potential, the T-matrix is momentum independent and analytical results can be obtained. The full Green's function G is related to the bare (without the impurity) Green's function G_0 and the T-matrix in the following way:

$$G(k, k', \omega) = G_0(k, \omega)\delta_{kk'} + G_0(k, \omega)T(\omega)G_0(k', \omega), \tag{4.84}$$

where ω is the frequency, k and k' represent the incoming and outgoing momenta in the scattering event, respectively. For the s-wave superfluid, we have:

$$G_0(k, w) = \frac{\omega\sigma_0 + (\epsilon_k - \tilde{\mu})\sigma_3 - \Delta\sigma_1}{\omega^2 - (\epsilon_k - \tilde{\mu})^2 - \Delta^2}, \tag{4.85}$$

where $\epsilon_k = \hbar^2 k^2/(2m)$, σ_i's are the Pauli matrices (σ_0 is the identity matrix) and Δ is the s-wave pairing gap. Here the effective chemical potential, $\tilde{\mu} = \mu - gn(x)$, includes the contribution from the Hartree term, where $n(x)$ is the local density for one spin species. For a magnetic impurity, we take $u = u_\uparrow = -u_\downarrow$and the T-matrix is given by:

$$T^{-1}(\omega) = u^{-1}\sigma_0 - \sum_k G_0(k, \omega)\,, \tag{4.86}$$

while for a non-magnetic impurity with $u = u_\uparrow = u_\downarrow$, and the corresponding T-matrix has the same form as in Eq. (4.86) with σ_0 replaced by σ_3. From the full Green's function, one can immediately obtain the local density of states (LDOS) at the impurity site as

$$\rho(\epsilon) = -\frac{1}{\pi}\sum_{k,k'} \mathrm{Im}\left[G(k, k', \epsilon + i0^+)\right]\,. \tag{4.87}$$

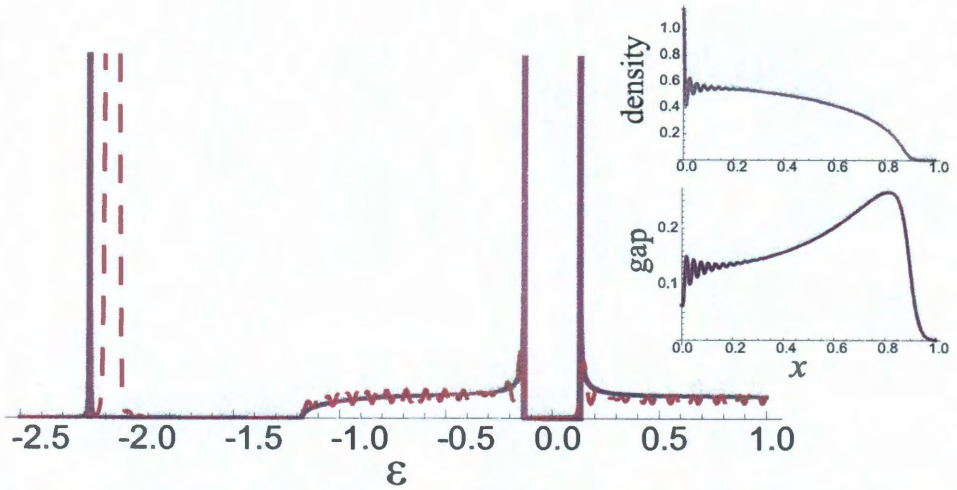

Figure 4.1 : Local density of state (arb. units) at the site of a localized non-magnetic impurity with $u = -0.02 E_F x_{TF}$, where E_F is the Fermi energy and $x_{TF} = \sqrt{N} a_{\rm ho}$ ($a_{\rm ho} = \sqrt{\hbar/(m\omega_0)}$) is the Thomas-Fermi radius of the non-interacting system. The dimensionless interaction parameter $\gamma = -mg/(\hbar^2 n_0) = 1.25$ where $n_0 = 2\sqrt{N}/(\pi a_{\rm ho})$ is the peak Thomas-Fermi density of the non-interacting system. $N = 100$ is the total number of particles. The two spin components have equal population. Solid and dashed lines represent results obtained using the T-matrix and B-dG method, respectively. The insets show the density and gap profile of the trapped system from the B-dG calculation. The units for density, energy and length are n_0, E_F and x_{TF}, respectively.

4.4.1 Non-magnetic Impurity

The solid line in Fig. 4.1 shows the LDOS at impurity site obtained from the T-matrix method for an attractive non-magnetic impurity with $u < 0$. The important features one can easily notice are the superfluid gap near $\epsilon = 0$ (the energy is measured relative to the Fermi energy), and a strong peak below the Fermi sea which represents the bound state induced by the impurity potential. The bound state energy can be obtained analytically as $E_0 = -\sqrt{[\tilde{\mu} + mu^2/(2\hbar^2)]^2 + \Delta^2}$. As the strength of the impurity potential $|u|$ increases, the bound state will move deeper below the Fermi sea.

To confirm that these results still hold when a trapping potential is present, as is always the case in the experiment, we add a harmonic potential $V_T = m\omega_0^2 x^2/2$ to the system and perform the calculation using the Bogoliubov-de Gennes (B-dG) method. The dashed line in Fig. 4.1 represents the LDOS at the non-magnetic impurity site ($x = 0$) calculated using the B-dG method. The agreement with the T-matrix method is satisfactory. The remaining discrepancies (in particular the position of the bound state) can be understood as the T-matrix method neglects the trapping potential and is not fully self-consistent: the values of the chemical potentials, densities and pairing gap used in the T-matrix calculation are taken to be those from the B-dG result in the absence of the impurity. The insets of Fig. 4.1 demonstrate the density and gap profiles of the trapped system. The Friedel oscillation with a spatial frequency close to $2k_F$, where k_F is the Fermi wave number, can be easily identified near the impurity.

4.4.2 Magnetic Impurity

The solid lines in Fig. 4.2(a),(b) display the LDOS at the magnetic impurity site for the two spin species obtained using the T-matrix method. Here the impurity potential is attractive (repulsive) for spin-up (down) atoms which creates a resonant state below the Fermi sea for spin up atoms manifested by the peak near $\epsilon = -2E_F$ in Fig. 4.2(a). As the strength of the impurity potential $|u|$ increases, the resonant state will move deeper below the Fermi sea. Besides this resonant state, both $\rho_\uparrow(\epsilon)$ and $\rho_\downarrow(\epsilon)$ exhibit an additional peak near $\epsilon = 0$, which signals the presence of a mid-gap bound state [127, 128, 129]. In the limit of weak interaction, the position of the mid-gap bound state is given by the T-matrix method as:

$$E_0 = \pm\Delta \frac{1 - (u\pi\rho_0/2)^2}{1 + (u\pi\rho_0/2)^2}, \tag{4.88}$$

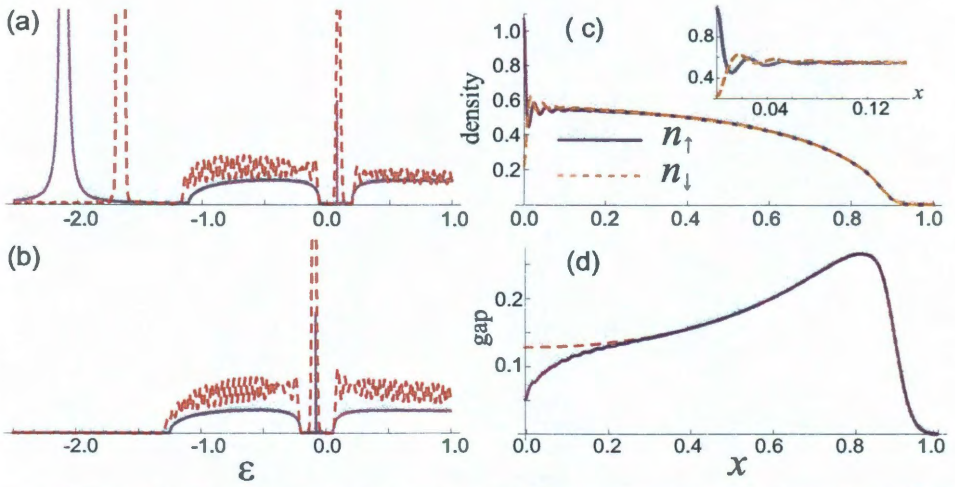

Figure 4.2 : (a) Density of states for spin up atoms. (b) Density of states for spin down atoms. (c) Density profiles for both spin species. (d) Gap profile. In (a) and (b) solid and dashed lines represent results obtained using the T-matrix and B-dG method, respectively. The dashed curve in (d) is the gap profile without the impurity. For all plots, $N_\uparrow = N_\downarrow = 50$, and $u = -0.02 E_F x_{TF}$, where E_F is the Fermi energy and $x_{TF} = \sqrt{N} a_{\rm ho}$ is the Thomas-Fermi radius of the non-interacting system. The harmonic oscillator length and Thomas Fermi density at the origin are defined by $a_{\rm ho} = \sqrt{\hbar/(m\omega_0)}$ and $n_0 = 2\sqrt{N}/(\pi a_{\rm ho})$. The dimensionless interaction parameter $\gamma = -mg/(\hbar^2 n_0) = 1.25$. The units for density, energy and length are n_0, E_F and x_{TF}, respectively.

where ρ_0 is the density of states at the Fermi sea, and the $+$ $(-)$ sign refers to the spin-up (-down) component. The mid-gap bound state is thus located outside the band and inside the pairing gap. As the strength of the impurity $|u|$ increases, the mid-gap moves from the upper gap edge to the lower gap edge for the spin-up component and moves oppositely for the spin-down component.

The dashed line in Fig. 4.2(a),(b) represents the LDOS at the magnetic impurity site ($x = 0$) calculated using the B-dG method. The agreement with the T-matrix method is satisfactory. The density and gap profiles of the trapped system are illustrated in Fig. 4.2(c),(d). Friedel oscillations with a spatial frequency close to $2k_F$ can

be seen in the density profiles near the impurity. The magnetic impurity tends to break Cooper pairs, leading to a reduced gap size near the impurity as can be seen from Fig. 4.2(d).

4.5 Detection of Mid-gap State

As we have seen above, the mid-gap bound state induced by a magnetic impurity manifests itself in the local density of states(LDOS). In general, the LDOS provides valuable information on the quantum system and it is highly desirable to measure it directly. Great dividends have been reaped in the study of high T_c superconductors where the scanning tunneling microscope (STM), which measures the differential current that is proportional to the LDOS, provides this function[130]. In ultra-cold Fermi gases, radio-frequency (RF) spectroscopy [69, 70, 39] could serve as an analogous tool. The RF field induces single-particle excitations by coupling one of the spin species (say $|\uparrow\rangle$ atoms) out of the pairing state to a third state $|3\rangle$ which is initially unoccupied. In the experiment, the RF signal is defined as the average rate change of the population in state $|\uparrow\rangle$ (or state $|3\rangle$) during the RF pulse. The first generation RF experiments had low resolution and provided averaged currents over the whole atomic cloud, which complicated interpretation of the signal due to the inhomogeneity of the sample [42]. More recently, spatially resolved RF spectroscopy which provides *local* information has been demonstrated [53]. Here we show that a modified implementation of spatially resolved RF spectroscopy can yield direct information of the LDOS and hence can serve as a powerful tool in the study of cold atom system.

To study the effect of the RF field, we include two additional parts to the total Hamiltonian (4.1):

$$H_3 = \int dx\, \psi_3^\dagger(x) \left[-\frac{\hbar^2}{2m}\frac{d^2}{dx^2} + V_3(x) - \nu - \mu_3 \right] \psi_3(x), \tag{4.89}$$

$$H_T = \int dx\, [T\psi_3^\dagger(x)\psi_\uparrow(x) + T\psi_\uparrow^\dagger(x)\psi_3(x)], \tag{4.90}$$

where H_3 represents the single-particle Hamiltonian of the state 3 (we assume that

atoms in state 3 do not interact with other atoms, so there is no final state effect), with V_3 being the trapping potential of the state and ν the detuning of the RF field from the atomic transition, H_T represents the coupling between state 3 and spin-up atoms. Since the RF photon wavelength is much larger than the typical size of the atomic cloud, the coupling strength T can be regarded as a spatially invariant constant. For weak RF coupling, one may use the linear response theory [64, 65, 131, 132, 133] to obtain the RF signal which is proportional to $I(x) = \frac{d}{dt}\langle\psi_3^\dagger(x)\psi_3(x)\rangle$. Under the linear response theory, we have

$$I(x) \propto \int dx' d\omega A_\uparrow(x, x'; \omega) A_3(x', x, \omega + \mu_\uparrow - \mu_3) f(\omega) \tag{4.91}$$

where $f(\omega)$ is the Fermi distribution function which reduces to the step function at zero temperature, A_α is the spectral function for state α. As state 3 is non-interacting, we have $A_3 = \sum_n \phi_n(x)\phi_n^*(x')\delta(\omega + \mu_\uparrow + \nu - \epsilon_n)$, where ϕ_n is the single-particle eigenfunction of state 3 and ϵ_n is the eigen-energy, respectively. The key step in our proposal is that in the case where V_3 represents an optical lattice potential in the tight-binding limit, the dispersion of state 3 is proportional to the hopping constant t which decreases exponentially as the lattice strength is increased. In this way the optical lattice changes the effective mass of state 3. For sufficiently large lattice strength, we may therefore neglect the dispersion of state 3 since the lowest band is nearly flat. In other words, under such conditions, $\epsilon_n = \epsilon$ becomes an n-independent constant. Consequently $A_3(x, x') \sim \delta(x - x')$ where the information of state 3 is washed out. In this limit and at zero temperature, the RF signal is then directly related to the LDOS of state $|\uparrow\rangle$ as:

$$I(x) \propto \rho_\uparrow(x, -\mu_\uparrow - \nu + \epsilon)\Theta(\mu_\uparrow + \nu - \epsilon)\,. \tag{4.92}$$

and the spatially resolved RF spectroscopy becomes a direct analog of the STM. A

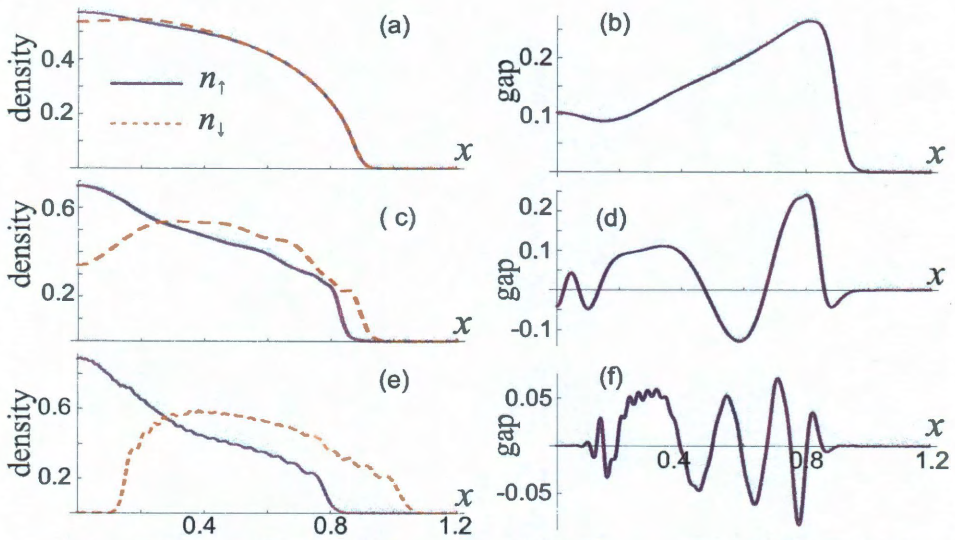

Figure 4.3 : Density (left panel) and gap (right panel) profiles of a trapped system under an extended Gaussian magnetic impurity potential. The width of the impurity potential is $a = 0.2x_{TF}$, while the strength is $u = -0.12E_F x_{TF}$ for (a) and (b); $u = -0.4E_F x_{TF}$ for (c) and (d), and $u = -1.0E_F x_{TF}$ for (e) and (f). Other parameters and units are the same as in Fig. 4.2.

crucial point here is that *only* state 3 experiences the lattice potential. We note here that a spin-dependent optical lattice selectively affecting only one spin state has recently been realized in the lab of de Marco [134]. In their experiment, they use off resonance laser light with polarization so that different hyperfine states interact with the laser light differently. The AC Stark shift is different for different hyperfine states and the light induced effective potential changes from species. The same technique can also be used to create magnetic impurity potentials by an external light field.

4.6 Extended Impurity

Now we turn to the extended impurity. We use Gaussian impurity potentials with finite width $U_\sigma(x) = u_\sigma e^{-x^2/a^2}/(a\sqrt{\pi})$. Since we obtain all of the previous (delta function) physics for narrow widths, we focus on relatively wide potentials. Examples of the density and gap profiles obtained from our B-dG calculations are shown in Fig. 4.3. For an extended impurity potential of sufficient width, the Friedel oscillations are suppressed. This is because now the impurity is complicated and has structure. Friedel oscillations interfere with each other and become smooth.

Under appropriate conditions, the gap profiles exhibit FFLO-like oscillations [135, 136], which has recently received considerable attention in studies of ultra-cold atoms [137, 138, 139, 140, 141]. In the FFLO state, due to population imbalance, the Fermi surfaces of two species mismatch. This causes the phase of the Cooper pair to have a periodic pattern in real space with a characteristic wavelength signifying the center-of-mass momentum of the pair. In previous experiments, polarized Fermi gas have been realized by preparing the gas with an overall population imbalance. Here the overall population is balanced but the magnetic impurity breaks the local population balance and by tailoring the strength and/or the width of the magnetic impurity, one is able to control the magnitude of the population imbalance as shown in Fig. 4.3 which in turn controls the nature of the induced FFLO state. In Fig. 4.3, by changing the magnetic impurity strength, the system evolves from a balanced system to an imbalanced system and the pairing changes from BCS pairing to FFLO pairing. The impurity therefore provides us with a controlled way to create FFLO state.

For simplicity, we have thus far focused on 1D systems. However, we have verified that the essential physics is also valid in higher dimensions. As an example, we illustrate in Fig. 4.4 the effect of an extended magnetic impurity in a 3D trapped

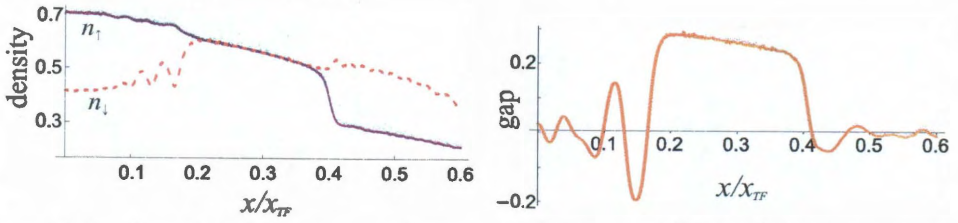

Figure 4.4 : Density (upper panel, in units of $(2E_F)^{3/2}/(6\pi^2)$) and gap (lower panel, in units of E_F) profiles along the x-axis of a 3D trapped system under an extended magnetic impurity potential. The impurity potential is uniform along the radial direction and has a Gaussian form with width $a = 0.3x_{TF}$ along the x-axis. The strength of the impurity is $u = -0.07E_F x_{TF}$. The atom-atom interaction is characterized by the 3D scattering length a_s. Here we have used $1/(k_F a_s) = -0.69$.

system obtained by solving the B-dG equations [125, 126]. Here a total of 1100 atoms are trapped in an elongated cylindrical trapping potential $V(r, x) = \frac{m}{2}(\omega_\perp^2 r^2 + \omega_x^2 x^2)$ with trap aspect ratio $\omega_\perp/\omega_x = 50$. The magnetic impurity centered at the origin, is radially uniform and has a Gaussian profile along the axial direction (x-axis). From the density and gap profiles shown in Fig. 4.4, one can easily identify the induced FFLO regions both near the center and the edge of the trap. In particular, the density oscillations in the spin-down component near trap center may be used as a signature of the FFLO state.

Chapter 5

Summary and Conclusions

In conclusion, the BEC-BCS crossover is becoming one of the most exciting fields in cold atoms and condensed matter physics. It connects to many other fields of physics, such as cuprate high temperature superconductivity, excitons in semiconductors, neutron stars, and the vacuum condensate for the early universe. It is also a candidate for quantum computation and quantum information. In addition, there are still many open questions. One is the accuracy for perturbation theory to give the quantitative explanations for the crossover experiment. In the crossover regime, fermions are strongly correlated and there is no small parameter to do the perturbative expansion. New progress occurs using new approaches, for example, large N expansion[142], [143] and ϵ dimensionality[144]. Another exciting field is the population imbalanced system, where the pairing mechanism for population imbalanced fermions raises long standing interest.

For Fermi superfluids, how to detect pairing is one of the biggest problems. We proposed to use optical spectroscopy in an EIT setting to probe the fermionic pairing in Fermi gases in Chapter 2. We have demonstrated that the EIT technique offers an extremely efficient probing method and is capable of detecting the onset of pair formation (i.e., determining T^*) due to its spectral sensitivity. With a sufficiently weak probe field, the whole spectrum may be obtained in a nearly non-destructive fashion via a relatively fast scan of probe frequency, without the need of repeatedly re-preparing the sample. We noted that in this work, we have focused on probing

the atomic system using photons. In the future, it will also be interesting to study how we can use atomic Fermi gas to manipulate the light. Superfluid fermions can serve as a new type of nonlinear media for photons. Also, we want to remark that, in this work, as a proof-of-principle, we have only considered a homogeneous system. As usual, the trap inhomogeneity can be easily accounted for within the local density approximation. Nevertheless, we noted that the capability of detecting the onset of pairing remains the same even in the presence of the trap. Furthermore, as optical fields are used in this scheme, one may focus the probe laser beam such that only a small localized portion of the atomic cloud is probed, hence there is no need to average over the whole cloud.

One exciting field in both cold atom and condensed matter physics is the topological phase. Spin-orbit coupling is one of the ways to introduce this novel property. In chapter 3, we provide a detailed theoretical description of a two-component Fermi gas with Rashba spin-orbit coupling and external Zeeman field, under the framework of the functional path integral formalism. Many important and experimentally relevant physical quantities in both two- and many-body situations — such as the bound state energy, the effective mass of the two-body bound state, the chemical potential, gap parameter, pairing correlation, quasi-particle dispersion, density of states, spin structure factor, etc. — are calculated in a rather straightforward way using this method. The spin-orbit coupling in general favors the formation of Cooper pair and bound state. In particular, we have found that when a Rashba ring exists for the single-particle ground state, a two-body bound state exists regardless of the sign of the s-wave scattering length.

For the sake of simplicity, we have only presented the zero-temperature results in this paper. The formalism and the relevant equations we have derived are nevertheless

valid for finite temperatures. In addition, we have focused on a uniform system. To take the trap into account, one may adopt the local density approximation [92, 96], under which the trapped Fermi gas was treated as the sum of many small cells with a local chemical potential $\mu(\mathbf{r}) = \mu - V_{\text{trap}}(\mathbf{r})$. In one of our works [92], we have shown that the important qualitative features of the system, like the mixed-spin pairing, anisotropy, enhanced pairing field, etc., are not affected by the presence of the trap. A self-consistent way to include the effects of the trapping potential is to use the Bogoliubov-de Gennes (B-dG) formalism. For large number of atoms as used in most experiments, we expected that the local density approximation should be quite accurate. However, for a system with relatively small number of atoms and tight trapping confinement, or in the case of a vortex state where the order parameter varies significantly in a short length scale, the B-dG approach will be more appropriate.

One crucial feature of the system arising from the spin-orbit coupling is that the superfluid transition temperature is greatly enhanced [93]. The mean-field calculation which we have focused on in this work is not expected to provide an accurate estimate of the transition temperature, particularly for systems with strong interaction. As we have outlined in Sec. 3.2 of chapter 3, the Gaussian fluctuations on top of the mean-field level can be accounted for using the functional path integral formalism. This will lead to a much more accurate calculation of the transition temperature. We plan to address this issue in a future work. Furthermore, the spin structure factor is calculated in the static model which neglects collective excitation. We plan to add this using a dynamic model, such as the random phase approximation(RPA).

In chapter 4, we have investigated the effects of a single classical impurity on a neutral fermionic superfluid. We show that a single classical impurity can be used to manipulate novel quantum states in a Fermi gas. For example, magnetic impu-

rity will induce a mid-gap bound state inside the pairing gap for both spin species. We have proposed an STM-like scheme based on the modified spatially resolved RF spectroscopy to measure the local density of states, from which the mid-gap bound states can be unambiguously detected. As different quantum phases of cold atoms will manifest themselves in their distinct LDOS, we expect this method will find important applications beyond what is proposed here and become an invaluable tool in the study of quantum gases. Finally, by considering an extended magnetic impurity potential in both 1D and 3D systems, we demonstrated the realization of the still unobserved FFLO phase in a controlled manner.

Interesting future directions may involve the study of periodic or random arrays of localized impurities which may be exploited to induce novel quantum states in Fermi superfluids and the consideration of a quantum impurity with its own internal degrees of freedom. Such a system may allow us to explore the Kondo physics in cold atoms.

Bibliography

[1] M. H. Anderson, J. R. Ensher, M. R. Matthews, C. E. Wieman, and E. A. Cornell, Science **269**, 198 (1995).

[2] C. C. Bradley, C. A. Sackett, J. J. Tollett, and R. G. Hulet, Phys. Rev. Lett. **75**, 1687 (1995).

[3] K. B. Davis, M.-O. Mewes, M. R. Andrews, N. J. van Druten, D. S. Durfee, D. M. Kurn, and W. Ketterle, Phys. Rev. Lett. **75**, 3969 (1995).

[4] B. DeMarco and D.S. Jin, Science **285** 1703 (1999).

[5] L. N. Cooper, Phys. Rev. **104**, 1189 (1956).

[6] J. Bardeen, L. N. Cooper, and J. R. Schrieffer, Phys. Rev. **108**, 1175 (1957).

[7] J. Bardeen, L. N. Cooper, and J. R. Schrieffer, Phys. Rev. **106**, 162 (1957).

[8] A. J. Leggett, Rev. Mod. Phys. **47**, 331 (1975).

[9] U. Fano, Phys. Rev. **124**, 1866 (1961).

[10] H. Feshbach, Ann. Phys. (N.Y.) **19**, 287 (1962).

[11] K. M. OHara, S. L. Hemmer, M. E. Gehm, S. R. Granade, and J. E. Thomas, Science **298**, 2179 (2002).

[12] T. Bourdel, J. Cubizolles, L. Khaykovich, K. M. F. Magalhes, S. J. J. M. F. Kokkelmans, G. V. Shlyapnikov, and C. Salomon, Phys. Rev. Lett. **91**, 020402 (2003).

[13] A.J. Legget, in *Modern Trends in the Theory of Condensed Matter* (Springer-Verlag, 1980).

[14] H. T. C. Stoof, M. Houbiers, C. A. Sackett, and R. G. Hulet, Phys. Rev. Lett. **76**, 10 (1996).

[15] G. Bruun, Y. Castin, R. Dum, and K. Burnett, Eur. Phys. J. D **7**, 433 (1999).

[16] M. Holland, et al., Phys. Rev. Lett. **87**, 120406 (2001).

[17] K. Huang, and C. N. Yang, Phys. Rev. **105**, 767 (1957).

[18] L. D. Landau, and E. M. Lifshitz, *Quantum Mechanics, 3rd ed.* (Pergamon, Oxford, 1987).

[19] T. L. Ho, Phys. Rev. Lett. **92**, 090402 (2004).

[20] I. Bloch, J. Dalibard, and W. Zwerger, Rev. Mod. Phys. **80**, 885 (2008).

[21] S. Giorgini, L. P. Pitaevskii, and S. Stringari, Rev. Mod. Phys. **80**, 1215 (2008).

[22] W. Ketterle and M. W. Zwierlein, *Making, probing and understanding ultracold Fermi Gases, Proceedings of the International School of Physics Enrico Fermi, Course CLXIV* edited by M. Inguscio, W. Ketterle, and C. Salomon, (IOS Press, Amsterdam, 2007), p.95.

[23] R. B. Diener, R. Sensarma, and M. Randeria, Phys. Rev. A **77**, 023626 (2008).

[24] D.S. Petrov, et al., Phys. Rev. Lett. **93** 090404 (2004).

[25] G.E. Astrakharchik, et al., Phys. Rev. Lett. **93** 200404 (2004).

[26] D.J. Thouless, Ann. Phys. **10**, 553 (1960).

[27] M. Gell-Mann and K.A. Brueckner, Phys. Rev. **106**, 364 (1958).

[28] E.W. Montroll and J.C. Ward, Phys. Fluids **1**, 55 (1958).

[29] P. Nozieres and S. Schmitt-Rink, J. Low Temp. Phys. **59**, 195 (1985).

[30] Y. Ohashi and A. Griffin, Phys. Rev. Lett. **89** 130402 (2002).

[31] A. Perali, P. Pieri, L. Pisani, and G. C. Strinati, Phys. Rev. Lett. **92**, 220404 (2004).

[32] H. Hu, X.-J. Liu, and P. Drummond, Europhys. Lett. **74**, 574 (2006).

[33] R. Haussmann, Phys. Rev. A **75** 023610 (2007).

[34] J. Stajic, et al., Phys. Rev. A **69** 063610 (2004).

[35] Q.J. Chen, et al., Phys. Rept. **412** 1 (2005).

[36] M. Greiner, et al., Nature **426** 537 (2003).

[37] C.A. Regal, et al., Phys. Rev. Lett. **92** 040403 (2004).

[38] M.W. Zwierlein, et al., Phys. Rev. Lett. **92** 120403 (2004).

[39] C. Chin, et al., Science **305** 1128 (2004).

[40] M.W. Zwierlein, et al., Nature **435** 1047 (2005).

[41] J. Kinnunen, et al., Science **305** 1131 (2004).

[42] P. Massignan, G. M. Bruun, and H. T. C. Stoof, Phys. Rev. A **77** 031601(R) (2008).

[43] Y. Ohashi and A. Griffin, Phys. Rev. A **72**, 013601 (2005).

[44] Z. Yu and G. Baym, Phys. Rev. A **73**, 063601 (2006).

[45] G. Baym, C. J. Pethick, Z. Yu and M. W. Zwierlein, Phys. Rev. Lett. **99**, 190407 (2007).

[46] A. Perali, P. Pieri, and G. C. Strinati, Phys. Rev. Lett. **100**, 010402 (2008).

[47] S. Basu and E. Mueller, Phys. Rev. Lett. **101**, 060405 (2008).

[48] Y. He, C.-C. Chien, Q. J. Chen, and K. Levin, Phys. Rev. Lett **102**, 020402 (2009).

[49] A. Schirotzek, Y. Shin, C.H. Schunck, and W. Ketterle, Phys. Rev. Lett. **101** , 140403 (2008).

[50] C.H. Schunck, Y. Shin, A. Schirotzek, and W. Ketterle, Nature **454** , 739 (2008).

[51] J. T. Stewart, J. P. Gaebler, and D. S. Jin, Nature (London) **454**, 744 (2008).

[52] J. P. Gaebler, J. T. Stewart, T. E. Drake, D. S. Jin, A. Perali, P. Pieri, and G. C. Strinati, Nature Phys. **6**, 569 (2010).

[53] Y. Shin *et al.*, Phys. Rev. Lett **99** 090403 (2007).

[54] W. Zhang, C. A. Sackett, and R. G. Hulet, Phys. Rev. A **60**, 504 (1999).

[55] F. Weig and W. Zwerger, Europhys. Lett. **49**, 282 (2000).

[56] E. Altman, E. Demler, and M. D. Lukin, Phys. Rev. A **70**, 013603 (2004).

[57] J. Ruostekoski, Phys. Rev. A **61**, 033605 (2000).

[58] A. Minguzzi, G. Ferrari, and Y. Castin, Eur. Phys. J. D **17** 49, 2001.

[59] C. P. Search, H. Pu, W. Zhang and P. Meystre, Phys. Rev. Lett. **88**, 110401 (2002).

[60] R. Combescot, S. Giorgini, and S. Stringari, Europhys. Lett. **75** 695 (2006).

[61] G. Veeravalli, E. Kuhnle, P. Dyke, and C. J. Vale, Phys. Rev. Lett. **101**, 250403 (2008).

[62] E. D. Kuhnle, H. Hu, X.-J. Liu, P. Dyke, M. Mark, P. D. Drummond, P. Hannaford, and C. J. Vale, Phys. Rev. Lett. **105**, 070402 (2010).

[63] E. D. Kuhnle, S. Hoinka, P. Dyke, H. Hu, P. Hannaford, and C. J. Vale, Phys. Rev. Lett. **106**, 170402 (2011).

[64] P. Törmä and P. Zoller, Phys. Rev. Lett. **85**, 487 (2000).

[65] G. M. Bruun *et al.*, Phys. Rev. A **64**, 033609 (2001).

[66] G. M. Bruun and G. Baym, Phys. Rev. Lett. **93**, 150403 (2004).

[67] J. Ruostekoski, Phys. Rev. A **60**, R1775 (1999).

[68] I. Carusotto, and Y. Castin, Phys. Rev. Lett. **94**, 223202 (2005).

[69] C.A. Regal and D.S. Jin, Phys. Rev. Lett. **90**, 230404 (2003).

[70] S. Gupta, Z. Hadzibabic, M. W. Zwierlein, C. A. Stan, K. Dieckmann, C. H. Schunck, E. G. M. van Kempen, B. J. Verhaar, and W. Ketterle, Science **300**, 1723 (2003).

[71] K. -J. Boller, A. Imamoglu, and S. E. Harris, Phys. Rev. Lett. **66**, 2593 (1991).

[72] M. Xiao, Y. Li, S. Jin, and J. Gea-Banacloche, Phys. Rev. Lett. **74**, 666 (1995).

[73] E. Arimondo, in *Progress in Optics XXXV*, ed. E. Wolf (Elsevier, Amsterdam, 1996), p. 257.

[74] L. V. Hau, S. E. Harris, Z. Dutton, C. H. Behroozi, Nature **397**, 594-598 (1999).

[75] M. M. Kash, V. A. Sautenkov, A. S. Zibrov, L. Hollberg, G. R. Welch, M. D. Lukin, Y. Rostovtsev, E. S. Fry, and M. O. Scully, Phys. Rev. Lett. **82**, 5229-5232(1999).

[76] R.W. Boyd and D. J. Gauthier, in *Progress in Optics*, ed. E. Wolf (Elsevier, Amsterdam, 2002), Vol **43**, p. 497.

[77] M. Fleischhauer and M. D. Lukin, Phys. Rev. Lett. **84**, 5094 (2000).

[78] C. Liu, Z. Dutton, C. Behroozi, and L. V. Hau, Nature **409**. 490 (2001).

[79] K. J. Weatherill, J. D. Pritchard, R. P. Abel, M. G. Bason, A. K. Mohapatra and C. S. Adams, J. Phys. B: At. Mol. Opt. Phys. **41** 201002 (2008).

[80] M. W. Zwierlein, A. Schirotzek, C. H. Schunck, and W. Ketterle, Science **311**, 492 (2006).

[81] G. B. Partridge, W. Li, R. I. Kamar, Y. Liao, and R. G. Hulet, Science **311**, 503 (2006).

[82] H. Y. Ling, Y.-Q. Li, and M. Xiao, Phys. Rev. A **53**, 1014 (1996).

[83] See, for example, G. D. Mahan, *Many-Particle Physics* (Indiana Univ., 1980).

[84] Y.-J. Lin, R. L. Compton, A. R. Perry, W. D. Phillips, J. V. Porto, and I. B. Spielman, Phys. Rev. Lett. **102**, 130401 (2009).

[85] Y.-J. Lin, R. L. Compton, K. Jiménez-García, J. V. Porto, and I. B. Spielman, Nature (London) **462**, 628 (2009).

[86] Y-J. Lin, R. L. Compton, K. Jiménez-García, W. D. Phillips, J. V. Porto, and I. B. Spielman, Nature Phys. **7**, 531 (2011).

[87] Y.-J. Lin, K. Jiménez-García, and I. B. Spielman, Nature (London) **471**, 83 (2011).

[88] Z. Fu, P. Wang, S. Chai, L. Huang, and J. Zhang, e-print arXiv:1106.0199.

[89] For a brief review, see, for example, Jean Dalibard, Fabrice Gerbier, Gediminas Juzeliū-nas, Patrik Öhberg, eprint arXiv:1008.5378.

[90] J. P. Vyasanakere, and V. B. Shenoy, Phys. Rev. B **83**, 094515 (2011).

[91] J. P. Vyasanakere, S. Zhang, and V. B. Shenoy,Phys. Rev. B **84**, 014512 (2011).

[92] H. Hu, L. Jiang, X.-J. Liu, and H. Pu, e-print arXiv:1105.2488.

[93] Z.-Q. Yu, and H. Zhai, e-print arXiv:1105.2250.

[94] C. Zhang, S. Tewari, R.M. Lutchyn, and S. Das Sarma, Phys. Rev. Lett. **101**, 160401 (2008).

[95] M. Gong, S. Tewari, and C. Zhang, e-print arXiv:1105.1796.

[96] W. Yi, and G.-C. Guo, e-print arXiv:1106.5667.

[97] J.D. Sau, R. Sensarma, S. Powell, I. B. Spielman, and S. Das Sarma, Phys. Rev. B **83**, 140510(R) (2011)

[98] M. Iskin, and A. L. Subaşı, Phys. Rev. Lett. **107**, 050402 (2011).

[99] M. Iskin, and A. L. Subaşı, e-print arXiv:1108.4263.

[100] T. Ozawa, and G. Baym, e-print arXiv:1107.3162.

[101] L. Han, and C. A. R. Sá de Melo, e-print arXiv:1106.3613.

[102] K. Seo, L. Han, and C. A. R. Sá de Melo, e-print arXiv:1108.4068.

[103] L.P. Gor'kov, and E.I. Rashba, Phys. Rev. Lett. **87**, 037004 (2001).

[104] S. Tewari, T.D. Stanescu, J.D. Sau, and S. Das Sarma, New J. Phys. **13**, 065004 (2011).

[105] M. Sato, Y. Takahashi, and S. Fujimoto, Phys. Rev. Lett. **103**, 020401 (2009); Phys. Rev. B **82**, 134521 (2010).

[106] C. A. R. Sá de Melo, M. Randeria, and J. R. Engelbrecht, Phys. Rev. Lett. **71**, 3202 (1993).

[107] M. Randeria, in *Bose-Einstein Condensation*, edited by A. Griffin, D. W. Snoke, and S. Stringari, (Cambridge University Press, Cambridge, England, 1995), p. 355-392.

[108] X.-J. Liu and H. Hu, Europhys. Lett. **75**, 364 (2006).

[109] L. Jiang, L. O. Baksmaty, H. Hu, Y. Chen, and H. Pu, Phys. Rev. A **83**, 061604(R) (2011).

[110] A. V. Balatsky, I. Vekhter, and J.-X. Zhu, Rev. Mod. Phys. **78**, 373 (2006).

[111] H. Alloul *et al.*, Rev. Mod. Phys. **81**, 45 (2009).

[112] A.P. Mackenzie *et al.*, Phys. Rev. Lett. **80**, 161 (1998).

[113] P. T. Sprunger *et al.*, Science **275**, 1764 (1997).

[114] A. J. Millis, Solid State Commun. **126**, 3 (2003).

[115] G. Modugno, Rep. Prog. Phys. **73**, 102401 (2010).

[116] C. Zipkes *et al.*, Nature **464**, 388 (2010).

[117] K. Targońska and K. Sacha, Phys. Rev. A **82**, 033601 (2010)

[118] E. Vernier *et al.*, Phys. Rev. A **83**, 033619 (2011).

[119] I. Bausmerth *et al.*, Phys. Rev. A **79**, 043622 (2009).

[120] P. J. Hirschfeld, D. Vollhard, and P. Wölfle, Solid State Commun. **59**, 111 (1986).

[121] R. Joynt, J. Low Temp. Phys. **109**, 811 (1997).

[122] P. de Gennes, *Superconductivity of Metals and Alloys* (Addison-Wesley, New York, 1966).

[123] X.-J. Liu, H. Hu, and P. D. Drummond, Phys. Rev. A **75**, 023614 (2007).

[124] X.-J. Liu, H. Hu, and P. D. Drummond, Phys. Rev. A **76**, 043605 (2007).

[125] L. O. Baksmaty *et al.*,Phys. Rev. A **83**, 023604 (2011).

[126] L. O. Baksmaty, H. Lu, C. J. Bolech, and H. Pu, New J. Phys. **13**, 055014 (2011).

[127] L. Yu, Acta Phys. Sin. **21**, 75 (1965).

[128] H. Shiba, Prog. Theor. Phys. **40**, 435 (1968).

[129] A. I. Rusinov, Sov. Phys. JETP **29**, 1101 (1969).

[130] Ø. Fischer *et al.*, Rev. Mod. Phys. **79**, 353 (2007).

[131] J. Kinnunen, M. Rodriguez, and P. Törmä, Phys. Rev. Lett. **92**, 230403 (2004).

[132] Y. He, Q. Chen, and K. Levin, Phys. Rev. A **72**, 011602(R) (2005).

[133] Y. He *et al.*, Phys. Rev. A **77**, 011602(R) (2008).

[134] D. McKay and B. DeMarco, New J. Phys. **12** 055013 (2010).

[135] P. Fulde and R. A. Ferrell, Phys. Rev. **135** A550 (1964).

[136] A. I. Larkin and Y. N. Ovchinnikov Sov. Phys.-JETP **20** 762 (1965).

[137] Y.-A. Liao *et al.*, Nature **467**, 567 (2010).

[138] G. Orso, Phys. Rev. Lett. **98**, 070402 (2007).

[139] H. Hu, X.-J. Liu, and P. D. Drummond, Phys. Rev. Lett. **98**, 070403 (2007).

[140] I. Zapata *et al.*, Phys. Rev. Lett. **105**, 095301 (2010).

[141] K. Sun *et al.*, Phys. Rev. A **83**, 033608 (2011).

[142] P. Nikolic and S. Sachdev, Phys. Rev. A **75** 033608 (2007).

[143] M.Y. Veillette, et al., Phys. Rev. A **75** 043614 (2007).

[144] Y. Nishida and D.Y. Son, Phys. Rev. Lett. 97 050403 (2006).